Ultrasound Shear Strain Imaging for Breast Cancer Classification

by

Haiyan Xu

A dissertation submitted in partial fulfillment of

the requirements for the degree of

Doctor of Philosophy

(Electrical Engineering)

at the

UNIVERSITY OF WISCONSIN – MADISON

2013

Date of final oral examination: 12/11/2013

The dissertation is approved by the following members of the Final Oral Committee:

Tomy Varghese, Professor, Electrical Engineering
Yu Hen Hu, Professor, Electrical Engineering
Willis T. Tompkins, Professor, Electrical Engineering
James. Zagzebski, Professor, Medical Physics
Timothy Hall, Professor, Medical Physics

Abstract

Early detection of breast cancer can significantly reduce breast cancer mortality and morbidity. Pathological differences between benign and malignant masses include the stiffness contrast, nonlinear stiffness variations and changes in breast mass boundaries evoked by desmoplastic scirrhous reactions. Ultrasound as a low cost and safe imaging modality has become the primary adjunct to mammography for screening. Ultrasound elasticity imaging can differentiate breast masses based on different mechanical and acoustic properties.

The goal of this dissertation is to evaluate features (normalized axial and full shear strain area, namely NASSA and NFSSA) derived from shear strain imaging for breast mass differentiation. Finite element simulation, tissue-mimicking (TM) phantom experiments, and *in-vivo* studies, are utilized to evaluate new algorithms and perform statistical analysis.

A new two-dimensional (2D) parallelogram kernel motion tracking algorithm was developed in this dissertation to estimate displacement vectors for normal and shear strain imaging, utilizing beam-steered ultrasound radiofrequency data. Quantitative analysis based on the elastographic signal-to-noise (SNR_e) and contrast-to-noise (CNR_e), was utilized to demonstrate the statistical significance of the results obtained from TM uniformly elastic and ellipsoidal inclusion phantoms respectively. Our results demonstrate that our 2D deformation tracking significantly outperforms the currently utilized one-dimensional (1D) algorithm for beam-steered data.

Classification results obtained using radiofrequency data sets on 123 patients (benign: 65, malignant: 58) acquired at four hospitals equipped with two different ultrasound systems, were

utilized to demonstrate the feasibility of using these normalized features extracted from the axial strain and axial-shear strain images for breast cancer diagnosis. Scatter plots of the NASSA feature shows that most of the malignant masses exhibit a NASSA value larger than 1.2, while for benign masses, it is lower than 1.2. The corresponding area under (AUC) the receiver operating characteristic (ROC) curve of 0.9 demonstrates the potential of using the NASSA feature for breast mass classification. Integrating the NASSA feature with the previously proposed features, namely the 'size ratio' and the 'stiffness contrast', further improves the classification performance, achieving an AUC of 0.93. These results demonstrate the potential of elasticity based imaging features for breast mass differentiation and classification.

Acknowledgements

First of all, I would like to express my great and sincere thanks to my advisor, Dr. Tomy Varghese, for his invaluable assistance, guidance, encouragement, and support during my graduate studies. He offered me this opportunity to work on this interesting topic. He helped me to build up my knowledge foundation for this area. He inspired me with new ideas and provided me with constructive suggestions on my research topic. I sincerely appreciate his willingness to give his time so generously on my papers and thesis.

I would like to thank Dr. James Zagzebski, for his guidance on my ultrasound system basis. I would also deliver my gratefulness to Dr. Timothy Hall and Dr. James Zagzebski for providing me with so many inspirational discussions throughout my Ph.D. study. I would like to thank Dr. Ernest Madsen, for his help during my ultrasound experience. I also would like to thank Dr. Willis Tompkins for his impressive course and project experiences. I would like to thank members of defense committee, Dr. Yu Hen Hu, Dr. Zagzebski, Dr. Hall, Dr. Varghese, Dr. Tompkins, for their insightful comments and great suggestions for this study.

I also want to thank my colleagues and friends in the ultrasound group for help and fruitful discussion. Thank you Dr. Jingfeng Jiang, Dr. Min Rao, Dr. Matt McCormick, Dr. Hao Chen, Dr. Nick Rubert, Dr. Eenas Omari, Dr. Matt Bayer, Dr. Ryan DeWall, Chi Ma, Xiao Wang, Kayvan Samimi, Ivan Rosada-Mendez, Dr. Kibo Nam and Atul Ingle.

Finally, I would like to send my heartfelt thanks to my families: my parents Yuping Xu and Yuying Wu for their blessings; my husband, Shilin Ding, for his complete support throughout my study.

Contents

List of Figures

List of Tables

Chapter 1:

Introduction

1.1 Breast Cancer Characteristics

One out of eight women (12%) will be diagnosed with breast cancer during her life time in the United States, accounting for approximately 28% of all new cancer cases among women [1]. Breast cancer is identified as a malignant tumor that starts in the cells of the breast, and can continuously grow into (invade) surrounding tissue or spread (metastasize) to other parts of the body. There are several types of breast cancers. Among them, ductal carcinoma in situ (DCIS) is the most common type of non-invasive breast cancer, accounting for 1 out of 5 new breast cancer cases. DCIS refers to cancer cells that are still inside the ducts and have not spread through the walls of the ducts into the surrounding breast tissue. Though DCIS is a treatable breast cancer, it can develop into invasive breast cancer without treatment. Thus early detection is significantly important for breast cancer treatment. Invasive (infiltrating) ductal carcinoma (IDC), as the most common type of breast cancer, starts in a milk duct of the breast and spreads into the fatty tissue of the breast. Statistically, for all the invasive breast cancers diagnosed, 80% of these are IDC, while 10% are classified as invasive lobular carcinoma (ILC), with the remaining 10% being comprised of the remaining tumor types such as invasive mammary cancer, papillary cancer, etc. On the other hand, non-cancerous new growths that occur in the breast, characterized as non invasive and non life threatening are benign tumors, the most common being fibroadenomas.

Fibroadenomas as the most common type of benign tumor display characteristic discrete margins and appear as well defined masses [1].

One of the pathological differences between benign and malignant breast masses is the stiffness contrast, when compared to adjacent adipose or fibrous tissue. Previous studies have shown that scirrhous carcinoma of the breast are characterized as extremely stiff nodules[2], while benign masses rarely manifest as extremely stiff masses [3]. In addition, cancers infiltrate into surrounding normal tissue and evoke a desmoplastic scirrhous reaction, that will also manifest as pathological differences on boundary conditions between tumors and surrounding tissue. Ultrasound studies [2, 4-7] have indicated that fibroadenomas have more circumscribed margins and are more loosely bound to the surrounding tissue and in some instances may be surrounded by a capsule, while cancerous new growths (malignant breast tumors) typically exhibit an irregular or spiculated appearance and are firmly bound to the surrounding tissue through infiltration.

1.2 Current Techniques for Early Detection of Breast Cancer

Early detection of breast cancers before they start to cause symptoms can significantly reduce breast cancer mortality. As suggested by The American Cancer Society, breast self examination (BSE) and clinical breast examination (palpation) (CBE) are the most frequently used diagnostic tools for early detection of breast abnormalities. However, due to its subjective nature and dependence on the expertise of the physician, CBE only provides a sensitivity of 27.6%, and specificity of 99.4% for all cancers (invasive and noninvasive) [8]. Thus various imaging based

screening modalities are utilized for tumors detection, including mammography, magnetic resonance imaging (MRI), and ultrasound imaging.

Mammography as the primary screening modality for breast cancer detection, is a fairly low cost ($100 - $150 per visit) method with a sensitivity of 0.52, a specificity of 0.91 and an accuracy of 0.78 as described in Berg et al. (table 2) [9-10]. However, its sensitivity drops to about 45% for extremely dense breasts (correlated with younger ages) [9]. The accuracy of mammography scans is dependent on how flat the breast can be compressed, which can be a very painful experience for the patient. In addition, the exposure of the patient to x-ray radiation is another limitation for mammography. In fact, exposure to x-ray radiation may lead to future development of cancer [1].

Magnetic resonance imaging is recommended for women at high risk of breast cancer, and is generally used to supplement mammography [9]. However, due to patient claustrophobia, time and financial constraints (>$2k per visit), only 57.9% of the patients who participated in this study with an elevated risk of breast cancer agreed to undergo MRI after mammography and ultrasound scanning [11]. In addition, MRI has been reported to have very high sensitivity but lower specificity [10, 12-13].

Ultrasound as a low cost, non-invasive and safe imaging modality has become the primary adjunct to mammography to differentiate between solid and cystic masses and to guide biopsy procedures. Based on a study of 4814 screening ultrasounds in three consecutive years combined, Berg et al., showed that the combination of mammography and ultrasound can provide a sensitivity of 0.76 with a specificity of 0.84 [10]. The sensitivity of the combined mammography

plus ultrasound and MRI is 1, with a drop in the specificity to 0.65. Incorporating conventional screening ultrasound or MRI with mammography in women with a high risk of breast cancer resulted in not only higher cancer detection but also an increased false-positive rate.

The primary goal of screening modalities is the early detection of breast cancer. However, only 40% of the high-risk women undergo regular screening mammograms in the United States [14]. Of these patients, about 1.3-2.5% also underwent a breast biopsy [15-16]. Unfortunately the benign to malignant ratio for breast biopsies ranges from 5.0 to 0.2 for women in different age ranges, leading to more benign masses being biopsied [15-16]. Incorporating new non-invasive and non-ionizing imaging features to further differentiate solid masses as benign or malignant, could improve the early detection accuracy and thereby reduce unnecessary biopsies.

Limitations of current imaging methods have led to increasing interest in utilizing pathological differences between benign and malignant masses as a means of differentiation [17-27]. Therefore ultrasound elasticity imaging methods that differentiate features with different mechanical properties (stiffness and boundary changes) and acoustic properties have gained attention recently. It has also been suggested that elasticity imaging, which is becoming commercially available on clinical ultrasound systems, may improve the sensitivity of ultrasound to differentiate benign from malignant masses [26, 28-39]. Based on a multinational study of 939 masses, Berg et al. have shown that adding shear-wave elastographic features to BI-RADS breast masses analysis could improve the specificity of breast masses classification without losing the sensitivity [40]. A comprehensive review and discussion of ultrasound elasticity imaging for breast cancer detection and classification is presented in Chapter 2.

1.3 Overview of this Dissertation

The goal of the research presented in this dissertation, was to develop normal and shear strain imaging techniques to provide a non-invasive method with high sensitivity and specificity for breast tumor classification. A brief overview of the chapters within the dissertation are as follows.

Chapter 2 provides a comprehensive literature review on ultrasound breast imaging, ultrasound breast elastography, and its application in breast cancer diagnosis. Various displacement and strain estimators described in the peer-reviewed literature are also introduced and discussed in this chapter.

Chapter 3 describes finite element analysis (FEA) methods used to model breast masses with different bonding conditions to surrounding tissue, under a quasi-static deformation. Strain tensor estimation methods based on displacement fields obtained from FEA are also introduced in this chapter. Different features derived from shear strain images for breast tumor classification are also developed and discussed in this chapter.

Chapter 4 investigates the tumor detection performance of these features derived from both axial shear and full shear strain images on tissue-mimicking (TM) phantoms. The impact of various parameters on the classification performance with these normalized features are also studied and discussed.

Chapter 5 presents a new two-dimensional (2D) deformation tracking algorithm that utilizes parallelogram shaped kernels to estimate 2D angular displacements from beam-steered

radiofrequency data acquired on TM phantoms. The complete shear strain tensor image is then calculated from axial and lateral displacement vectors estimated from the angular 2D displacements. Improvements over 1D deformation tracking methods using beam-steered data are quantified in terms of the elastographic signal-to-noise ratio (SNR_e) and contrast-to-noise ratio (CNR_e) based on TM phantom experiments.

Chapter 6 evaluates the feasibility of using normalized features extracted from the axial-shear strain images derived from *in-vivo* data sets for breast cancer diagnosis. The *in-vivo* data sets on patients were acquired at four hospitals equipped with two different ultrasound systems. Scatter plots of the normalized features and corresponding receiver operating characteristic (ROC) curves are presented to demonstrate the potential of using the normalized axial shear strain area feature derived from the axial-shear strain tensor for breast tumor classification.

Chapter 7 investigates the combined classification performance obtained using both the newly developed normalized axial-shear strain feature in this dissertation and previously proposed elastographic features utilized for breast mass characterization. Support vector machine (SVM) and ROC analysis using the leave-one-out criteria were used to obtain the combined classification performance utilizing all the above features.

Finally, the contributions of this dissertation and possible future work are discussed in Chapter 8.

Chapter 2:

Literature Review

2.1 Ultrasound Breast Imaging

Wild and Reid [41] first built a real-time handheld ultrasound scanner and clinically applied it for breast scanning in 1954. Breast ultrasound has played an important role in both breast screening and diagnosis, such as to help diagnose breast abnormalities detected during a physical exam, to screen and characterize abnormalities exhibited on mammography or magnetic resonance imaging (MRI), and to guide many interventional procedures, such as biopsy [1, 12]. Currently, there are various modalities available for breast cancer screening, including mammography, ultrasound, computed tomography (CT) and MRI. Among these, mammography is the primary modality used for breast screening. However, mammography doesn't work well in dense breast, thus they are mainly recommended for women older than 40 years when most of their dense tissues have been replaced by fat [1, 12, 42-43]. In addition, the X-ray radiation exposure and pain introduced during breast compression during the process are also the limitations of mammography [1, 12, 42-43]. Compared to other clinical systems, ultrasound imaging is a low cost modality with no ionizing radiation involved during the examination. Ultrasound is especially intended for women with dense breasts, younger women, and pregnant or lactating patients. Initial ultrasound screening is recommended as the preferred option for women younger than 30 years with a dominant mass or asymmetric nodularity [44]. It is also recommended for women aged 30 years or older with masses marked under the Breast Imaging

Reporting and Data System (BI-RADS) scale from 1 to 3. In addition, ultrasound is widely used as the primary adjunct to mammographic screening to reveal a suspicious breast abnormality and is utilized to detect these in dense breasts, where these masses are not detected in a mammogram. Various modes of ultrasound imaging have been utilized, including B-mode ultrasonography, Doppler imaging, elasticity imaging and so on [1, 43, 45-47]. Among these modes, B-mode imaging is the most commonly used for clinical breast diagnosis [1]. Clinical ultrasonography based methods are utilized for identifying suspicious sonographic features [4, 6, 48-52], such as irregular mass shapes, mass margins, echo intensity and acoustic shadowing which indicate malignancy as well as noting bland features such as circumscribed margins, oval shape, or posterior acoustic enhancement suggesting benign breast abnormalities. Much of the analysis in current clinical ultrasound is aimed at distinguishing cystic from solid tumors and differentiating benign from malignant solid breast masses.

A well-known example is the set of ultrasound B-mode image based features described by Stavros et al. [49] that apply features such as spiculation, angular margins, calcification, "echogenicity", shadowing, and branching patterns to stratify breast masses. The results demonstrated a sensitivity of 98.4% for malignant and a specificity of 67.8% with an overall accuracy of 72.9% [49]. This was followed by efforts to encode many of these criteria into an ultrasound detection scheme similar to the BI-RADS description in mammography [12, 49, 53-54]. One significant drawback of this approach is that some of these parameters are described very subjectively and can be system-dependent. For example, the degree of shadowing (attenuation artifact) behind a lesion is a phenomenon that depends on the relative acoustic attenuation, interface size relative to the ultrasonic beam, poor contact between transducer and skin, complex combination of absorption and refraction along the mass border and so on. In

addition, the "echogenicity" of different structures in the breast is estimated by comparing to normal breast fat portrayed as gray[49].

Berg et al. studied 2809 women with elevated risk of breast cancer and dense breasts obtained from 21 sites using 3 annual independent screening modalities (mammography, ultrasound and MRI) [10, 12]. Among these patients, 2662 women consented to take mammography and ultrasound in randomized order, and 612 of 703 women chose to undergo an MRI after 3 rounds of both screening modalities. Berg et al. have shown that ultrasound screening increased cancer detection at a rate of 5.3 cancers per 1000 women in the first year, with an average of 4.3 women per 1000 in three follow up years. Additional ultrasound information could improve the sensitivity of mammography from 0.52 to 0.76, at a cost of reduction in the specificity from 0.91 to 0.84. However, unlike screening ultrasound that was available and acceptable to most patients, only 58% of ACRIN 6666 participants were accepted to undergo an MRI with no additional charge [11].

2.2 Ultrasound Breast Elastography

Previous studies have shown that scirrhous carcinoma of the breast, a common subtype of infiltrating ductal carcinoma (IDC), is characterized as extremely stiff nodules [2]. On the other hand, benign masses rarely manifest as extremely stiff masses [55]. In addition, cancers infiltrate into surrounding normal tissue and evoke a desmoplastic scirrhous reaction that will also cause pathological differences on the boundary between tumors and surrounding tissue. However, conventional ultrasound imaging that distinguishes masses based on their acoustic properties cannot depict both the stiffness and boundary properties accurately. Thus ultrasound breast elasticity imaging, a method that is based on imaging the viscoelastic properties of breast masses

has gained clinical significance [23, 26-27, 29, 56-59]. By assuming tissue to be isotropic in elasticity under small deformations, tissue viscoelastic properties can be represented by two parameters, i.e. the Young's modulus and Poisson's ratio [29]. The ratio of Young's modulus values used to represent the relative stiffness of tissues and Poisson's ratio denotes tissue's compressibility. Various approaches have been proposed to image tissue elasticity. A commonly used method, referred to as quasi-static elastography, acquires ultrasound radiofrequency (RF) echo signals before and after an applied deformation to characterize the tissue response by depicting stiffness variations.

2.2.1. Displacement and Strain Estimation

Different methods have been developed to track displacement (time delay estimation) between pre- and post- deformation ultrasound data, which might be in the form of either B-mode, envelope signals or RF data. Based on tracking kernel dimensions, the displacement estimator can be grouped into one-dimensional (1D) time delay estimators [60], two-dimensional (2D) block matching estimators [61-62] and three-dimensional (3D) estimators [63-64]. Real-time estimation was developed using 1D displacement tracking along a single A-line, however, it failed to track motion in a 3 cm wide field of view for small deformations, and its tracking error increased with increased deformation [61] and tracking depth [21]. The cross-correlation coefficient as a domain similarity metric can provide accurate matching results. On the other hand, the sum-absolute difference approach can provide fast motion tracking at the cost of accuracy. Since 2D cross-correlation based motion tracking methods can provide both axial and lateral displacement tracking results with high accuracy among all others similarity metric methods, it is currently the dominant approach for ultrasound motion tracking. A 2D cross-

correlation based block matching method was implemented by searching within a specified search range to find both axial and lateral displacement vectors.

Both normal and shear strain tensors have been obtained from the gradient of displacement estimates as shown in Equation 2.1 and 2.2:

$$\mathrm{e}_{zz} = \frac{\partial d_z}{\partial z},\ \mathrm{e}_{xx} = \frac{\partial d_x}{\partial x}, \text{and } e_{yy} = \frac{\partial d_y}{\partial y} \tag{2.1}$$

where e_{zz}, e_{xx} and e_{yy} denote three normal strain tensors components, axial-strain, lateral-strain and elevational strain along the z, x and y direction respectively. d_z, d_x and d_y represent the displacement vectors along z, x and y respectively. Axial strain is computed from the gradient of the tissue displacement, along the beam direction. Lateral strain is estimated from the gradient of the tissue displacements along the lateral direction (perpendicular to the beam direction) and elevational strain from the gradient perpendicular to both beam propagation and scan plane direction.

The full shear strain tensor includes both axial-shear and lateral shear strain tensor components as defined in equation 2.2

$$\text{Full - shear strain} = e_{zx} + e_{xz} = \frac{1}{2}\left(\frac{\partial d_z}{\partial x} + \frac{\partial d_x}{\partial z} \right) \tag{2.2}$$

where z and x represent the axial and lateral directions, respectively, e_{zx} represents the axial-shear strain tensor, and e_{xz} represents the lateral-shear strain tensor. The elevational component is ignored here due to transducer limitation.

Due to the lack of phase information to track in the lateral and elevational directions, most of previous studies were based on strain estimated along the axial, or the beam propagation

direction, ignoring displacement and strain components in the lateral and elevational direction [30, 62, 65-66]. Methods to estimate axial, lateral and shear strain tensors have been described in the literature. Konofagou and Ophir (1998) described an algorithm for estimation of both axial and lateral displacements and thereby the axial, lateral and shear strain tensor using weighted interpolation between neighboring RF A-lines in the lateral direction along with iterative correction of lateral and axial displacements. The assumption of incompressibility has been utilized to estimate lateral strains from the estimated axial strain [67]. Interpolation for cross-correlation motion tracking [68-69] and multi-dimensional processing [70-71] has also been proposed.

Techavipoo et al. [72] proposed an approach to obtain normal and shear strain tensors using RF echo data collected using a phased array transducer that is translated to obtain angular data along a scan plane. Rao et al. [73-74] implemented this approach using beam steering on a linear array transducer, along with 1D cross correlation based displacement tracking of the angular data sets. Both of these approaches assumed that estimated displacement noise artifacts were independent and identically distributed, modeled using a zero-mean normal probability density function. Quantitative experimental results with spatial angular compounding demonstrate that least-squares compounding provides significant improvement in the elastographic signal-to-noise ratio (SNR_e) and contrast-to-noise ratio (CNR_e), when compared to weighted-compounding [75]. Chen and Varghese [76] extended this analysis, eliminating assumptions on the angular displacement noise artifacts by incorporating them into the least squares strain estimation using a cross-correlation matrix of the displacement noise artifacts. In addition, angular compounding has been used to estimate variations in lateral attenuation to reduce shadowing of spatially compounded images [77] and to estimate Young's modulus [78].

Viola et al. (2002) and Rao et al. (2007) have also investigated the use of lateral shear deformations to enhance shear strain visualized for TM phantoms. Their results indicated that shear strain elastography can characterize regions of increased bonding between the lesion and background tissue. They also presented a theoretical analysis on signal de-correlation that suggested that this technique might introduce large shearing strains, thereby improving the signal to noise ratio of the estimated shear strain over techniques that utilize a uniaxial deformation.

Hansen et al. [79] presented an approach utilizing 2D block matching based motion tracking to estimate angular displacements. However, again only the axial component of the 2D block motion tracking was utilized to estimate the axial shear-strain tensor, ignoring the noisy lateral component. Results demonstrated that the angular compounding of RF data from three angles (large negative and positive beam steered angles and 0^o) improves the accuracy of strain tensor estimation. In this dissertation, a full 2D shear strain tensor is estimated based on incorporating both the axial and lateral displacement components obtained using 2D block matching based tracking. Angular compounding performance studies utilizing different beam steering increments along with maximum values of the beam steered angles are also discussed in this dissertation in Chapter 5 and 6.

2.2.2. Methods for Ultrasound Breast Elastography

Based on the type or mode of the applied deformation, ultrasound elastography could be classified into those that utilize quasi-static deformations [29, 57, 80], transient impulse excitation [19, 81-84], and harmonic excitation [59, 85].

In quasi-static elastography, the axial displacements (along the direction of insonification/deformation) or lateral displacements (perpendicular to the beam direction) are

estimated using time-delay estimation techniques on frames of RF echo-signals acquired before and after a small amount (typically 1%) of deformation, as described earlier. Since low-frequency deformations on the order of 1-10 Hz will not generate appreciable shear waves in tissue, these deformation responses (local stiffness to applied deformation) can be implied as a linear process. Quasi-static deformations were applied to the tissue using either a stepper motor [30] or real-time freehand palpation [31] to acquire pre- and post- deformation RF data. Since malignant masses are generally stiffer than benign masses, they are typically depicted as regions with low strains on the axial strain images when compared to the softer background adipose or fibrous tissue. Garra et al.[30] demonstrated this as a method of potential. In addition, he also found that cancers appear as larger stiffer regions on axial strain images. This was hypothesized to be caused by a desmoplastic reaction due to infiltration of cancer cells into surrounding tissue when compared to their dimensions on corresponding ultrasound B-mode images. Fibroadenomas on the other hand appear as masses with similar dimensions in both the B-mode and axial strain images. These results were further confirmed by Hall et al. who extended this criteria to a comparison based on the lesion area ratio between strain and B-mode images. In addition, observation of brightness changes in fibroadenomas along with deformation can provide improved discrimination performance [32]. Regner et al. [26] and Burnside et al. [23] have demonstrated the potential of breast mass differentiation based on utilization of this size ratio feature. More recent publications from the international community have confirmed the value of strain imaging on similar or slightly larger patient populations (ranging from 99 to 193 cases) [86-89]. Performance has been similar to previous studies demonstrating areas under the Receiver Operating Characteristic (ROC) curve of between 0.8 and 0.9, which, while promising, is not sufficient as a stand-alone predictor of malignancy to obviate biopsy.

Real-time elastography based clinical trials have also been performed using conventional ultrasound systems supported with additional software to estimate the elastic modulus of tissue in a region of interest (ROI) [90]. A color map or gray-scale maps are employed to portray relative stiffness variance within the ROI. One of the first real-time clinical trial based evaluation of *in-vivo* breast masses using real time elastography was performed by Itoh et al. [90] using a EUB-6500 scanner (Hitachi Medical, Tokyo, Japan) and the combined autocorrelation method [91]. Breast lesions from 111 patients (59 benign and 52 malignant) were scored based on a 5 level elastography scoring system proposed by the authors. Score level were also associated with and compared to BI-RADS criteria [92]. Results demonstrated a sensitivity of 71.2% and a specificity of 96.6% with 84.7% accuracy to differentiate benign from malignant masses using a cutoff value between level 4 and 5. In a multicenter study of 874 breast lesions (614 benign and 260 malignant), Rizzatto et al.[93-94] further demonstrated the feasibility of breast lesion differentiation. The authors set guidelines for an elastography-based scoring system using real time elastography. Barr et al. [95] presented real-time elastography-based imaging using a Siemens Antares Premier Edition system (Siemens Medical Solutions, Mountain View, CA), where an EI/B-mode size ratio equal to or greater than 1 was regarded as a malignant lesion. Based on a total of 251 breast lesions (197 benign and 54 malignant), the results obtained provided a sensitivity of 100% and specificity of 95%. Barr et al.[96] also presented a multicenter un-blinded study for breast tumor classification describing 635 breast lesions (413 benign and 222 malignant) that was implemented over six sites where scanning was performed. The results of breast masses classification described an overall sensitivity of 98.6%, ranging from 96.7% to 100% for the six individual sites and an overall specificity of 87.4%, ranging from 66.7% to 95.4% for the six individual sites.

Using a transient pulse (acoustic radiation force) excitation, the transient deformation response of soft tissue can be monitored using the same transducer or different transducers to estimate elasticity parameters. Depended on different tracking strategies (on-axis/off-axis), it can further be divided as acoustic radiation force impulse (ARFI), shear wave elasticity imaging (SWEI), spatially modulated ultrasound radiation (SMURF) and so on.

Acoustic radiation force elasticity imaging uses acoustic radiation forces to generate localized displacement of a region of interest in tissue, with a tracking pulse aligned on-axis with the excitation pulse and applied at a given time duration after the excitation pulse (0.5-1 msec). Both excitation and tracking pulse sequence were swept across the scanning field to image regions of interest [18-19, 84, 97-98]. By applying cross-correlation or phase-shift based algorithms, the axial displacement can be estimated to obtain information on the stiffness properties of tissue. In general, the darker regions of ARFI images are associated with stiffer tissues and brighter regions are associated with compliant tissue. Thus these images display the relative stiffness difference in tissue. Nightingale et al. first clinically tense the ARFI technique for breast lesion differentiation [17, 19, 99]. In order to obtain quantitative information about the tissue stiffness, different time of flight (TOF) methods such as time to peak [82], leading edge arrival time [81] have also been utilized to estimate the speed of shear wave propagation [82-83].

Commercial implementations of ARFI have also been made available recently [100]. One of the implementation is on the ACUSON S2000 system (Siemens Medical solutions, Mountain View, CA) that utilizes ARFI imaging equipped with the Virtual Touch Tissue Imaging tool. Meng et al.[98], evaluated a total of 86 patients with 92 breast lesions (65 benign and 27 malignant) based on virtual touch tissue quantification (VTQ) and the area ratio (AR). The

results demonstrated that benign lesions exhibited statistically lower VTQ values than malignant lesions. In addition, the sensitivity of using VTQ values to predict malignant breast lesion is 96.3%, where the specificity is 91.8%. Based on a study of 30 breast lesions (13 benign and 17 malignant) that were classified as BI-RADS category 4, Tozaki et al. [101-102] also demonstrated that the mean shear wave velocity in malignant lesions was higher than that observed in benign regions.

Shear wave elasticity imaging (SWEI), on the other hand, was performed by tracking the deformation response at multiple locations with known separation distances to the region where the excitation was applied. In general, shear waves propagate slowly (~3 m/s) in soft tissue, but faster in stiffer tissue [103-104]. Different methods have been applied to quantitate shear wave propagation speed. Typically, TOF methods have been utilized. The algorithm apply linear regression between the wave arrival time at distances from the ARFI excitation to estimate the speed of the propagating shear wave [105].

Another commercial system utilized for shear wave imaging is the Supersonic Aixplorer imaging system equipped with linear and phase array transducers (Supersonic Imagine, Aix-en-Provence, France) [81, 83]. Combined with the “ultrafast echographic imaging”, SSI can display elasticity maps that recover both the shear wave speed and estimates of the Young's modulus of *in-vivo* breast lesions in real time [24, 83, 106]. A clinical study based on 15 patients demonstrated the feasibility of using SSI to provide quantitative information and to differentiate stiffer breast tissue from soft tissue. A study presented by Chang et al. on 152 patients showed that high stiffness values obtained using shear wave elastography (SWE) using the Supersonic Imagine system correlated with aggressive breast cancer subtypes [107]. Youk et al. [108] also

demonstrated improved detection performance by integrating SWEI into the B-mode imaging BI-RADS classification with subcategory 4. The area under the curve (AUC) of the elasticity ratio feature was improved from 0.952 to 0.978, and Young's modulus feature was improved from 0.859 to 0.949 [30]. The impact of a multi-observer performance on SWEI breast tumor classification was also reported in the literature [30, 109], where SWEI from two different views were shown to improve detection performance.

For harmonic methods, excitation can be applied using either a mechanical vibration (such as sono-elasticity) or multiple acoustic radiation force pulses (such as vibro-acoustography) to drive soft tissue at frequencies ranging from 20 to 100 KHz. Sono-elastography imaging used ultrasound Doppler methods to image low-frequency (less than 1kHz) shear wave propagation within elastic medium, from which the tissue mechanical properties (Young's modulus) can be estimated [59, 110-112]. The low-frequency vibration utilized in sonoelasticity is provided by an external source in close contact with the patient. The vibration amplitude and phase detected by Doppler techniques are utilized to portray a vibration map, where bright regions represent high vibration amplitude and dark regions are associated with lower vibration amplitude [113]. Vibro-acoustography, a method first developed by Fatemi and Greenleaf [114-115], used two ultrasound beams of slightly frequency to intersect at a given location. Nonlinear mixing generate an acoustic response (acoustic emission) that was used for imaging and tissue characterization. Typical ultrasound frequencies were on the order of 2-5MHz, with frequency offsets between beam of 10-70 kHz [116]. The phase and amplitude of the vibration were recorded using a hydrophone. Initial clinical results of breast tumor classification based on 57 participants presented a sensitivity ranging from 69% to 100%, and specificity for diagnostic accuracy of 94%, also demonstrated the potential application of vibro-acoustography in the

detection of breast abnormalities detection [117-118]. Other methods that reconstructed Young's modulus from the force-displacement slope with an assumed finite element (FE) model were also investigated [119-121]. In these methods, the tumor was first sliced, photographed and segmented to create a FE mesh model. The force was applied on the model to calculate a force-displacement curve. The Young's modulus of the tumor was estimated from the slope of the force-displacement curve. Results obtained from 169 fresh *ex vivo* breast tissue sample demonstrated that fibroadenomas exhibited twice the stiffness when compared to normal breast fat and fibroglandular tissue, while malignant tumors exhibited a 3-6 times increased stiffness [119-121].

2.3 Ultrasound Shear Strain Tensor

Much of the previous research on ultrasound strain, modulus, and shear wave imaging as described above is based on interpretations of stiffness variations in breast tissue. However, the stiffness feature may not always provide differentiation between benign and malignant masses. For example, some fibroadenomas can be stiffer than malignant masses, while cancers such as necrotic or mucinous subtypes can be softer than others [119]. Previous ultrasound studies [2, 4-7] have indicated that malignant breast tumors typically exhibit an irregular or spiculated appearance and are firmly bound to the surrounding tissue through infiltration, whereas fibroadenomas have more circumscribed margins and are loosely bound to the surrounding tissue and in some instances, may be surrounded by a capsule. Since cancers infiltrate into surrounding normal tissue, they are far less mobile and exhibit reduced slippage during deformation, in contrast to benign masses like fibroadenomas that are not firmly attached to surrounding normal tissue [20, 72, 80, 122-124]. Shear strain estimates characterize breast masses based on their

mobility or attachment to background tissue [80, 124].The estimator are computed as defined by Equation 2.2.

Shear strain tensors estimated around the breast mass boundary could provide supplementary information on the bonding between a tumor and the surrounding tissue. Shear strain imaging has been shown to provide new and additional features that can be utilized to differentiate benign breast masses (unbound) from malignant masses (bound) [72, 80, 122]. The full-shear strain component includes contributions from both axial-shear and lateral-shear in response to an applied deformation. However, due to the significantly lower lateral resolution associated with current clinical ultrasound systems, when compared to the axial resolution, many investigators utilize only the axial component of the estimated local displacements to generate axial-shear strain images [20, 123-124], while ignoring the contributions of the lateral-shear component [72, 80, 122]. This represents a practical solution since estimation of lateral displacements from RF data acquired along the 0^{o} insonification or backscatter direction can be noisy, leading to noise artifacts in the shear strain image.

In-vivo results on breast masses demonstrating the use of "normalized area of the axial-shear strain regions" was first reported by Thitaikumar et al. [124]. Where the dimensions of the breast mass on B-mode images are used as a normalization factor for the axial shear strain images. Changes in the normalization of the feature, primarily through utilization of breast mass dimensions obtained from the axial-strain image along with use of the acronym NASSA to denote the 'normalized axial shear strain area' feature was reported in Xu et al. [20]. The NASSA feature has been utilized as a discriminator to classify breast masses as benign or malignant in the literature [20, 123-124].

In this dissertation we report on the use of shear strain imaging for breast mass characterization and differentiation.

Chapter 3:

Evaluation of Strain Tensor Features Using Finite Element Analysis

3.1 Introduction

Finite element analysis (FEA) software ANSYS (ANSYS Inc., Pittsburgh, PA, USA), was utilized to evaluate the contributions of different breast mass characteristics to the normal and shear strain images, to develop features for classification of these masses into benign or malignant, and to access their impact on breast tumor classification. FEA models were utilized to model different breast tumor mass shapes and their degree of attachment or bonding to the background normal tissue, and the different normal and shear strain patterns obtained are discussed. Local axial and lateral displacements generated using finite element simulations were then used to generate normal and shear strain images for both two-dimensional (2D) and three-dimensional (3D) simulations.

3.2 Finite Element Model

Two-dimensional (2D) and 3D finite element simulations for spherical and ellipsoidal masses embedded in a uniformly elastic background were modeled for shear strain imaging analysis using ANSYS (ANSYS Inc., Pittsburgh, PA, USA) software. For 2D simulations, a cross-section

Material in this chapter was adapted from:

Xu, H., T. Varghese, and E.L. Madsen, *Analysis of shear strain imaging for classifying breast masses: finite element and phantom results.* Med Phys, 2011. **38**(11): p. 6119-27.

of the ellipsoidal mass was modeled, referred to as an ellipse or elliptical model in our FEA simulations. For the 2D model with the embedded spherical mass, a single inclusion with a 10mm diameter was embedded within a uniform background with dimensions 40 mm × 40 mm. In a similar manner, the 2D ellipsoidal mass model utilized a single elliptical mass characterized by major (a) and minor (b) axis of 12 and 9 mm respectively, embedded within a uniformly elastic background as shown in Figure 3.1. For the 3D model with the embedded spherical mass, a single inclusion with a dimension 12 mm ×10 mm ×10 mm was embedded at the center of a uniform background with dimensions 40 mm × 40 mm × 40 mm. The stiffness ratio between the inclusion and background was set based on the ratio of their corresponding Young's Modulus values. A quasi-static deformation was applied on the top surface of the simulation model as the perturbation for strain imaging, as shown in Figure 3.1.

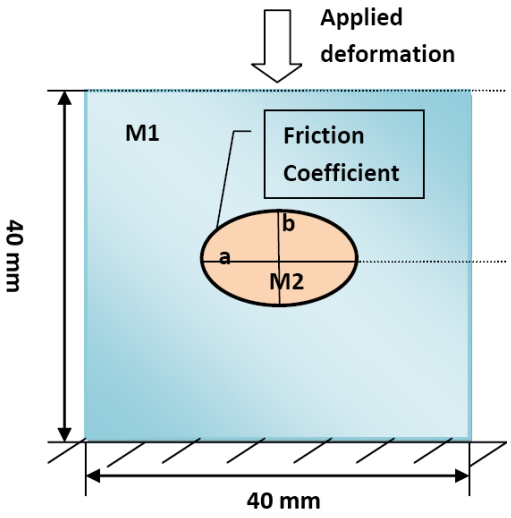

Figure 3.1 Schematic diagram of the FEA simulation model for an ellipsoidal mass.

Both 2D and 3D models were implemented using ANSYS software. The following steps were utilized for each simulation:

1) **Element Type:** Structural masses in ANSYS were composed of small elements. The choice of the element may affect the simulation performance. In our study, the element

labeled 8node 82 was used for 2D simulations, while the element labeled as 10node187 was utilized for 3D simulations.

2) **Material Models:** Two different tissue material types were utilized in the FEA model to simulate the TM phantom including both a tumor and the normal surrounding tissue. We assumed that both tissues were linear, isotropic and elastic, requiring only two constants to describe the deformation response [57]: the Young's modulus and the Poisson's ratio. The Poisson's ratio for both the background and inclusion materials was set to 0.495, simulating incompressible tissue. The Young's modulus, on the other hand was set to different values for the tumor and the background based on the experimental results reported in the literature for breast tissue [55]. The ratio of Young's Modulus values represents the relative stiffness ratio between inclusion and the background. For the simulation, the Young's modulus of the background was set to 10 kPa, while that of the inclusion was set to 30 kPa.

3) **Modeling:** For both 2D and 3D simulations, the tumor was placed at the center of the uniformly elastic background. In order to create a tumor mass with an asymmetrical positioning of the inclusion, two co-ordinates that are common to both the lesion and background res were used for modeling. A 0^0 co-ordinate system was created to build a background mass model, and this defined the reference co-ordinates. A 2^{nd} co-ordinate system with a specified rotation angle (θ) and vector ratio corresponding to the ratio between the ellipsoidal inclusion major and minor axis, when measured in the reference co-ordination was generated to model an ellipsoidal inclusion located 0^o to its co-ordinate system, but at some specified rotation angle (θ) with respect to the reference co-ordinate system. The θ co-ordinate system was placed at the center with selected angle (θ) and

ratio to the global co-ordinate utilized to create key points for the masses (command: local, csys, k). An inclusion was generated using key points located within the θ co-ordinate system, while the background region subtracted from the inclusion was generated within 0^o coordinate system. Thus the number of key points and volume will define available subsets of the areas and volumes respectively.

A distinct boundary, referred to as the "contact interface" was created between the inclusion embedded within the background surrounding tissue to model the bonding of the inclusion surface and background. Different degrees of bonding at the mass/background interface was modeled using friction coefficient values ranging from 0.01 to 100 depicting unbound to bound masses [125]. For modeling malignant masses, the inclusion was bound or attached to the surrounding medium, implemented in ANSYS by gluing the contact surfaces together during the modeling step. The benign mass, on the other hand (unbound mass) was implemented in ANSYS by assigning a lower friction coefficient value to the contact interface elements at the boundary. Note that meshing was required for the area/volume before corresponding contact pairs could be created.

4) **Meshing:** Since shear strain distributions are generated at the background/inclusion interface, we are more interested in the variation of these displacements/deformations at the interface or boundary of the inclusion. Thus the meshed regions around these interfaces were assigned with a finer mesh density in order to obtain accurate lateral and axial displacement information from the FEA simulation. The mesh for both the 2D and 3D asymmetric phantom simulation generated using ANSYS is shown in Figure 3.2.
5) **Loading:** The simulated FEA phantom model was fixed on the bottom surface (to model the attachment of breast tissue to the chest wall), and was free to move on both sides. A

quasi-static compressive deformation (1% of the phantom height) was then applied to the top surface of the phantom.

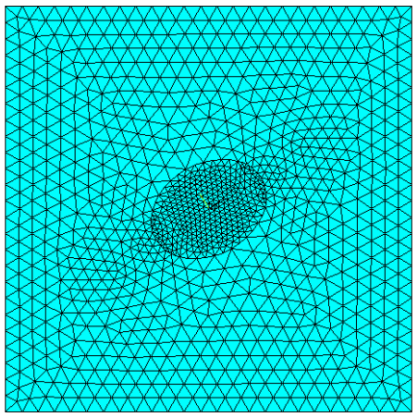

(a)

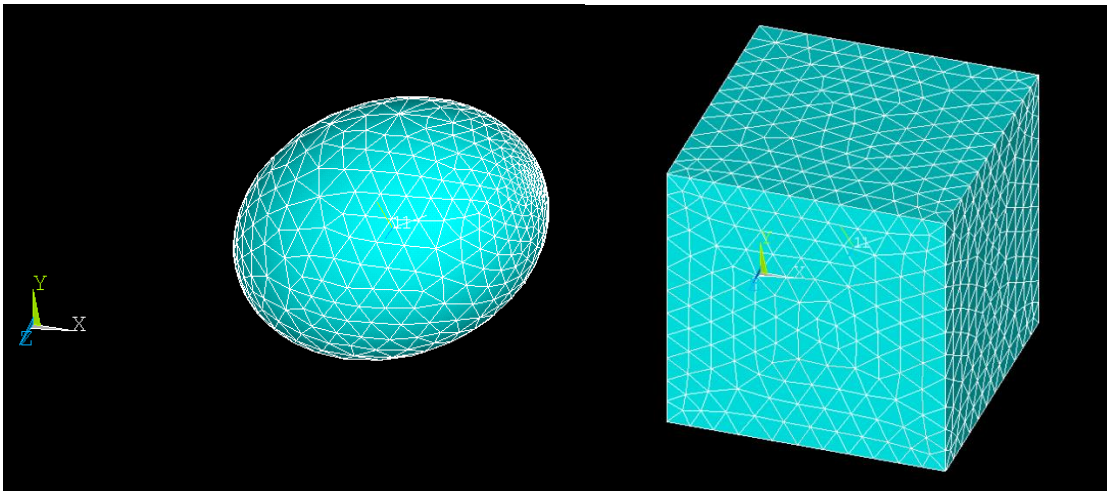

(b) (c)

Figure 3.2 Mesh for the asymmetric 2D (a) and 3D (b-c) phantom model with inclusion rotated at 30^{o} to the applied deformation. The mesh was generated using ANSYS.

Based on these settings, ANSYS solves the finite element analysis problem and computes the local displacement in response to the applied deformation at each node. The coordinate position and displacement files were saved for further analysis and for the ultrasound simulation.

3.3 Strain Tensor Estimation

The ideal (noiseless) pre- and post-deformation displacement information describing both the axial and lateral displacements were output from ANSYS software and interpolated to a regular Cartesian grid using MATLAB (The Mathworks, Natick, RI). This interpolated displacement data was utilized to evaluate the respective normal strain and shear strain distributions. Both strain tensors, including the normal strain tensor (defined in equation 2.1) and shear strain tensor (defined in equation 2.2) were calculated from the local displacement components using a least-squares strain estimator [126].

$$d_z(i) = sz(i) + n, \text{ for } i = 1, \cdots, N \tag{3.1}$$

where $d_z(i)$ and $z(i)$ are the displacement and spatial depth at i^{th} point along the axial direction, with strain parameters s and noise parameter n. The parameter *s* is the slope or the local strain of the linear model, which is estimated from the slope of the best fit line through N consecutive displacements.

Shear strain estimates characterize breast masses based on their mobility or attachment to background tissue [80, 124]. Since cancers infiltrate into surrounding normal tissue and evoke a desmoplastic scirrhous reaction, the hypothesis is that they may be far less mobile than fibroadenomas. Therefore they do not slip during compression or deformations as do fibroadenomas [6]. Thus in FEA simulations, we model benign masses (unbound) with a lower friction coefficient value at the contact interface between the inclusion and background tissue, while the malignant masses are modeled with full attachment by gluing the contact interfaces together. Shear strain images estimated from the shear strain tensor has the potential for clearly

depicting any sliding or slippage of such masses that may occur during a uniaxial deformation or shear deformation of tissue.

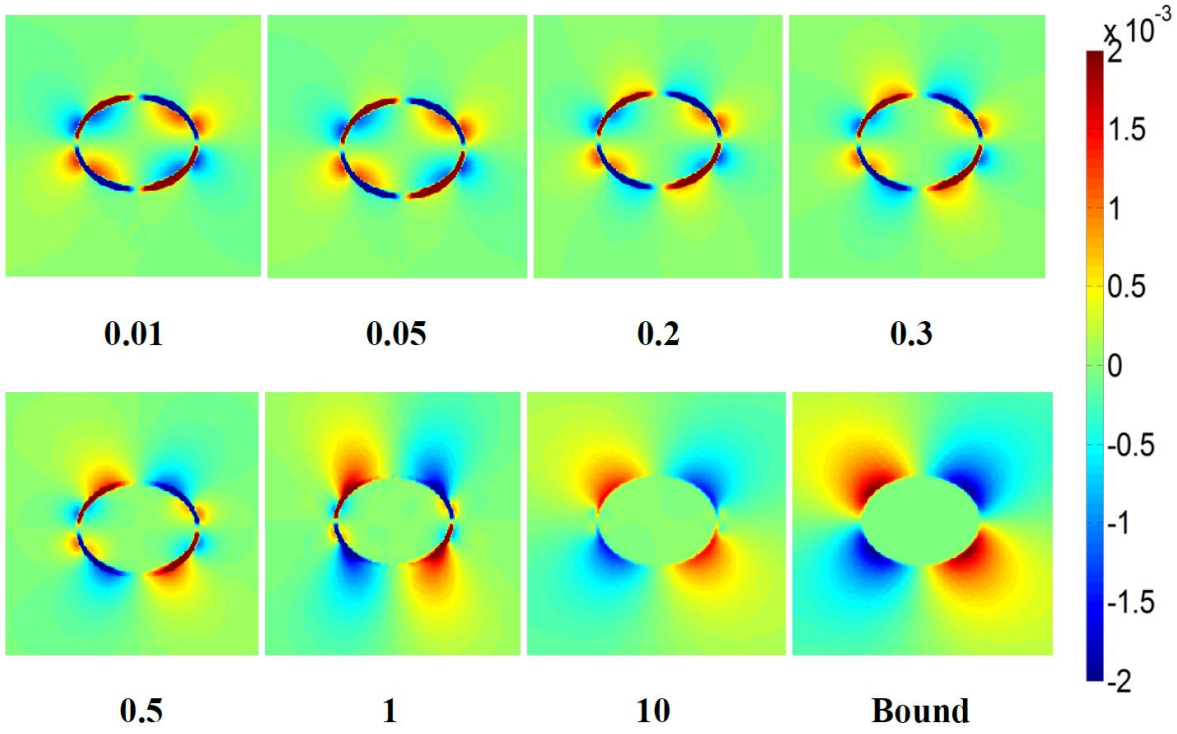

Figure 3.3 Comparison of 2D full-shear strain images obtained for 2D elliptical inclusions for different values of the friction coefficient depicting loosely bound to firmly bound masses.

Figure 3.3 presents full-shear strain images obtained from FEA simulations with friction coefficient values ranging from 0.01(denoting loosely bound or unbound) to firmly bound inclusions. Observe the distinct variations in the shear strain patterns between the bound and unbound masses. The “halo” (or larger strain value region) around the inclusion for the unbound mass no longer exists for the bound mass [125]. This concept was described previously in Rao et al. [125] for spherical inclusions under lateral shear deformations. The presence of the “halo” was due to the presence of shearing forces on the inclusion when it was oriented at an angle to the applied deformation, and is one feature that can be used to differentiate between benign and malignant breast masses. Secondly, full-shear strain area patterns outside the breast masses

appear to be larger for the bound mass[124] when compared to the unbound ones. Thirdly, axial-shear strain areas visualized inside breast masses for the unbound mass referred to as “fill-in” [127-128], were not observed for the bound mass. Finally, the negative and positive shear strain area patterns that represent the direction of the displacement or strain estimated with respect to the applied deformation, exhibit symmetric patterns for inclusions that are placed symmetrically within the uniformly elastic background.

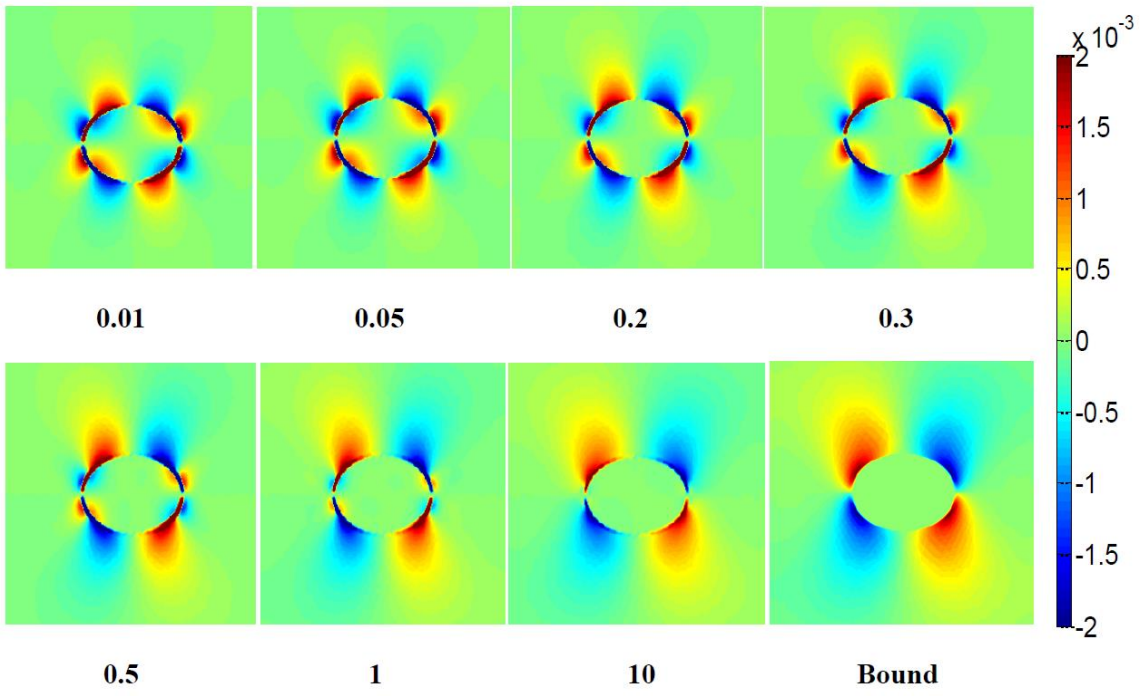

Figure 3.4 Comparison of 2D axial-shear strain images obtained for 2D elliptical inclusions for different values of the friction coefficient depicting loosely bound to firmly bound masses.

However, the estimation of lateral displacements from radiofrequency (RF) data acquired along the 0^o insonification or backscatter direction can be noisy leading to additional noise artifacts in the shear strain image. Many investigators utilize only the axial component of the estimated local displacements to generate axial-shear strain images [20, 123-124], while ignoring the contributions of the lateral-shear component [72, 80, 122]. Thus we will first evaluate the

feasibility of using axial-shear strain images for breast tumor classification. Figure 3.4 demonstrates comparison results of axial-shear strain patterns obtained with an elliptical inclusion with friction coefficient ranging from 0.01 to the firmly bound condition. Observe that axial-shear strain patterns inherit most features present in full-shear strain patterns. Both the "halo" and "fill-in" only exist in the loosely bound model. Phantoms of symmetrical axial-shear strain area patterns outside the masses increased along with the increased friction coefficient values, with a relative lower variance when compared to full-shear strain area patterns.

The impact of inclusion orientation with respect to the applied deformation for both bound and unbound masses was also evaluated based on FEA simulation. We evaluate the impact of asymmetric inclusion orientations by rotating the elliptical inclusion from 0^o to 90^o in steps of 10^o (relative to the top surface of the model where the quasi-static deformation is applied). The unbound inclusions were assigned a friction coefficient value of 0.2, while the contact interfaces of bound model were glued together. From the comparison results between unbound and bound shown in Figure 3.5, observe that: 1) the presence of the "halo" was not affected by the asymmetrical location of the mass in background tissue. However, the direction of the "halo" shear pattern varied along with the asymmetric positioning of the inclusion. In addition, the "halo" area increased with the asymmetric orientation of the mass in the uniformly elastic background; 2) "fill-in" [127-128] exists only in unbound masses; 3) "fill-in" increased gradually along with orientation angle of the inclusion from 0^o to 40^o to the peak and then decreased gradually from 50^o to 90^o. Thus the orientation angle or the degree of asymmetric inclusion with respect to the applied deformation primarily determines the "fill in" volume; 4) the axial-shear strain area outside the inclusion was not affected by asymmetric orientation of the inclusion. It appears to be consistently larger for the bound masses than the unbound masses over all

orientation angles. 5) the negative and positive shear strain patterns area outside the inclusion also vary along the contact interface for asymmetric orientations of the mass in the uniformly elastic background.

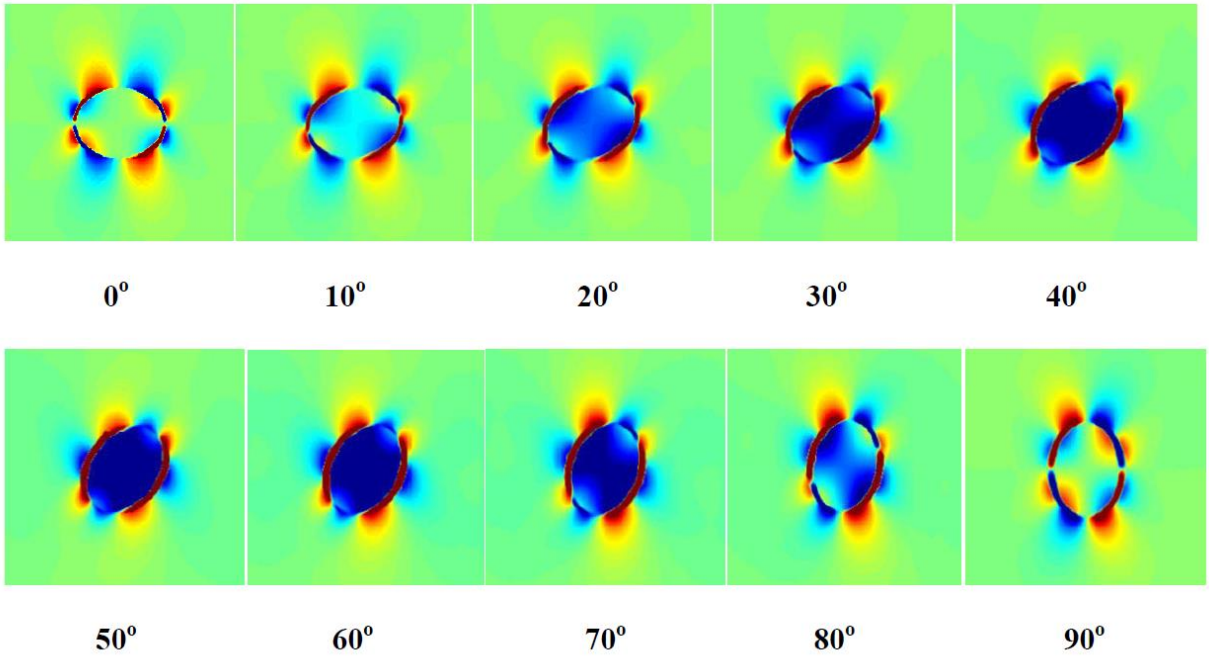

(a)

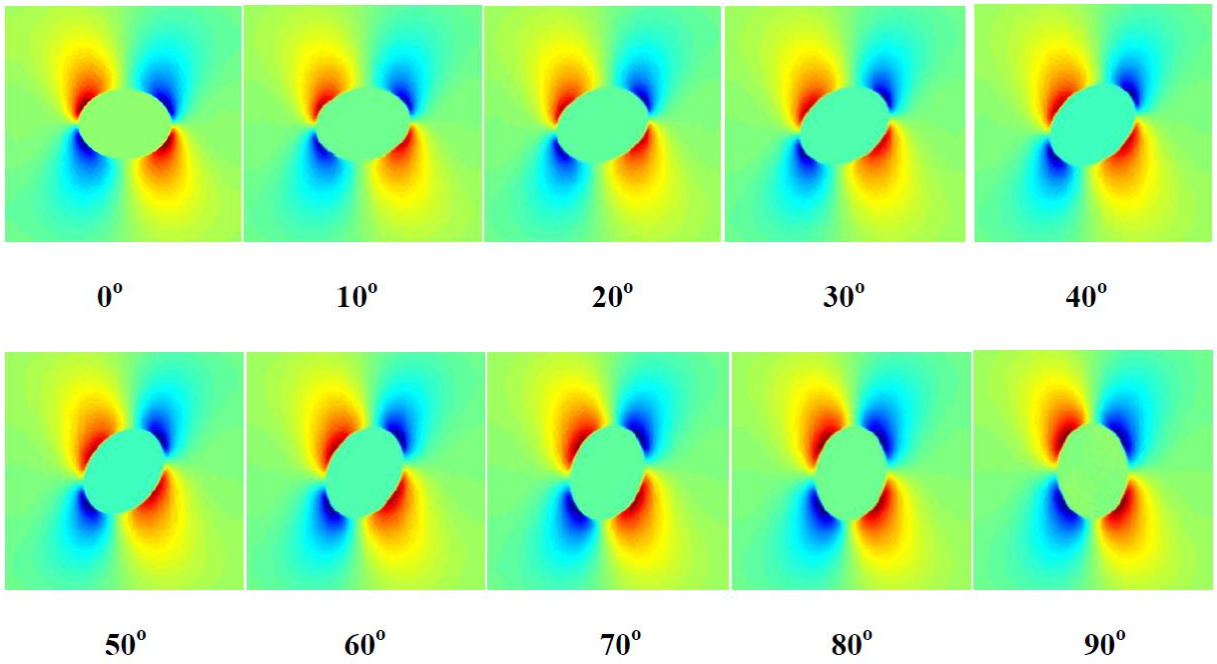

(b)

Figure 3.5 Comparison of axial-shear strain images obtained with elliptical inclusions oriented at different degrees to the applied deformation for both (a) loosely bound and (b) firmly bound masses.

We also evaluated the impact of partial bonding caused by possible partial infiltration of invasive tumors into surrounding normal background tissue using FEA simulations. The impact of a partial bonding condition was studied by setting sections of the contact interface with different specified friction coefficient values for a single mass. The unbound parts were assigned a friction coefficient value of 0.05, while the contact interfaces of bound sections were glued together.

Figure 3.6 demonstrates results obtained for inclusions with different levels of partial bonding, ranging from unbound to fully bound for a single quadrant, for two and three-quadrants and finally all quadrants being completely bound. We found that the presence of the "halo" effect corresponded only to the quadrant with an unbound contact interface. Secondly, the "fill in" effect varied for the partly bonded quadrants of the masses, especially for the ¼ (quadrant) and ¾ (3 quadrant) bound masses. The variation in the "fill in" direction along with the partly bound contact interface was also evaluated as shown in Figure 3.7. This was built up by setting a quadrant (¼) of the contact interface as bound (or unbound) and the remaining 3 quadrants (¾) of the contact interface as unbound (or bound). Since the spherical inclusion phantom is symmetrical, only the quadrant of the contact interface on the right side of the inclusion was evaluated. For each case the contract interface of the top quadrant or the bottom quadrant of the inclusion was either bound or unbound, and the remaining three quadrants of the interface possessed the opposite contact parameters. Observe that the direction (positive or negative) of

the “fill in” depended on the position of the unbound contract interface or unbound quadrant. Also note that the “fill in” area increases with partial bonding.

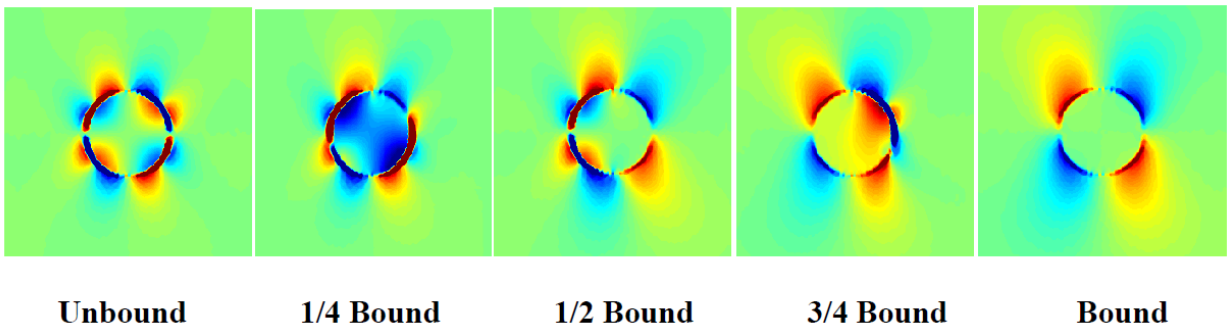

Figure 3.6 Axial-shear strain patterns obtained with inclusions with only part of the contact interface completely bound to the background tissue. The increase in the bound contact interface was increased in quadrant blocks.

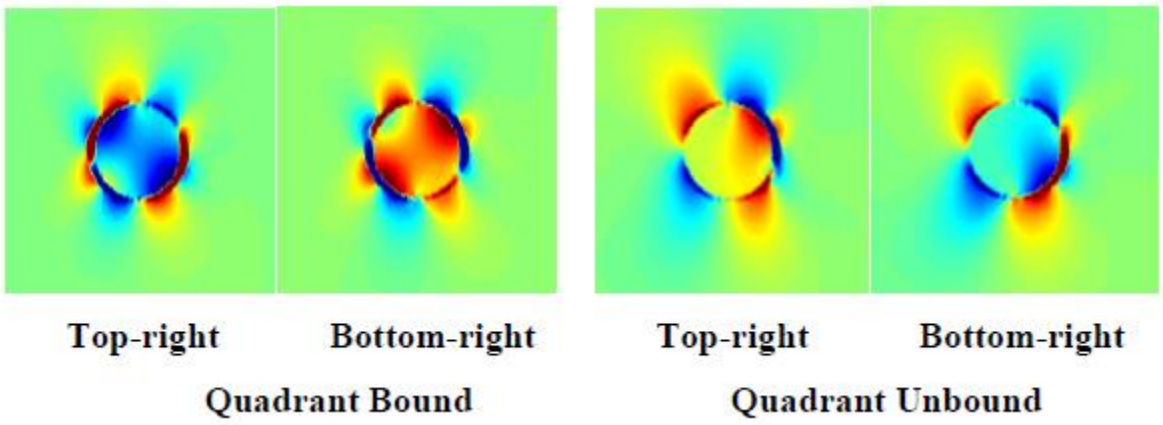

Figure 3.7 Axial-shear strain patterns obtained for partially bound/unbound inclusions

Figure 3.8 presents 3D simulation results of the axial-shear strain for a symmetric ellipsoidal unbound mass (a) and a symmetric ellipsoidal bound mass (b). Both the ellipsoidal inclusions simulated were three times stiffer than the background with an applied deformation equal to 1% of the model height. For the unbound mass, a contact interface with friction coefficient values equal to 0.01 was created between the inclusion and background; for the bound mass, the inclusion was glued to the background. The threshold of the iso-surface displayed in Figure 3.8

was set at -0.008 (blue) and 0.008 (red) respectively. Observe that 1) similar to the 2D cross sectional axial-shear strain image, the 3D bound mass exhibits a larger axial-shear strain volume when compared to that obtained with the unbound mass. 2) axial-shear strain tensors are only displayed outside the mass or inclusion. Note that the shear strain patterns extend further away from the inclusion center for the bound mass. 3) "fill in" is exhibited only with unbound masses.

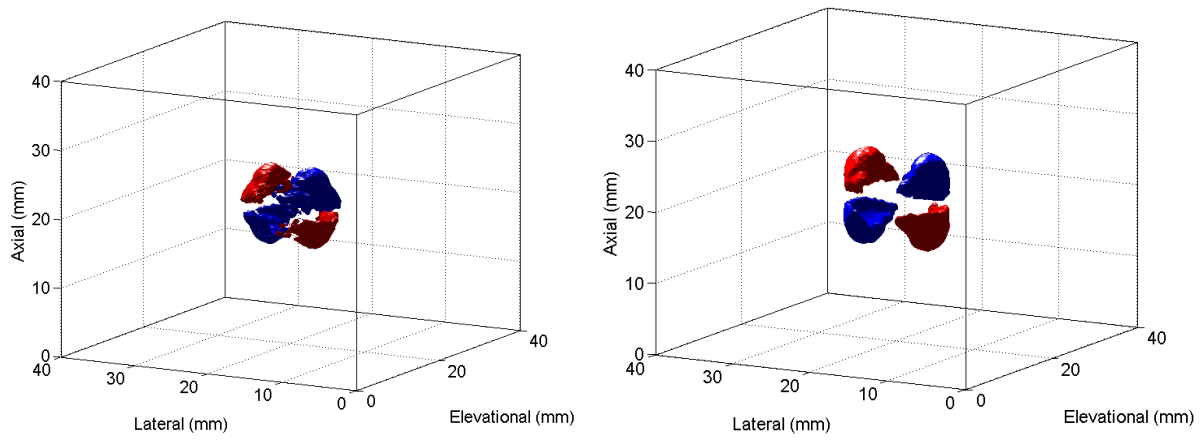

(a) (b)

Figure 3.8 3D axial-shear strain patterns for a simulated symmetrical ellipsoidal inclusion, that is not bound to the background (a) and bound (b) to background tissue.

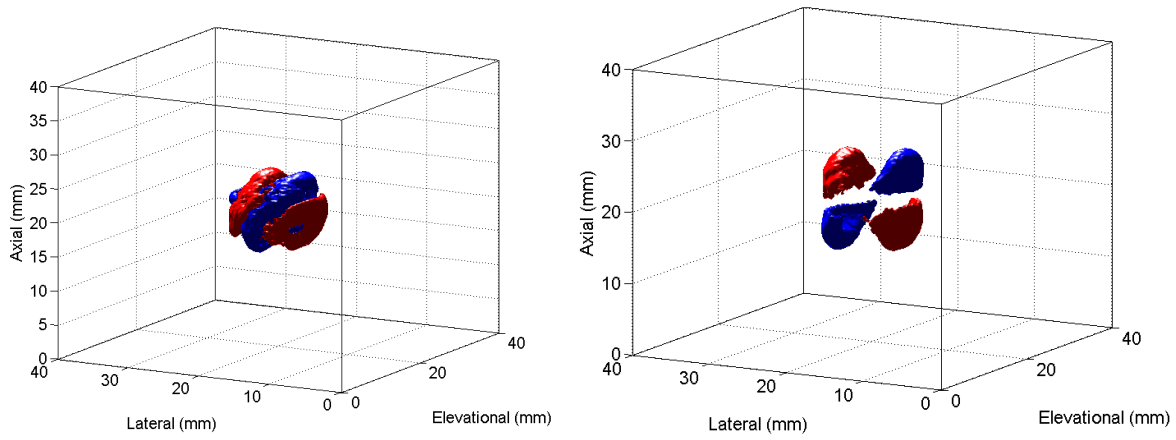

(a) (b)

Figure 3.9 3D axial-shear strain patterns for a simulated asymmetrical ellipsoidal inclusion, that is not bound to the background (a) and bound (b) to background tissue. Both unbound and bound ellipsoidal masses were oriented at a 30^{o}angle to the applied deformation.

The axial-shear strain tensors obtained for a 3D asymmetrical ellipsoidal mass for both unbound (a) and bound (b) inclusions are also shown in Figure 3.9. The asymmetrical inclusion was simulated by placing the inclusion at an angle of 30^{o} to the applied deformation. The threshold of the iso-surface displayed in Figure 3.8 was set to similar values as used to produce Figure 3.7. Observe that both positive and negative axial-shear strain tensors were displayed along with the inclusion surface. The existence of the "fill in" patterns is consistent with cross-sectional results obtained for 2D simulations of asymmetrical unbound mass described previously.

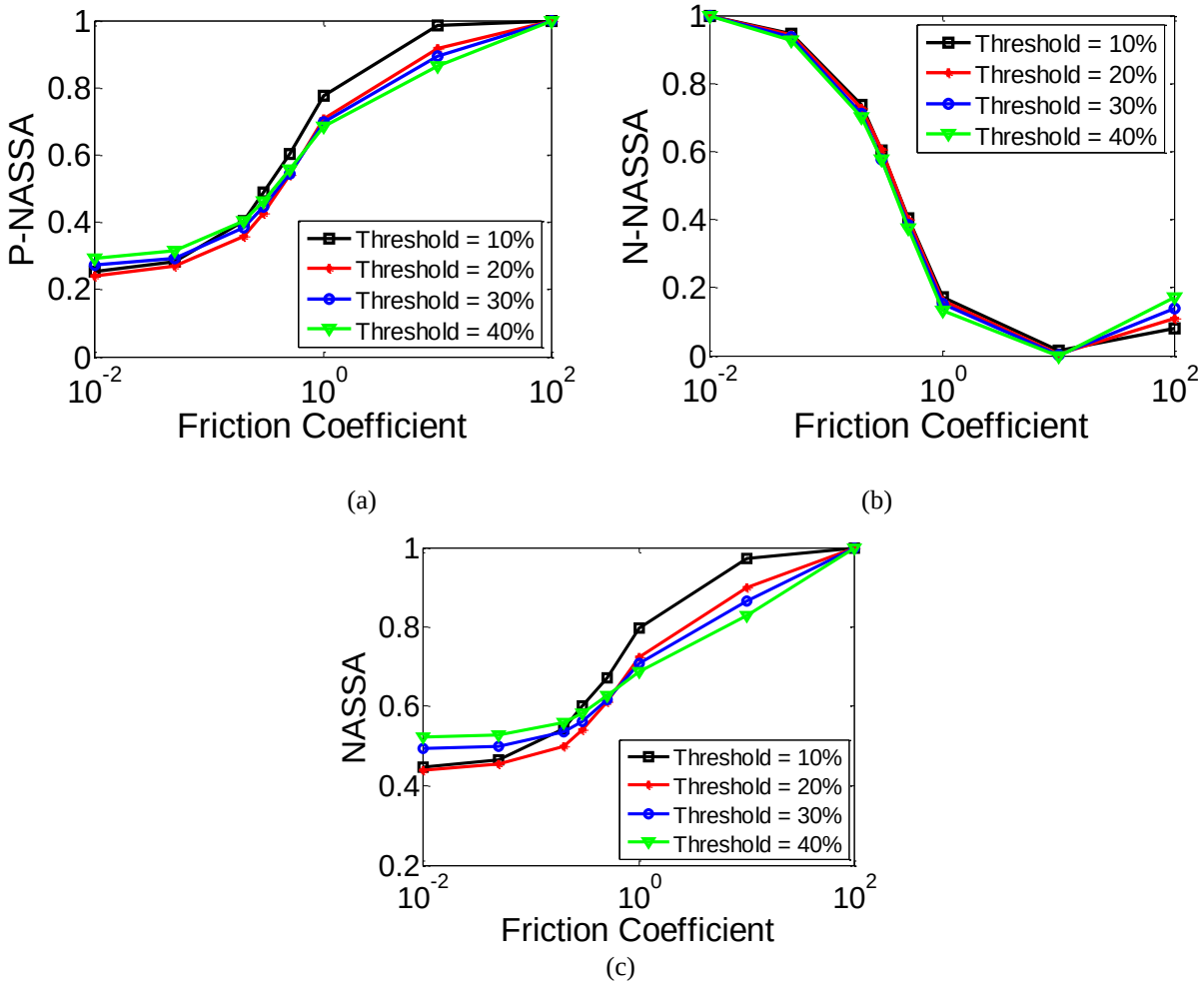

Figure 3.10 Plots depicting variations in the normalized axial-shear strain area (NASSA) for ellipsoidal inclusions for different threshold values. Plot (a) presents the positive component (P-NASSA), while (b) presents the negative component (N-NASSA) and the overall performance (NASSA) is shown in (c).

The difference in the axial-shear strain patterns when comparing unbound to bound inclusions indicate that features derived from the axial-shear strain images may provide features that would enable classification of breast tumors as benign or malignant based on their bonding information. Apart from the bonding at the interface between the inclusion and background, other parameters that may also affect classification results including the applied deformation, the stiffness contrast, and the inclusion dimensions. The impacts of most of these parameters are incorporated by normalizations to obtain features that are only sensitive to the bonding between the inclusion and background. The normalized axial-shear strain area (NASSA) was obtained as follows. Firstly, we set a threshold to segment the axial-shear strain images. Secondly, we found the region in axial-shear strain image with magnitude larger than the threshold. Finally, normalize the area obtained in step 2 to the inclusion area. Four different thresholds ranging from 10% to 40% (of the applied deformation) at steps of 10% were utilized to evaluate the performance of this threshold on tumor classification. Results are shown in Figure 3.10. The performance of the positive component (P-NASSA, Figure 3.10 (a)), negative component (N-NASSA, Figure 3.10 (b)) and overall normalized axial-shear strain areas (NASSA, Figure 3.10 (c)) are shown in these figures. Both the P-NASSA and NASSA features present lower values for unbound inclusions, and the normalized area feature value increases significantly for firmly bound inclusion interfaces compared to unbound interface. The N-NASSA feature values decrease with increases in the friction coefficient values of the contact interface between the inclusion and background. Thirdly, although the variation in the N-NASSA value is large, its contribution to the overall area is smaller than P-NASSA. With an increase in the friction coefficient value from 0.01 to the firmly bound condition, P-NASSA values increase from around 0.2 to 1, which is larger than the difference obtained using NASSA features (0.4 - 1).

Thus the discrimination ability of P-NASSA may be larger than that obtained using NASSA. However, it is also more sensitive to the inclusion position as shown in the previous axial-shear strain images. We also see that lower thresholds provide improved discrimination at the cost of increased noise in the shear strain features.

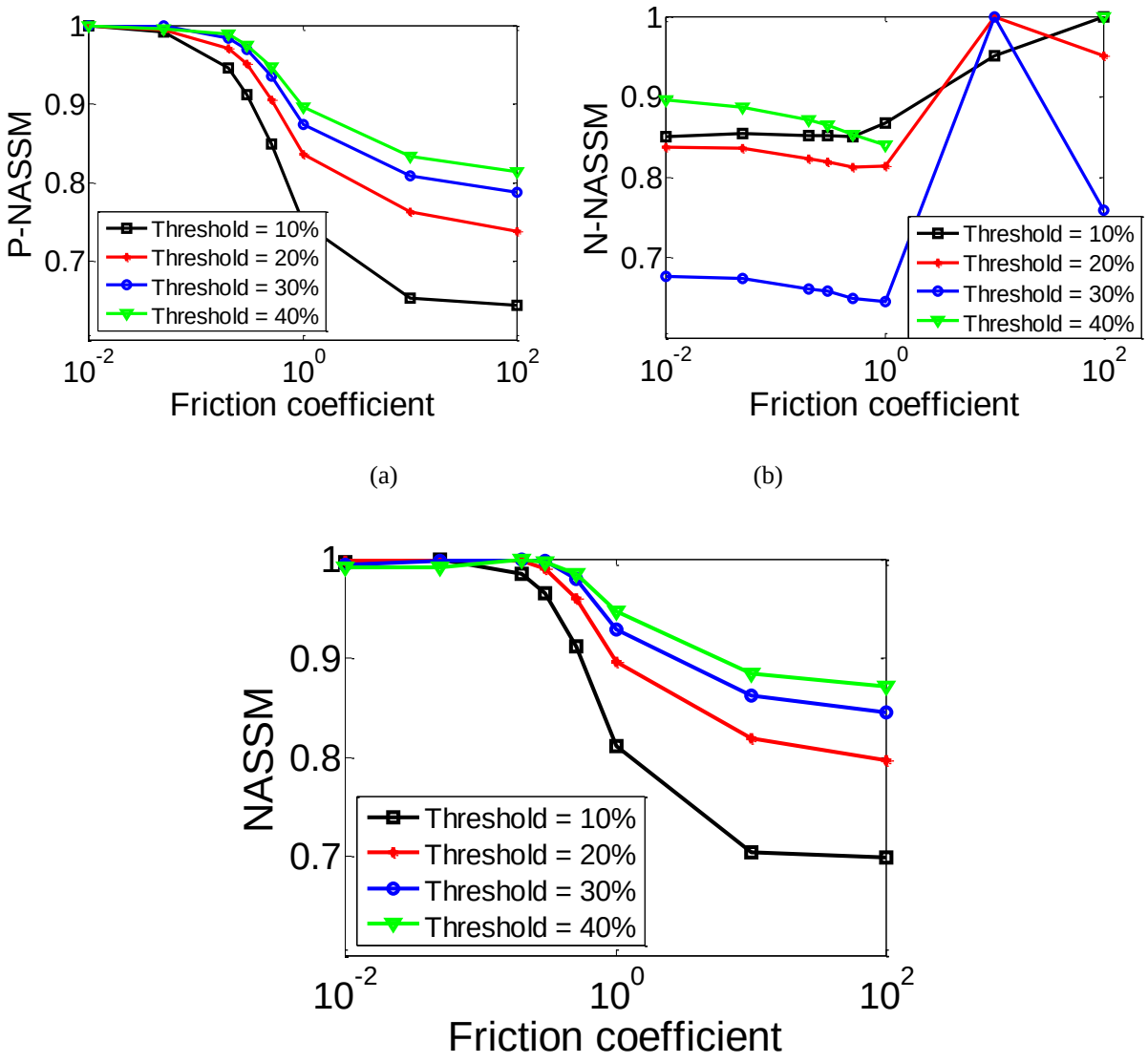

Figure 3.11 Plots depicting variations in the normalized axial-shear strain magnitude (NASSM) for ellipsoidal inclusions for different threshold values. Plot (a) presents the positive component (P-NASSM), (b) presents the negative component (N-NASSM) and the overall performance is shown in (c).

The discrimination performance using the normalized magnitude value of axial-shear strain images (NASSM) for tumor classification is also shown in Figure 3.11. Note that both NASSM and its positive component exhibit larger values with saturation for unbound inclusions, and these values decrease with an increase in the friction coefficient for firmly bound inclusions. Lower threshold provide improved discrimination, however, lower thresholds may also induce more noise artifacts in *in-vivo* studies. NASSM feature values decrease from 1 to 0.7 as the friction coefficient values increase, while NASSA feature values increase from around 0.4 to 1 for the same changes. Thus the discrimination feasibility of using magnitude features derived from axial-shear strain images is lower than using normalized area features.

In general, lower thresholds provide improved discrimination at the cost of increased noise in the shear strain features. Thus a 20% threshold value is selected for further analysis in our study. Compared to the normalized magnitude feature, the normalized area (NASSA) feature provides better discrimination. Although the positive component of NASSA also indicates the feasibility to differentiate benign from malignant breast masses, it is sensitive to the mass position. Asymmetric inclusions will also introduce large “fill in” artifacts with the inclusion orientation angle or direction to the applied deformation. In addition, as demonstrated in Figure. 3.5, the variation in the “fill in” artifacts was also related to the angular position of the mass relative to the applied deformation direction. Thus in our study we choose the overall normalized area i.e. NASSA or NFSSA instead of positive or negative components of these features for further evaluation.

Chapter 4:

Comparison of Axial-Shear and Full-Shear Strain Imaging

4.1 Introduction

Shear strain imaging has been shown to provide new and additional information, as well as novel features derived from this information, that can be utilized to differentiate benign breast masses (unbound) from malignant masses (bound) [22, 72, 80, 122]. The full-shear strain component includes contributions from both axial-shear and lateral-shear due to the applied deformation. However, many investigators utilize only the axial component of the estimated local displacements to generate axial-shear strain images [20, 123-124], while ignoring the contributions of the lateral-shear component [72, 80, 122]. This represents a practical solution since estimation of lateral displacements from radiofrequency (RF) data acquired along the 0^o insonification or backscatter direction can be noisy, leading to noise artifacts in the shear strain image. Our laboratory has developed approaches that utilize beam-steering of a linear array transducer to estimate both axial and lateral displacements in response to an applied deformation. These methods improve the feasibility of obtaining the full shear strain component [76, 129-130].

In this chapter, we first use simulation models built using the finite element analysis (FEA) software applied in Chapter 3 to evaluate both the normalized axial-shear strain area (NASSA) and the normalized full-shear strain area (NFSSA) features exhibited by different inclusion

shapes (spherical and ellipsoidal masses). Changes in the NASSA and NFSSA feature values for these inclusion shapes are presented for variations in the friction coefficient modeling the attachment of the mass to background tissue [125]. Different mass dimensions characterized by variations in the major (a) and minor (b) axes of the mass were used. Different stiffness ratios, applied deformation, and orientations of the mass with the background tissue are also studied. Simulation results are then corroborated using experimental TM phantoms with ellipsoidal masses.

4.2 Tissue Mimicking (TM) Phantom Corroboration

Four single-inclusion TM phantoms each with a single ellipsoidal inclusion were studied to corroborate the mass differentiation performance between the axial-shear and full-shear features. An ellipsoidal mass with dimensions ($19\times14\times14$) mm was embedded within the center of a uniform cubic background with dimensions ($80\times80\times80$) mm for each phantom. The selection of the ellipsoidal mass dimensions was based on mass dimensions reported in *in-vivo* studies. The acoustic and elastic properties of the TM materials used in the phantom and the phantom production procedure have been previously described in Madsen et al. [131-132]. The Young's modulus values for the various materials in the phantoms were obtained using dynamic mechanical testing *via* an EnduraTEC ELF 3220 (Bose Corporation, EnduraTEC Systems Group, Minnetonka, MN). The Young's modulus values and contrasts (ratio of Young's moduli between the mass and background) are shown in Table 4.1.

Table 4.1 Young's Modulus values of the TM phantom materials and their respective Modulus contrasts.

Phantom No.	**Background dimension (mm)**	**Inclusion dimension (mm)**	**Angle**	**Bound/ Unbound**	**Young's Modulus (I, kPa)**	**Young's Modulus (B, kPa)**	**Contrast (I/B)**
1	80×80×80	19×14×14	0^0/ 90^0	Unbound Benign	48.0	11.3	4.2
2	80×80×80	19×14×14	0^0/ 90^0	Bound Malignant	48.0	11.3	4.2
3	80×80×80	19×14×14	30^0/ 60^0	Unbound Benign	58.7	18.2	3.2
4	80×80×80	19×14×14	30^0/ 60^0	Bound Malignant	58.7	18.2	3.2

The ellipsoidal masses were positioned at the center of the cube shaped background material. For the phantoms with representations that mimic benign ellipsoidal masses, a layer of petroleum jelly was applied around the masses before they were embedded in the uniformly elastic TM background. On the other hand, for the ellipsoidal masses that mimic malignant tumors, infiltration of the masses into the background was assured by "gluing" the masses to the previously congealed surrounding background material with molten TM background material. The phantoms with unbound ellipsoids (Phantoms 1 and 3) simulate a benign tumor mass, with symmetrically and asymmetrically oriented masses having stiffness values that are 4.2 and 3.2 times greater than the background material, respectively. Phantoms 2 and 4 also have a modulus contrast of 4.2 and 3.2, respectively, with respect to the background TM material. Application of the quasi-static deformation on different surfaces of the cubical phantom provides different relative angles of the major-axis to the applied deformation surface. Thus, for the ellipsoidal mass in the symmetrical phantoms (Phantom 1 where the ellipsoid was bound to the background material, representing a cancer, and Phantom 2 where the ellipsoid was not bound to the

background material, representing a benign tumor), we evaluate shear strain patterns obtained along both the 0^o and 90^o orientation of the mass with respect to the background. In a similar manner, for the phantoms with the asymmetrical masses, we evaluate shear strain patterns for both 30^o and 60^o orientations of the major axis of the mass with respective to the background (Phantom 3 where the ellipsoid was bound to the background material and Phantom 4 where the ellipsoid was not bound to the background material).

TM phantoms were scanned using a Siemens ACUSON S2000 real-time clinical scanner (Siemens Ultrasound, Mountain View, CA) equipped with a VFX 9L4 linear-array transducer operating at a 6 MHz center frequency. A single transmit focal zone was selected at a depth of 40 mm. RF data were acquired at a 40 MHz sampling frequency. The transducer was held in a motion controlled stage and embedded within a compression plate to provide a uniform quasi-static deformation to the top surface of the phantom. A quasi-static deformation was then applied to the top surface of the phantom. In order to estimate lateral displacements, beam-steering to obtain angular RF data ranging from -15^o to 15^o in increments of 1^o was applied and RF data were acquired. Beam steered pre- and post-deformation RF data were acquired before and after a deformation of 1% of the phantom height (0.8 mm) which was aided by a positional stage as illustrated in Figure 4.1. A plate larger than the TM phantom surface was used to provide uniform deformation over the entire TM phantom.

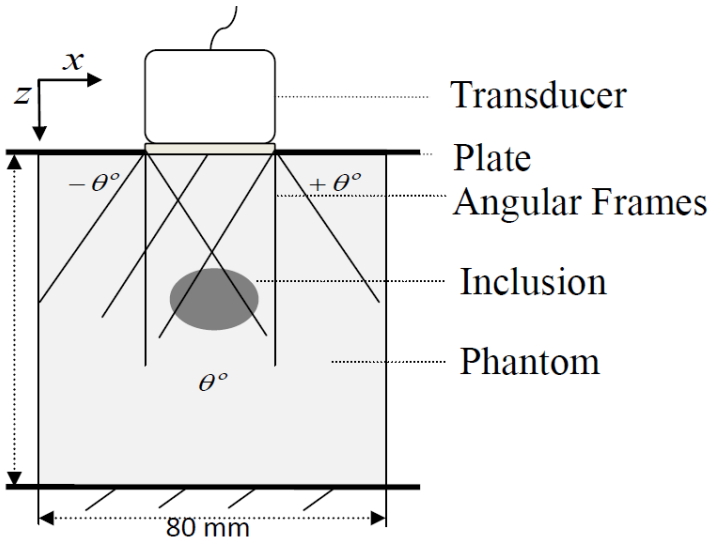

Figure 4.1 Schematic diagram of RF data acquisition using a linear array transducer with beam steering. Note that z represents the direction of the applied deformation, also referred to as the axial direction, and x represents the lateral direction. The beam steered angle for insonification is varied from $-\theta^o$ to $+\theta^o$. A plate larger than the phantom surface is placed on top of the phantom to provide smooth, uniform deformation across the top surface of the phantom.

4.3 Displacement Estimation

Angular displacements (displacement along each beam direction) were estimated from pre- and post- deformation RF data pairs for each beam steering angle using a 1D cross-correlation algorithm with 2D tracking of the displacement [3]. 1D cross-correlation was utilized for this analysis, since two-dimensional (2D) cross-correlation blocks have to be parallelogram shaped with appropriate angles for the angular data sets. Efficient approaches to process angular data sets with 2D processing blocks were developed later and will be discussed in Chapter 5. Angular displacements for each beam direction were then separated into both axial- and lateral displacement components. Median filtering was used to remove outliers in the angular displacement estimates. Only displacement estimates with a normalized cross correlation coefficient value greater than 0.75 were used in the least squares strain estimation. A window

size of 3 mm along with a 75% overlap was used to perform displacement estimation. However, since angular displacements were estimated along each beam steering angle, they have different pixel grid locations. In order to make the angular displacement vectors amenable for image registration, they were interpolated onto the zero-angle spatial grid using bilinear interpolation. The axial- and lateral- displacement components were then estimated from the angular displacements using a least-squares approach previously described by Techavipoo et al. and Rao et al. [8-9].

Let $d_z(i)$ and $z(i)$ be the displacement $d_z(i) = sz(i) + n$ and spatial depth at the i^{th} point along the axial direction, with strain parameter s and noise parameter n. The parameter s is the slope or the local strain of the linear model, which is estimated from the slope of the best fit line through N consecutive displacement. Thus the matrix and its least squares solution are given by Equation 4.1.

$$\bar{d} = A\bar{\theta}, \quad \begin{bmatrix} d_z(1) \\ \vdots \\ d_z(N) \end{bmatrix} = \begin{bmatrix} Z(1) & 1 \\ \vdots & \vdots \\ Z(N) & N \end{bmatrix} \begin{bmatrix} s \\ n \end{bmatrix} \tag{4.1}$$

where the least squares solution is: $\hat{\bar{\theta}} = \begin{bmatrix} \hat{s} \\ \hat{n} \end{bmatrix} = (A^T A)^{-1} A^T \bar{d}$

Note that when N equals to 2, the least squares estimator is similar to a gradient operator. A larger value of N will reduce spatial resolution by blurring edges of regions in generating the strain or shear strain images. In general, a smaller N (≤ 8) is recommended. A 1D processing window size of 3 mm was used to obtain displacement estimates [122]. Axial- and lateral displacement vector images obtained from RF data acquired from the four TM phantoms are shown in Figure 4.2.

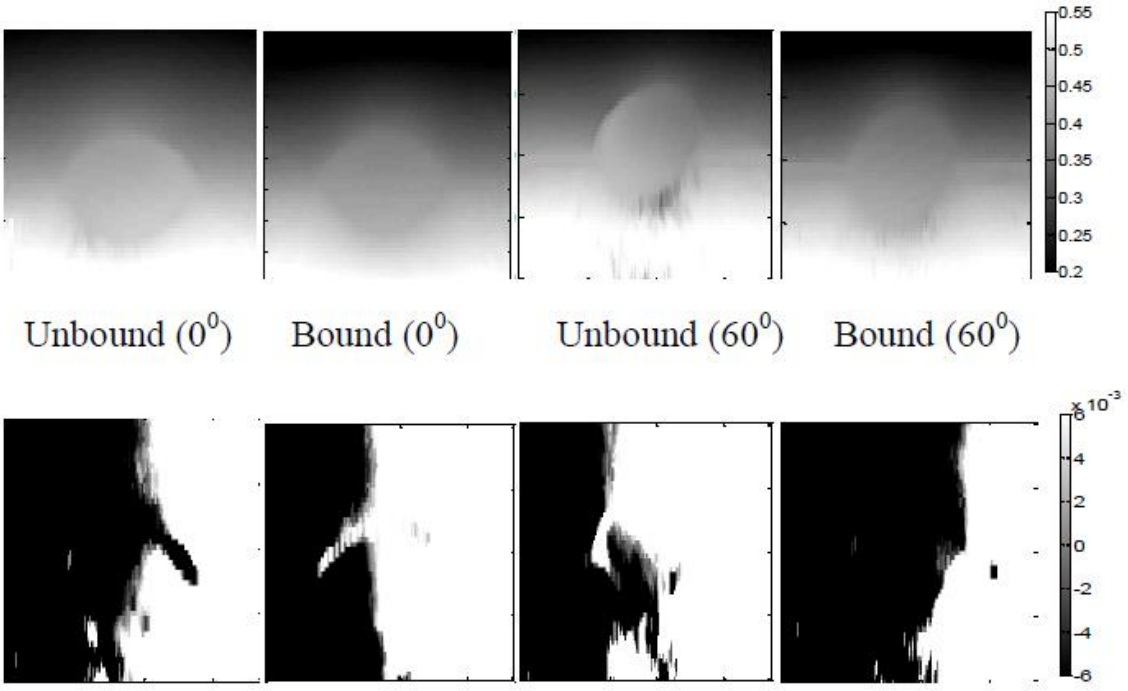

Figure 4.2 Axial (top row) and lateral (bottom row) displacement vector images obtained from TM phantom experiments using beam steered data and 1D processing of the echo signals. The ellipsoidal inclusions in the TM phantoms are oriented at an angle of 0^o and 60^o to the applied deformation. The colorbars for the displacement vectors are in millimeters.

As shown in Figure 4.2, using 1D cross-correlation analysis we were able to track the inclusion boundary above the phantom center (40mm) along the axial direction. However, tracking performance decreased with increased depth due to increased attenuation, especially in phantoms with asymmetrical lesions. The lateral displacement estimates are noisier when compared to the axial displacement vector.

4.4 Normal and Shear Strain Tensor Estimation and Normalization

Axial- and lateral- displacements interpolated to the zero-angle grid as shown in Figure 4.2, were utilized to calculate the axial-strain, lateral-strain, axial-shear and full-shear strain tensors for comparison. Both axial and lateral strain images obtained from the four phantoms are shown

in Figure 4.3. The TM phantom results exhibit noise artifacts near the bottom of the ellipsoidal masses due to lower signal-to-noise ratios (SNR) caused by attenuation. 1D tracking failed to accurately track the deformation beyond the phantom center (>40 mm). This is particularly evident in the asymmetrical phantom. The 1D tracking algorithm produces displacement and strain tensor images with increased noise artifacts along the lateral direction.

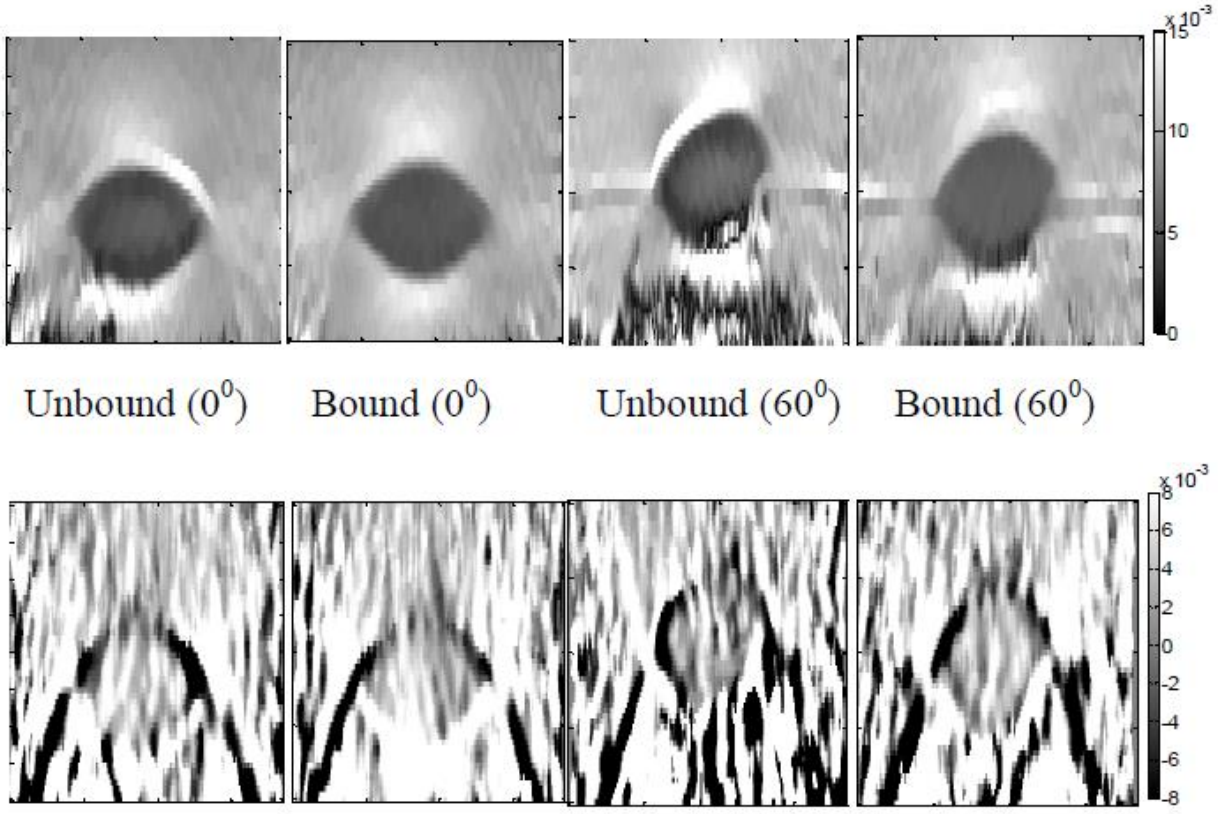

Figure 4.3 Axial (top row) and lateral strain (bottom row) tensor images of the four TM phantoms with ellipsoidal inclusions oriented at an angle of 0^o and 60^o respectively, to the applied deformation for different bonding condition. The 0.01 value on the colorbar represents a 1% strain.

The shear strain (or full shear strain) and the axial-shear strain tensor within the ultrasound scan plane was presented in Chapter 2, Equations 2.1 and 2.2. The shear strain tensor estimators were further filtered by an adaptive median filter. The axial-shear strain tensor was filtered by a filter of size 9×5 pixels. The lateral-shear strain tensor was filtered by a filter of size 5×9

pixels. In order to utilize the shear strain area feature, we first have to normalize the shear strain for performing comparisons over different mass dimensions that vary across patients and under different scanning conditions where the applied deformations may also vary. The stiffness ratio or contrast between the mass and background tissue was another factor utilized for normalization of the shear strain area. Normalized axial-shear strain regions that were first reported by Thitaikumar et al. [6] utilize mass dimensions or areas estimated from ultrasound B-mode images, which can be subjective and depend significantly on the operator's expertise. Stravos [15] reports that most fibroadenomas are visualized as isoechoic while two-thirds of the malignant masses appear as hypoechoic masses on ultrasound B-mode images. In our shear strain area normalizations, coined NASSA for axial-shear in Xu et al. [7], and NFSSA for the full-shear strain area, we utilize mass dimensions estimated from the axial-strain image, where they are clearly visualized and can be obtained using automated segmentation approaches [16-18]. The previously reported normalized shear strain area feature however, included shear strain regions that could occur both within and outside the breast mass [6-7]. To further differentiate shear strain patterns, those that occur outside the masses (OM) are denoted as NASSA_OM and those within masses (IM) were denoted by NASSA_IM as shown in Figure 4.4. The normalized shear strain patterns shown in Figure 4.4 were obtained using FEA simulations for unbound masses. Normalized shear strain areas visualized within breast masses, denoted by NASSA_IM was previously described as "fill-in" by ThitaiKumar et al. [19-20]. They have also reported that the "fill-in" [19-20] depends on the mass orientation, with larger values obtained for unbound masses oriented at an angle (asymmetric) to the applied deformation.

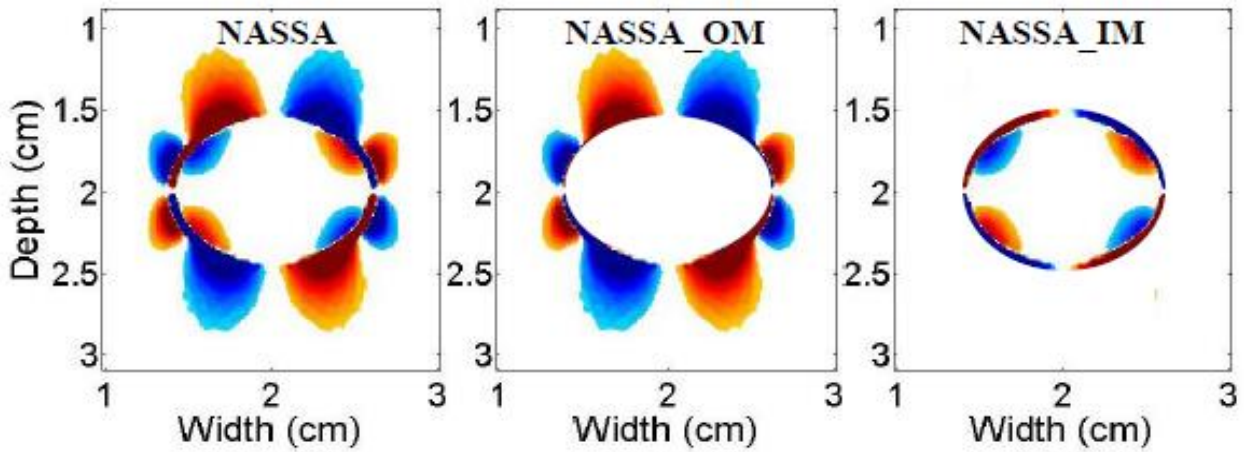

(a) (b) (c)

Figure 4.4 Shear strain area mappings demonstrating the region mapped using the normalized axial shear strain area (NASSA) (a) The normalized shear strain area outside the mass (NASSA_OM) (b) and normalized shear strain area inside the mass (NASSA_IM) (c) obtained using FEA simulations for an unbound mass with a friction coefficient of 0.2.

4.5 Comparison of Shear Strain Patterns

Shear strain images shown in Figure 4.5 were obtained from both FEA simulations (a) and TM phantom based experimental results (b). A comparison of the shear strain patterns between axial-shear (top row) and full-shear (bottom row) is presented for ellipsoidal masses. Since the FEA simulations are 2D, a cross-section with an elliptical shape was utilized. Shear strain variations are depicted for friction coefficient values of 0.2 and 10, denoting unbound versus bound masses. Details on phantom construction for the experimental TM phantoms were presented in the previous section 4.4. Observe the distinct variations in the shear strain patterns between the bound and unbound masses. The “halo” (or larger strain value region) around the inclusion for the unbound mass is absent for the bound mass [125]. this concept was described previously in Rao et al. [125] for spherical inclusions under shear deformations. The presence of the “halo” is due to the presence of shearing forces on the inclusion when it is oriented at an angle to the applied deformation, and is another feature that can be used to differentiate between

benign and malignant breast masses. The magnitude of the normalized full-shear strain area patterns are slightly lower than those seen with axial-shear alone. Normalized shear strain area patterns outside the breast masses (NASSA_OM and NFSSA_OM) appear to be larger for the bound mass[124] than for unbound ones. Normalized shear strain areas visualized inside breast masses denoted by NASSA_IM and NFSSA_IM, previously described as "fill-in" [127-128] for the unbound mass are not observed for the bound mass in both simulations and experiments. The negative and positive shear strain area patterns also vary along the contact interface for asymmetric locations of the mass in background tissue. This was also observed in results obtained with the experimental TM phantoms in Figure 3(b). Symmetric shear strain patterns are observed for ellipsoidal inclusions oriented at 0^o to the applied deformation surface as shown in Figure 4.5, which is consistent with the results reported in previous spherical inclusion studies [20, 80, 128, 133].

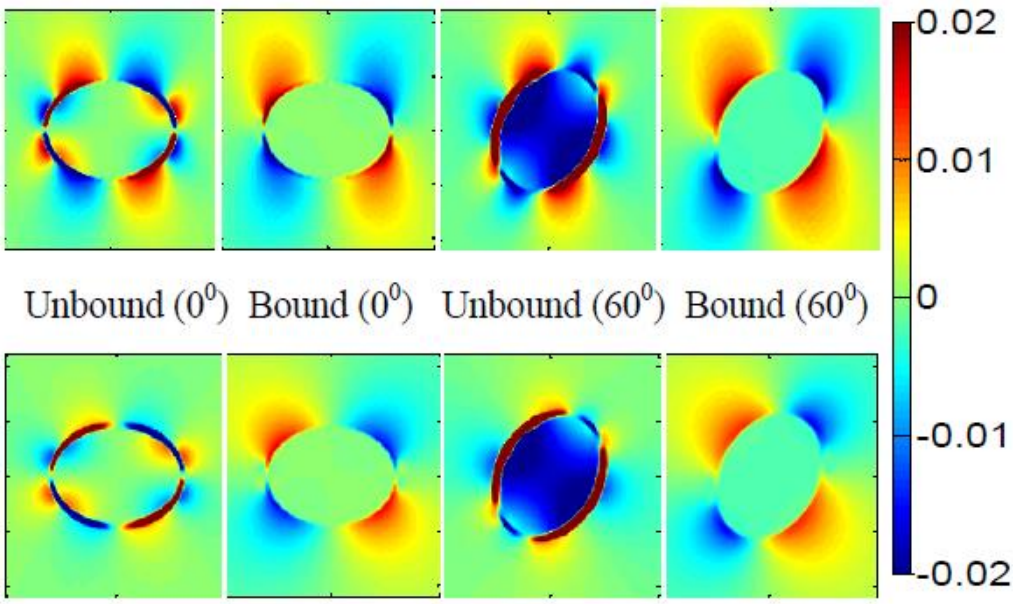

(a)

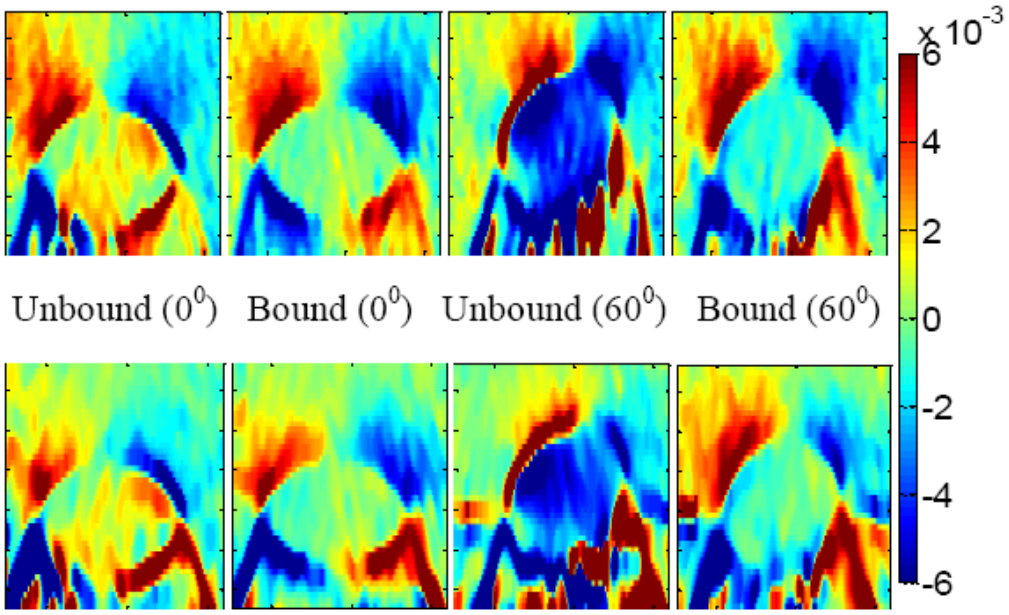

(b)

Figure 4.5 Shear strain images obtained using FEA simulation (a) and corresponding TM phantom experiments (b). Comparison of the shear strain patterns obtained using axial-shear (top row) to that obtained with full-shear (bottom row) for elliptical and ellipsoidal inclusions oriented at an angle of 0^0 and 60^0 to the applied deformation for different bonding conditions are shown.

Shear strain images shown in Figure 4.5(b) represent ellipsoidal TM phantom results oriented at 0^o and 60^o to the applied deformation. Note that the TM phantom results exhibit similar characteristics as those described for the FEA simulation results. However, the TM phantom results include additional noise artifacts around the bottom of the ellipsoidal masses, primarily due to the lower signal-to-noise ratios (SNR) associated with attenuation in the phantom. As shown in Figure 4.5, both axial-shear strain and full-shear strain imaging exhibit lower SNR below the phantom center than in regions above the center. Thus we will only use shear strain estimates above the phantom center ($\leq$ 40 mm) for further feature analysis.

Previous studies based on spherical masses have demonstrated that a threshold set at 20% of the applied deformation provided an optimal value for the NASSA and NFSSA features. Plots of

both the NASSA (Figure 4.6(a)) and NFSSA feature (Figure 4.6(b)) with threshold values ranging from 10% to 40% in increments of 10% are shown in Figure 4.6 for elliptical masses, for friction coefficient ranging from 0.01 to 100. Observe from Figure 4.6, that a threshold of 20% of the applied deformation provides an optimal value for both NASSA and NFSSA features for differentiation between the modeled FEA elliptical inclusions consistent with the previously described results for spherical inclusions. Previously published *in-vivo* results [20, 123] have reported on the use of NASSA features obtained utilizing a threshold level of 20% [20] and 25% [123-124, 127]. In general, lower thresholds provide improved discrimination at the cost of increased noise in the shear strain features. The 20% threshold value is also used in this chapter. Also note from Figure 4.6, NFSSA features provide a better discrimination between lower friction coefficient and high friction coefficient masses when compared to NASSA features.

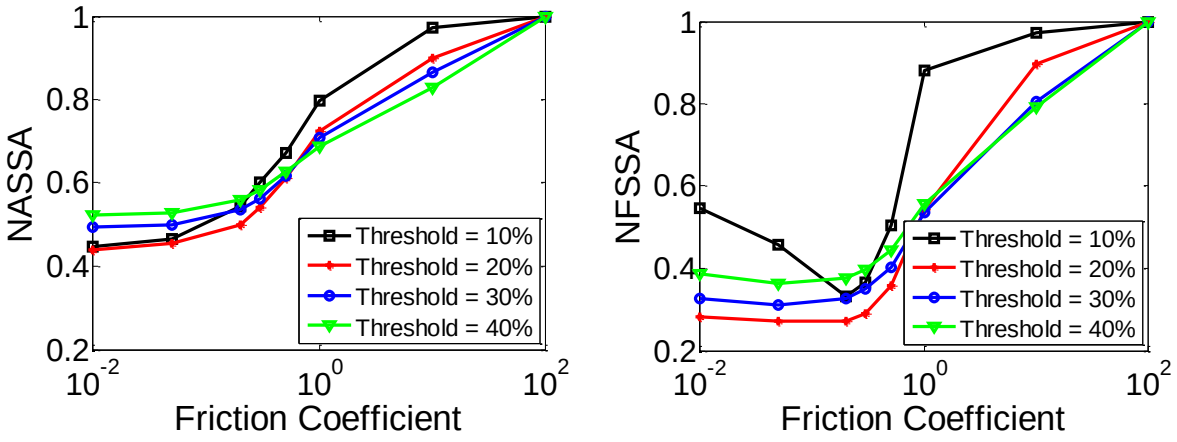

(a) (b)

Figure 4.6 Plots depicting variations in the NASSA and (a) NFSSA (b) for ellipsoidal inclusions for different threshold values.

Variations in the NASSA and NFSSA feature values versus the friction coefficient are shown in Figure 4.7(a) and (b). Results are shown for three different inclusion dimensions,

characterized by the ratio of the minor to major axis (b/a). The inclusion with a b/a value of 1 is a spherical. The NASSA feature value shows the same trend (Figure 4.7 (a)) for inclusions with different b/a. NASSA exhibits a larger variance and lower discrimination than the NFSSA feature shown in Figure 4.7(b). Both features demonstrate low values for unbound inclusions, with the values increasing as the mass become progressively more attached to the background tissue.

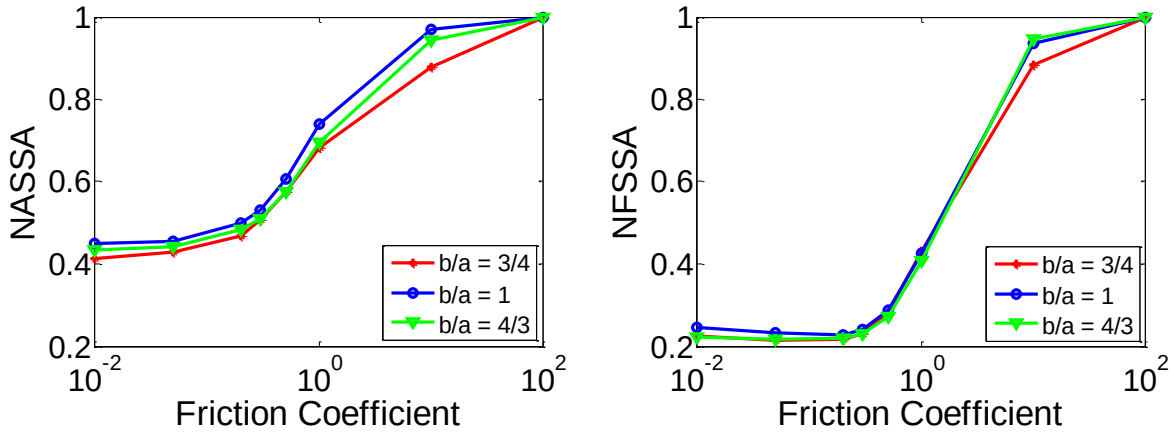

(a) (b)

Figure 4.7 Plots showing variations in the NASSA (a) and NFSSA (b) feature values for ellipsoidal inclusions with different b/a value.

Variations in the feature values for changes in the stiffness contrast between the inclusion and background tissue are shown in Figure 4.8. Three values of the background/inclusion Young's modulus ratio were studied, namely 1:3, 1:5, and 1:10 to evaluate if stiffening of the inclusion would change the shear strain patterns. The Young's modulus of the background tissue was set to 10 kPa in our FEA analysis. Note that these background/inclusion stiffness ratios have similar NASSA and NFSSA feature values, with the results being more consistent for stiffer masses (1:5 and 1:10). Note also that higher stiffness contrast improves discrimination for NFSSA features. Variation in the features due to change in the applied deformation (AD) is

shown in Figure 4.9. Observe that both NASSA and NFSSA feature values with friction coefficient lower than 0.4 are unstable for larger applied deformation (>5%), probably due to increased mass slippage.

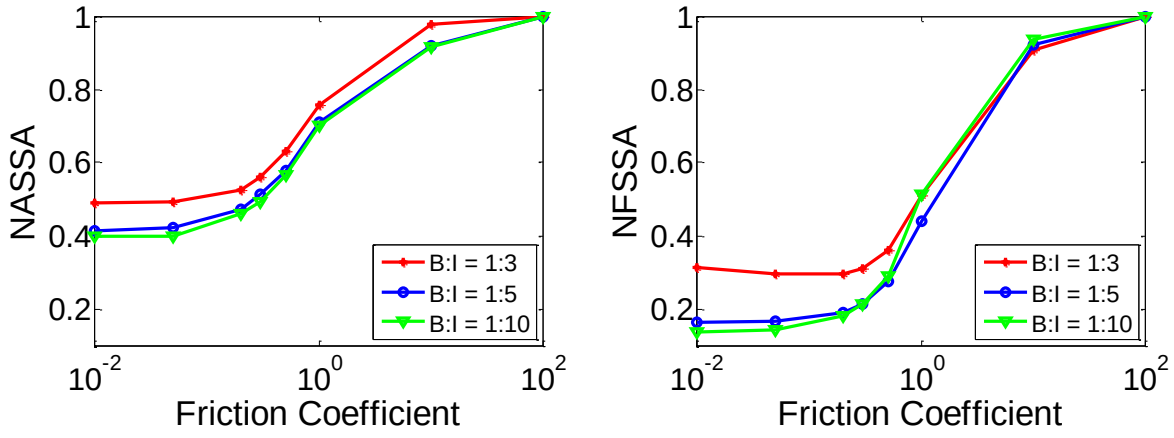

(a) (b)

Figure 4.8 Plots showing the impact of various stiffness ratio values on the NASSA (a) and NFSSA (b) respectively.

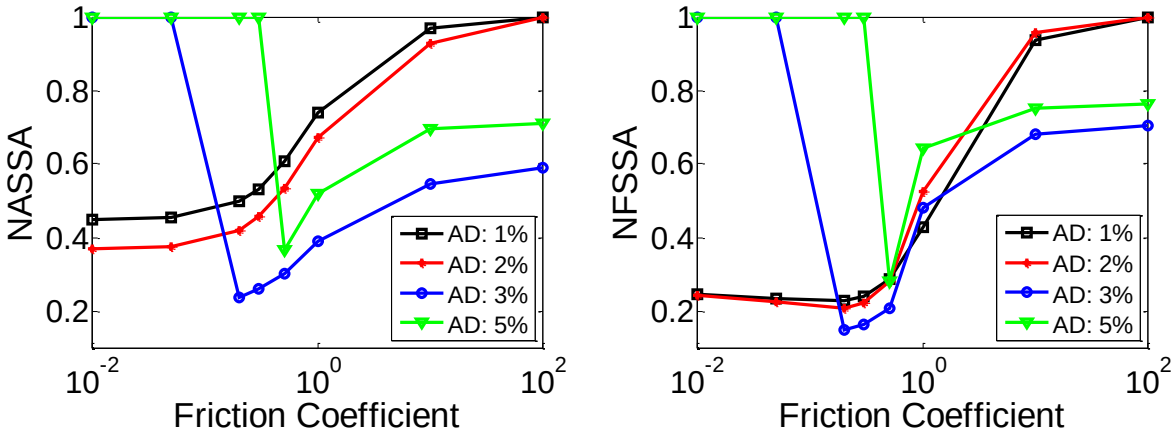

(a) (b)

Figure 4.9 Impact of applied deformation on NASSA (a) and NFSSA (b).

Finally, we evaluate the impact of inclusion orientation with respect to the applied deformation for both bound and unbound masses based on both FEA simulations (Figure 4.10-4.11 (i)) and experimental TM phantom results (Figs. 4.10-4.11 (ii)). For FEA simulation, we

evaluate the impact of asymmetric inclusion orientation by rotating the elliptical inclusion from 0^o to 90^o in steps of 10^o (relative to the top surface of the model where the deformation is applied), assigning the unbound inclusions with a 0.5 friction coefficient value and gluing the contact interface of the bound model together. For the TM phantom, both the NASSA feature extracted from half of the axial-shear strain image (above the phantom center ($\leq$ 40mm)) and the NFSSA feature extracted from the same region were obtained utilizing beam-steering from $\pm 15^0$. Results are presented for the NASSA and NFSSA feature values for ellipsoidal inclusions oriented at 0^o, 30^o, 60^o and 90^o respectively for both the bound and unbound phantoms. Both the feature values, namely NASSA and NFSSA present values that are larger along all orientation angles for bound inclusions than for unbound inclusions. Also note that both the NASSA and NFSSA values vary significantly with orientation angle for the unbound mass. The best discrimination was obtained at mass orientations of 0^o and 90^o respectively. Since only half of the shear strain imaging of TM phantom ($\leq$ 40mm) are used for the feature study, both NASSA and NFSSA TM phantom feature values are about half of their FEA simulation results. In addition, the overall NFSSA feature values are lower than NASSA feature values both for FEA simulation results (i) and TM phantom results (ii).

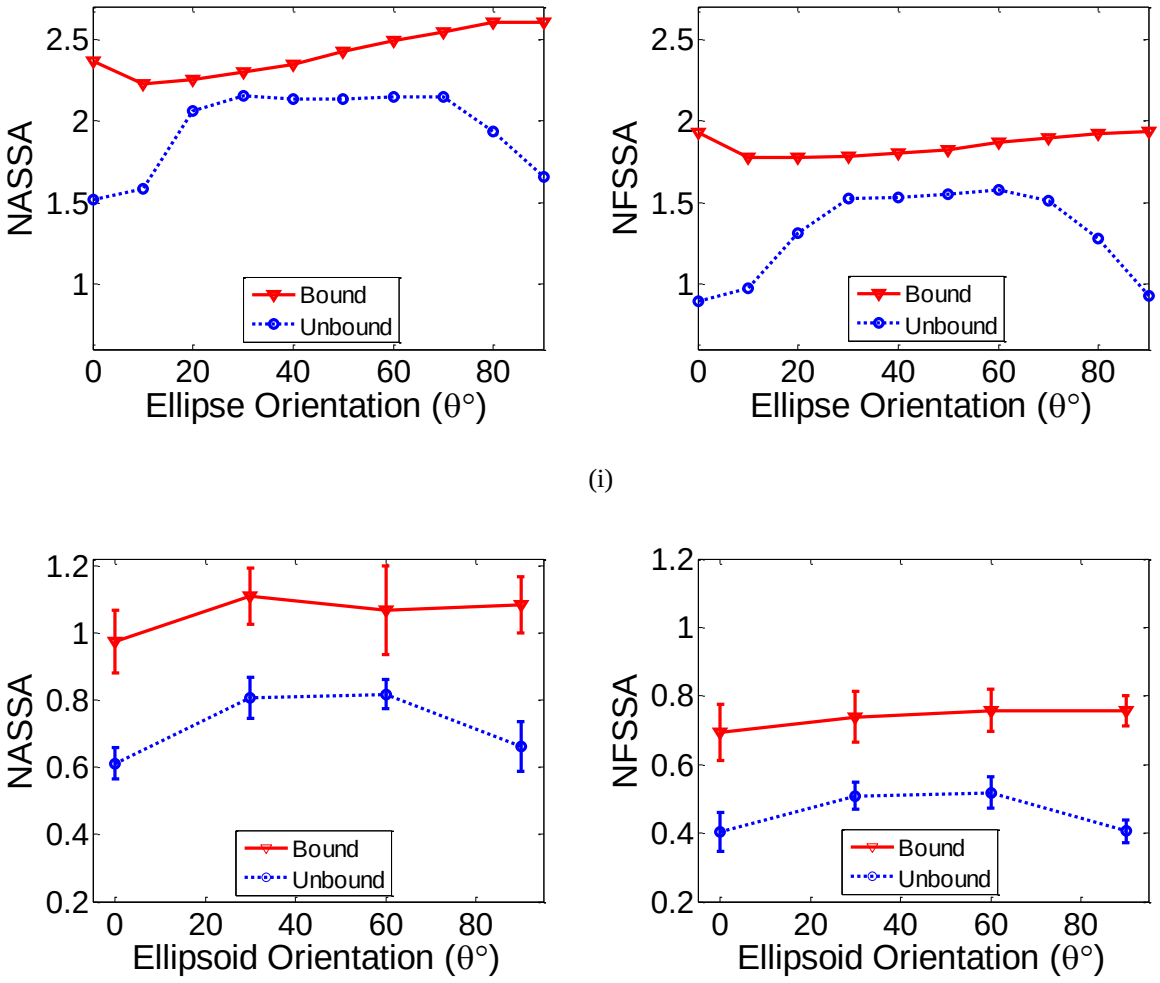

Figure 4.10 Plots demonstrating the impact of inclusion orientation to the applied deformation for both FEA simulations (top row or i) and experimental TM phantom results (bottom row or ii). Column (a) demonstrates the variations in the NASSA feature values while column (b) presents the same for the NFSSA feature values.

Discrimination between bound and unbound conditions was worse when the mass was oriented at an angle of 20^{o} to 70^{o}. This is due to the increased shear strains within these masses [127-128]. One way to circumvent this would be to apply deformations with the mass oriented at 0^{o} or 90^{o} to the applied deformation. In addition, the NFSSA feature is more stable and constant for the bound inclusions than the NASSA feature, as observed in the simulation results. However, as shown in Figure 4.10 (ii), this was not as obvious for phantom results, likely due to

increased noise artifacts. Also note that the trend of descending from 0^o to 10^o and ascending from 10^o to 90^o for bound FEA simulation results are not obvious in the experimental results. This may be is partly due to the limited angles of TM phantom used for this study. Some of these artifacts are due to reduced averaging at the sides of the inclusion due to the reduced coverage with beam steered data collection, and thus increased noise. The error bars plotted in Figure 4.10-4.11 (ii) represent the standard deviation of the mean feature value (NASSA and NFSSA) estimated from ten independent sets of RF data acquired with the TM phantoms. Note that the standard deviation for the features derived from the unbound phantom was smaller than that for the bound masses. Since shear strain patterns within the masses only exist for unbound or loosely bound masses, and specifically for asymmetric positioning of the masses, we plotted the NASSA_OM and NFSSA_OM feature values in Figure 4.11. NASSA_OM and NFSSA_OM were obtained by excluding any shear strain patterns within the inclusion or mass. As illustrated in Figure 4.11, without accounting for shear strains within masses, both the NASSA_OM and NFSSA_OM features provide significantly better differentiation between benign and malignant masses for all asymmetric orientations of the mass with respect to the applied deformation. In addition, the NFSSA feature was more stable for unbound masses as shown in Figure 4.11 (b). Further analysis and additional features may be required to completely characterize masses that are oriented at an angle to the applied deformation.

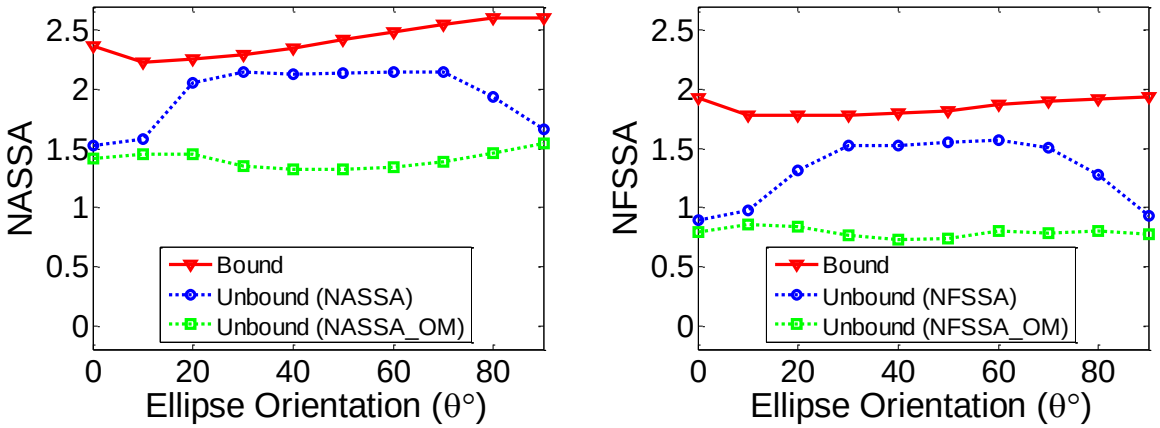

(i)

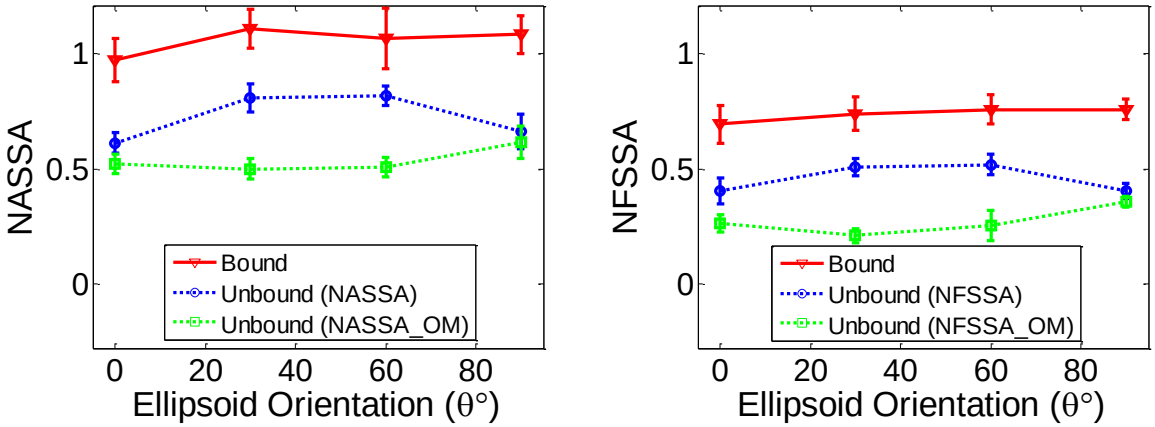

(ii)

(a) (b)

Figure 4.11 Plots demonstrating the impact of inclusion orientation to the applied deformation with and without shearing strains within the inclusion for both FEA simulation (i) and experimental TM phantom results (ii). Column (a) demonstrates the variations in the NASSA feature values while column (b) presents NFSSA feature values.

4.6 Discussion of NASSA and NFSSA Results

In this chapter, we show the feasibility of utilizing both the normalized axial-shear strain area (NASSA) and the normalized full-shear strain area (NFSSA) feature to differentiate between

benign and malignant breast masses based on their attachment to background tissue. Differentiation between bound or unbound masses was not affected by the lesion size or shape for symmetric positioning or location of the mass within the background. On the other hand, for unbound masses shear strains within the inclusion were enhanced, especially with asymmetric positioning of masses within the background. For asymmetric masses these shear strains within the inclusion introduce errors that reduce the ability of both the NASSA and NFSSA features to differentiate between firmly and loosely attached masses as shown in Figure 4.11. Orientation of the mass at 0^o or 90^o to the applied deformation for data acquisition on patients would be an obvious solution, as supported by results in Figure 4.11. Another option as illustrated in this chapter would be to exclude shear strains within the inclusion as is done with the NASSA_OM and the NFSSA_OM features. Mass differentiation and classification for bound and unbound masses for all orientations with respect to the applied deformation was improved significantly by excluding shearing strains within the interior of the inclusion. However, we have to keep in mind that the shearing strains within an inclusion could be an indicator of necrotic regions within a tumor that could be significantly stiffer than the surrounding tissue, or perhaps an indicator of multiple distributed masses [134].

Another artifact source were the tracking errors present with 1D cross correlation. These introduce signal de-correlation errors, observed at increased depths in the phantom (for depths > 5 cm in Figure4.5), and were attributed to lower ultrasound SNR associated with the echo signal and caused by attenuation. The reduced SNR introduces noise artifacts into both the NASSA and NFSSA features, reducing their ability to differentiate benign from malignant breast masses. Improved displacement tracking and estimation with 2D kernels, are therefore necessary to estimate angular displacements with better accuracy and spatial resolution.

Results reported in the chapter also indicate that increased mass stiffness improves classification done by the NFSSA feature, when compared to classification with the NASSA feature. This observation is based on a larger difference in the feature values for bound vs. unbound masses, shown in Figure 4.8. In general increased mass stiffness with respect to background tissue improves visualization of shear strains. Finally, Figure 4.9 also indicates that larger applied deformations may introduce instabilities due to mass slippage for both NASSA and NFSSA features for unbound masses.

Chapter 5:

Two Dimensional Tracking on Beam Steered Linear Array Datasets

5.1 Introduction

Beam-steered radiofrequency (RF) data has been utilized previously to estimate both the normal and shear strain tensors within a scan-plane [135]. However, all of the analysis for angular displacement tracking and strain tensor imaging was performed either using 1D cross-correlation analysis of the pre- and post-deformation signals or 2D block tracking with only axial components. There were obtained after a quasi-static deformation. In the previous chapter, we demonstrated the presence of decorrelation noise artifacts associated with the 1D cross-correlation motion tracking method.

In this chapter, we present the use of parallelogram shaped 2D processing blocks for motion tracking. The block varies with beam-steering angle to estimate the complete 2D angular displacement vector under quasi-static deformation [136]. Utilization of the full 2D angular displacement included the orthogonal components (i.e. axial and lateral components) of the displacement vector that were estimated using a least-square compounding approach. The gradient of the axial displacement vector was utilized to estimate axial strain and axial-shear strain tensors. In a similar manner, the lateral displacement vector was used for lateral strain and

---

Material in this chapter was adapted from:

H. Xu and T. Varghese, "Normal and shear strain imaging using 2D deformation tracking on beam steered linear array datasets," *Med Phys*, vol. 40, p. 012902, Jan 2013

lateral-shear strain tensor estimation. Full-shear strain images were then calculated from the axial-shear and lateral-shear strain tensors. The performance of our novel 2D deformation tracking method was compared to the previously utilized 1D deformation tracking method using tissue-mimicking (TM) phantom experiments. Quantitative experimental results obtained from uniform TM phantom using 2D motion tracking demonstrated the significant improvement in the elastographic signal to noise (SNR_e) when compared to 1D tracking. Single inclusion ellipsoidal TM phantoms demonstrated improvements in the elastographic contrast to noise (CNR_e) over that obtained using 1D processing.

5.2 2D Parallelogram Kernel Based Deformation Tracking Algorithm

A uniformly elastic TM phantom with dimensions $(100 \times 100 \times 100)$ mm described in chapter 4 was used to compare strain SNR_e performance between 1D and 2D motion tracking methods for beam-steered data. In addition, four single-inclusion TM phantoms as discussed in chapters 4 were used to evaluate the CNR_e for the two motion tracking approaches.

Beam steered RF data were acquired from -15 ° to 15 ° degrees in increments of 1 ° from both the uniform and ellipsoidal mass phantoms described in chapter 4. Thus, 31 pairs of RF beam steered data frames were acquired before and after an applied deformation. Angular displacement vectors (along and perpendicular to the beam direction) at each beam steered angle (θ^o) were estimated from pre- and post-deformation echo signals using parallelogram shaped 2D cross-correlation based deformation tracking. The parallelogram shaped kernel dimensions were 0.385 mm along the beam direction ×3 A-lines, with a 75% overlap along the beam direction and

one A-line overlap in the lateral direction. The angular displacement pairs were estimated from a Cartesian spatial grid obtained for each beam steered angle.

In order to make the angular displacement obtained under each beam steering angle comparable and to prepare them for image registration, the estimated angular displacement vectors were first interpolated using spline interpolation along each beam steered angle. A 1D median filter was applied to remove noise from angular displacement vectors. Then these angular displacement vectors from each angular Cartesian spatial grid were transformed and registered into the Cartesian spatial grid defined for the $0\,^{\circ}$ RF data. A geometrical shear transformation, defined in Eq. (6.1) was utilized to perform the transformation to the $0\,^{\circ}$ Cartesian grid. Thus,

$$\begin{aligned} z &= zt_{\theta} \\ x &= \tan(\theta) \times zt_{\theta} + xt_{\theta} \end{aligned} \tag{5.1}$$

where θ represents each beam steering angle ranging from $-15\,^{\circ}$ to $15\,^{\circ}$ degrees, zt_{θ} and xt_{θ} represent the axial and lateral coordinates of each beam steered Cartesian spatial grid, and z and x denote the axial and lateral coordinates of the $0\,^{\circ}$ Cartesian spatial grid.

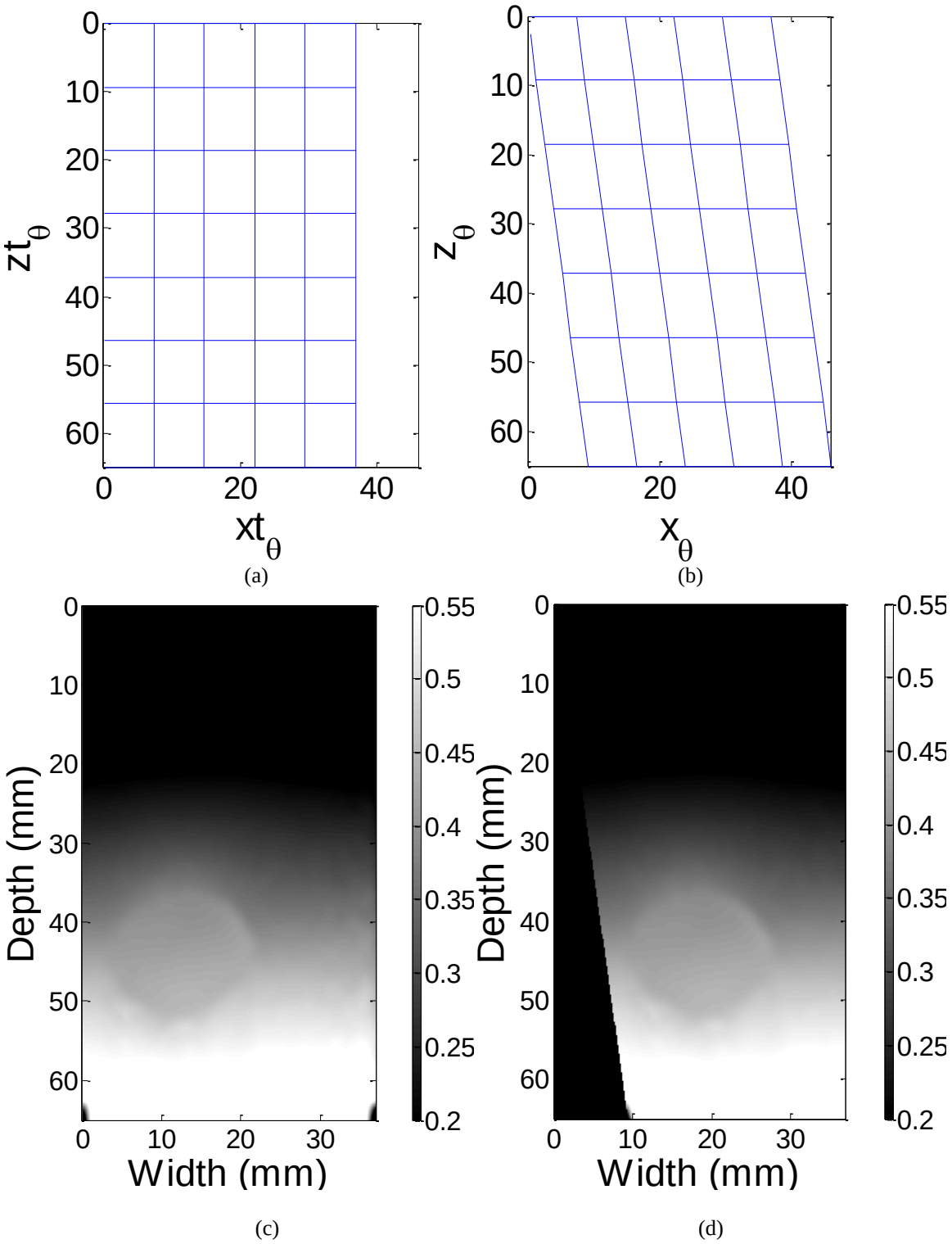

Figure 5.1 Shear transformation for the spatial grid (top), along with the angular displacement vector. The left column shows the spatial grid and angular displacements obtained using a 8^o steered angle, respectively. The right column shows the spatial grid and angular displacement using a 0^o spatial grid.

Comparison between the Cartesian spatial grid obtained for $8°$ and its corresponding shear transformation within the Cartesian spatial grid obtained along the $0°$ direction was shown in Figure 5.1 (a-d), where (a) represents the spatial grid for the $8°$ beam steered angle and (b) represents its corresponding shear geometrical transformation within the spatial grid for the $0°$ coordinate system. Note that a rectangular spatial grid within the steered coordinates was transformed into a parallelogram shape within the $0°$ coordinate system. Based on this spatial grid and shear transformation, both the angular displacement vectors were transferred onto the spatial grid obtained for the $0°$ RF data using a 2D transformation. Figure 5.1 (c-d) shown the angular displacement vector along the beam steered angle ($8°$) for the symmetrical bound ellipsoidal phantom, while Figure 5.1 (c) presents the experimental phantom results obtained within its beam steered coordinates and Figure 5.1 (d) presents its corresponding shear transformation results for the $0°$ coordinates. In a similar manner, all the angular displacement vectors were transferred to the same Cartesian spatial grid using interpolation for each beam steered angle and the 2D geometrical shear transformation.

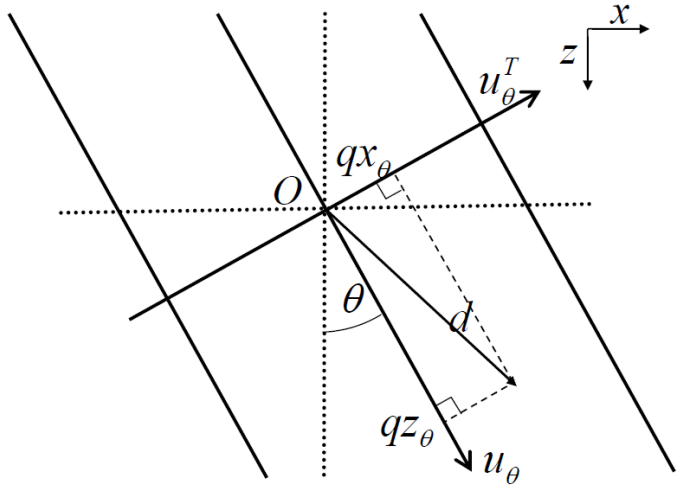

Figure 5.2 Projection of the actual displacement vector $\vec{d}$ at point O, onto unit vectors along $\bar{u}_\theta$ beam steered direction, and u_θ^T which is perpendicular to this direction.

For each point *O* in space from a single beam steered acquisition, its total displacement vector $\vec{d}$ is tracked using 2D motion tracking. This is done both along and perpendicular to the beam steered direction, as shown in Figure 5.2. Assume $\bar{u}_\theta$ to be a unit vector along the beam steered angle θ and $\bar{u}_\theta^T$ to be a unit vector perpendicular to the beam steered direction. Let pz_θ be the projection of the total displacement vector $\vec{d}$ in the beam steered direction and px_θ be its projection onto the unit vector $\bar{u}_\theta^T$ perpendicular to the beam steered direction. Thus the projection can be expressed as the dot product between the total displacement and the projected directional unit vector, as described in Eq. (5.2):

$$\begin{bmatrix} pz_\theta \\ px_\theta \end{bmatrix} = \begin{bmatrix} \vec{d} \cdot \bar{u}_\theta \\ \vec{d} \cdot \bar{u}_\theta^T \end{bmatrix} = \begin{bmatrix} \cos\theta & \sin\theta \\ -\sin\theta & \cos\theta \end{bmatrix} \begin{bmatrix} d_z \\ d_x \end{bmatrix} \tag{5.2}$$

where d_z and d_x represent the component of the displacement vector $\vec{d}$ along the z and x direction respectively, and θ represents the beam steered angle.

All the angular displacement vectors passing through the point *O* were registered onto the zero-angle grid. They were then used to compute the axial and lateral displacement vector using a 2D least squares displacement estimator. The contribution of the lateral angular displacement vector to the actual lateral displacement component was calculated based on each spatial angular displacement, using

$$\bar{q} = A\bar{d} + \bar{n} \tag{5.3}$$

where

$$\bar{q} = \begin{bmatrix} qz_{\theta_1} \\ qz_{\theta_2} \\ \vdots \\ qz_{\theta_m} \\ qx_{\theta_1} \\ qx_{\theta_2} \\ \vdots \\ qx_{\theta_m} \end{bmatrix}, A = \begin{bmatrix} \cos\theta_1 & \sin\theta_1 \\ \cos\theta_2 & \sin\theta_2 \\ \vdots & \vdots \\ \cos\theta_m & \sin\theta_m \\ -\sin\theta_1 & \cos\theta_1 \\ -\sin\theta_2 & \cos\theta_2 \\ \vdots & \vdots \\ -\sin\theta_m & \cos\theta_m \end{bmatrix}, \bar{d} = \begin{bmatrix} d_z \\ d_x \end{bmatrix}, \text{and } \bar{n} = \begin{bmatrix} nz_{\theta_1} \\ nz_{\theta_2} \\ \vdots \\ nz_{\theta_m} \\ nx_{\theta_1} \\ nx_{\theta_2} \\ \vdots \\ nx_{\theta_m} \end{bmatrix}$$

Note that qz_{θ_i} and qx_{θ_i} represent an observation of the displacement vector $\bar{d}$ along and perpendicular to the beam-steered angle θ_i for $i = 1, \ldots, m$, where m denotes the total number of beam steered frames acquired. In Equation (5.3), A represents the transformation matrix that includes contributions due to steering angle θ_i along the clock-wise direction, d_z and d_x represent the axial and lateral displacement vector components (relative to the applied deformation), and nz_{θ_i} and nx_{θ_i} denote the noise contributions in the estimated displacements along and perpendicular to each beam steered angle θ_i.

The least squares solution for the displacement vector was previously described by Techavipoo et al. [135]. This is given by:

$$\tilde{d} = (A^{\mathrm{T}}A)^{-1}A^{\mathrm{T}}\bar{q} \tag{5.4}$$

The normal and shear strain tensors were calculated from the axial and lateral displacement vectors using a least-squares strain estimator [137].

In previous studies, the axial and lateral displacements were estimated from the angular component along the beam-steered direction using a 1D rotational transformation [79, 129] as described in Eq. (5.5). The angular component was estimated either using 1D motion tracking or

2D block matching with only the axial components obtained due to a lower SNR along the lateral angular direction. To study the performance of the 2D parallelogram motion tracking and transformation method, we will present a quantitative analysis on three methods. We will present the results obtained using 2D parallelogram motion tracking with 2D transformation that utilizes both the axial and lateral components of the angular displacement estimated as shown in Eq. (5.2). This will be termed '2D' throughout this chapter, Strain tensor estimation results obtained using only the axial-angular component obtained using 2D tracking with the parallelogram shaped kernels, and using a 1D transformation is presented as '2D_A'. this will be called the 2D axial approximation. Finally, we also present results obtained using 1D motion tracking with a 1D transformation, and this is termed '1D' tracking [73, 79, 129].

$$pz_{\theta} = \vec{d} \cdot \bar{u}_{\theta} = \begin{bmatrix} \cos\theta & \sin\theta \end{bmatrix} \begin{bmatrix} d_z \\ d_x \end{bmatrix} \tag{5.5}$$

where d_z and d_x represent the component of the displacement vector $\vec{d}$ along the z and x direction respectively and θ represents the beam steered angle. The axial and lateral displacement components were estimated from the angular displacement vector.

A 1D 1×5 median filter was applied to the angular displacement vectors before the 1D, 2D and 2D_A transformations. Note that the axial strain tensor *SNRe* and CNR_e mean values improved significantly when compared to results presented in our previous study that utilized a 2D median filter with dimensions 5×5 [21]. The reduction in the *SNRe* was due to the application of a rectangular 2D filter that introduced additional artifacts to the angular displacement vectors. Unlike the 2D displacement vectors along the 0^o co-ordinate plane with small fluctuations between the angular displacement vectors perpendicular to the A-lines, the 2D angular displacements estimated incurred large fluctuations between neighboring A-lines. The

2D median filter, in addition to removing noise spikes also introduced spatial angular distortions in the displacement field which introduced an artifactual increase in the standard deviation of the local strain estimates. The 2D 5×5 median filter was therefore replaced with a 1D 1×5 median filter to reduce noise spikes without adding additional spatial angular distortions to the angular displacement vector field. In order to apply 2D filtering, an adaptive 2D median filter that can be separately applied to each of the beam-steered angular displacement vector fields is required to avoid spatial distortions in the angular displacement vector fields.

5.3 Estimation of *SNRe*, *CNRe* and Strain Contrast

The SNR_e of the strain tensor images obtained for the uniformly elastic phantom using both 1D and 2D deformation tracking were evaluated. In order to study the contributions of the angular displacements to the axial- and lateral displacement vector estimation, we will also present results obtained using only the axial component of the 2D angular displacement vector estimated using 2D tracking; this result is depicted as 2D_A, in the following figures. Thus the 2D transformation used in Eq. (5.3) will resemble a 1D (one column) transformation, which is similar to the transformation matrix presented in previous studies [79, 129].

The SNR_e in the uniformly elastic strain tensor images is defined as [138]:

$$SNR_e = \frac{m}{\sigma} \tag{5.6}$$

where m and σ represents the mean and standard deviation of the strain estimates in the selected region of interest (ROI) respectively.

Ellipsoidal inclusion phantoms were used to estimate the CNR_e and the corresponding stiffness contrast (CN) values. These are defined as follows[139]:

$$CNR_e = \frac{2(m_i - m_b)^2}{(\sigma_i^2 + \sigma_b^2)} \tag{5.7}$$

$$CN = \frac{m_i}{m_b} \tag{5.8}$$

where m_i and m_b represent the mean strain estimated in the selected ROI within the inclusion and background respectively, and σ_i^2 and σ_b^2 denote the corresponding variance within the inclusion and background ROI respectively.

A selected ROI around the focal depth (40 mm) of the axial and lateral strain tensor images were used to compute SNR_e, CNR_e and CN values using both 1D and 2D motion tracking methods. Since the strain tensor image was calculated using angular displacements obtained using independent beam-steered data, the number of angular pixels that contribute to the axial and lateral strain tensor image was the largest in the central triangular region and decreases on either side. The isosceles trapezoidal shaped ROI in the strain tensor image that utilizes all available beam steered contributions during the image registration process was selected for SNR_e analysis. This ROI has a height of 20 mm, a top long edge of 15 mm and a bottom short edge of 6 mm. On the other hand, CNR_e analysis was performed using three rectangular shaped ROIs, one within the inclusion and two ROI's located in the background at a similar depth as shown in Figure 5.8(a-b). The area of the ROI within the inclusion was equal to the sum of two background ROIs, which were placed symmetrically in the background and parallel to the ROI within the inclusion.

In order to obtain statistically significant results, we estimated the mean and standard deviation of the SNR_e and CNR_e estimates that were obtained over ten independent RF data acquisitions. Statistical analysis was based on similarly selected ROIs in the strain tensor images.

Each independent beam-steered pre- and post-deformation data set was processed using both 1D and 2D motion tracking approaches. We also analyzed the performance changes with different maximum beam steered angles and for different beam steered angular increments.

5.4 Quantitative Analysis Using an Uniformly Elastic TM Phantom

The plots shown in Figures 5.3 and 5.4 present the mean and standard deviation of the SNR_e estimated over ten independent axial strain tensor images. Figure 5.3 presents the variation of SNR_e versus the beam-steered angular increment for a maximum beam steered angle of $\pm 15°$ and angular increments of $1°$, $3°$, $5°$ and $15°$. Each corresponding strain tensor image was calculated from 31, 11, 5 and 3 beam steered RF echo signal frame pairs respectively. The 1D results were obtained from the 1D motion tracking method. The 2D_A results were obtained with only the axial component of the 2D displacement vector obtained with 2D tracking. And the 2D results were obtained using both the axial and lateral components of the angular displacements obtained using our 2D motion tracking method. Observe that SNR_e values decrease with a decrease in the total number of angular displacement images used for image registration for both 1D and 2D motion tracking. For the same maximum angle, a higher SNR_e is obtained with an increase in the number of angular displacement frames used. Note that 2D motion tracking provides both higher mean SNR_e values and significantly lower standard deviations indicated by the errorbars. The results indicate that 2D tracking is a more robust motion tracking method. On the other hand, 1D motion tracking exhibits significantly higher standard deviation which increases the number of angular displacement images needed to obtain a reasonable strain tensor image, when compared to 2D motion tracking. This is due to the increased ultrasound noise artifacts with depth due to attenuation and increased noise artifacts for beam steered RF data obtained at larger beam

insonification angles. The SNR_e estimates obtained using the 2D axial approximation (2D_A) of the axial angular component of the displacement vector, tracked using the 2D parallelogram kernel, also present with lower standard deviations. However, the mean values drop significantly. Thus both the axial- and lateral- angular displacement vectors estimated using our 2D tracking contribute to significantly improved SNR_e values for the axial strain tensor images.

Variations in the SNR_e versus the maximum beam-steered angle used for image registration in increments of 1 ° are shown in Figure 5.4. The SNR_e slightly decreases with an increase in the maximum angle. This is due to the increased artifacts in beam steered echo data pairs obtained at larger beam steered angles. Larger beam steered angles provide additional lateral displacement information at the cost of increased noise artifacts in the angular displacement images. Note that the 2D motion tracking method provides stable and significantly higher SNR_e values over all the strain tensor images estimated at different maximum angles.

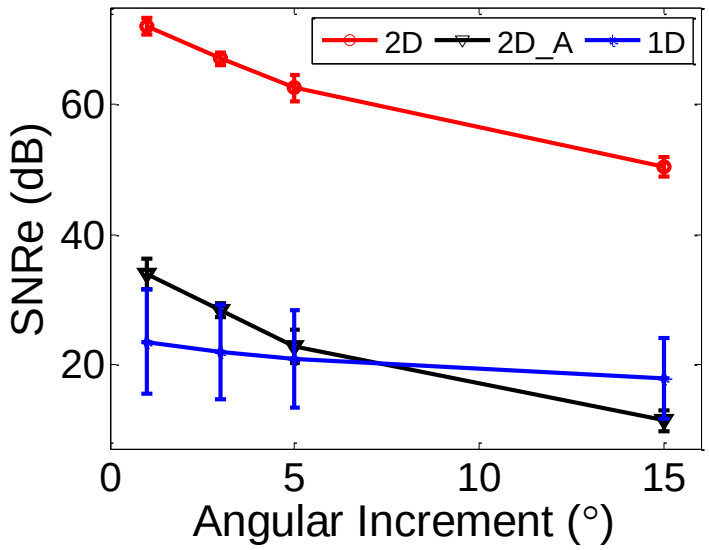

Figure 5.3 Plots of the mean SNR_e and standard deviation (errorbars) of axial strain tensor imagesover ten independent RF data sets acquired on a uniform TM phantom demonstrating the impact of beam steered anglar increment for 1D, 2D and 2D_A.

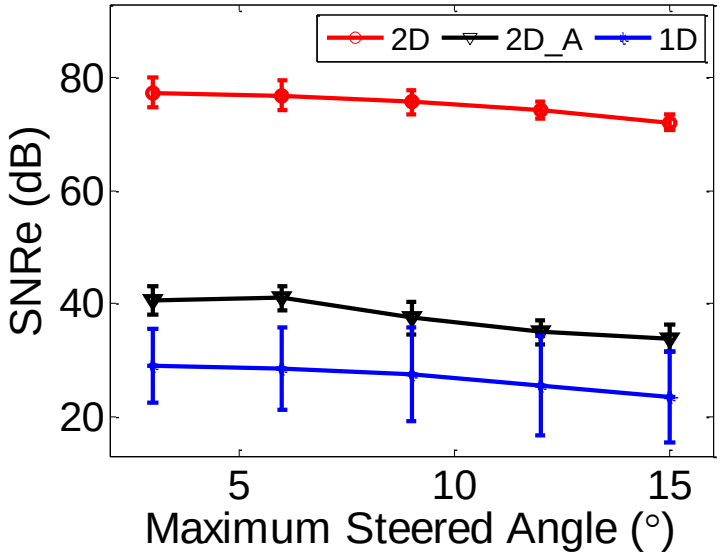

Figure 5.4 Plots of mean SNR_e and standard deviation (errorbars) of axial strain tensor imagesover ten independent RF data sets acquired on a uniform TM phantom demonstrating the impact of maximum angle on compounded strain images for 1D, 2D and 2D_A.

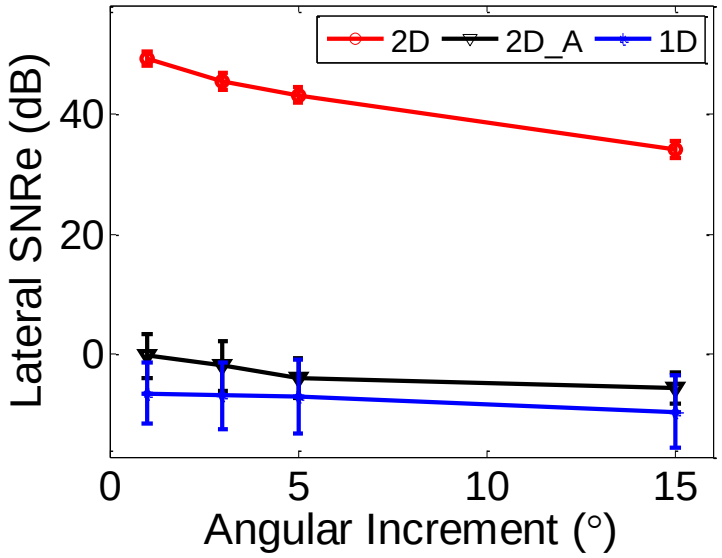

Figure 5.5 Plots of the mean SNR_e and standard deviation (errorbars) of lateral strain tensor imagesover ten independent RF data sets acquired on a uniform TM phantom demonstrating the impact of beam steered anglar increment for 1D, 2D and 2D_A.

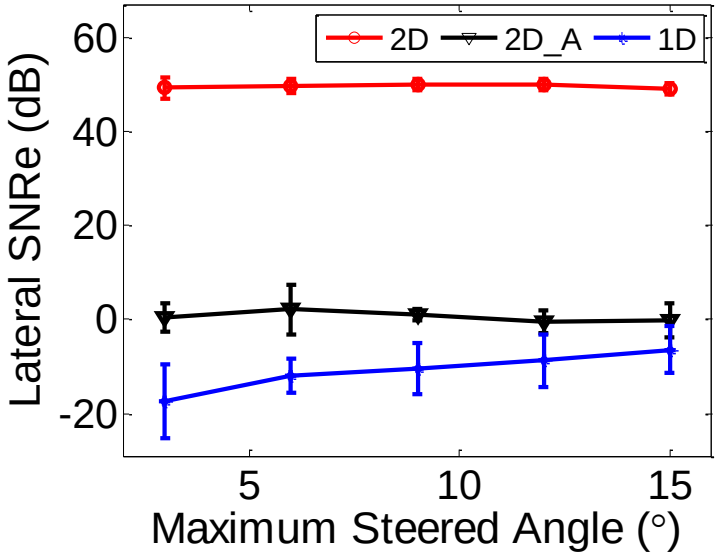

Figure 5.6 Plots of mean SNR_e and standard deviation (errorbars) of lateral strain tensor imagesover ten independent RF data sets acquired on a uniform TM phantom demonstrating the impact of maximum angle on compounded strain images for 1D, 2D and 2D_A.

Figures 5.5 and 5.6 show plots of the SNR_e estimated over ten independent lateral strain tensor images. SNR_e values for lateral strain tensor images obtained using 1D motion tracking are lower than 0 dB, with a larger variance. This means that more noise than signal exists in the lateral strain tensor images obtained using 1D motion tracking. Thus 1D motion tracking does not provide useful lateral strain tensor information. Figure 5.5 indicates that SNR_e values in the lateral strain tensor images also decrease with a decrease in the total number of angular displacement images used for image registration for both 1D and 2D motion tracking. For the same maximum angle, higher lateral SNR_e is obtained with an increase in the number of angular displacement frames. Figure 5.6 presents the variation in the lateral SNR_e versus the maximum beam-steered angle used for image registration. We find that stable lateral SNR_e values are obtained with an increase in the maximum angle, which is slightly different from the results shown in axial SNR_e plot in Figure 5.4. This is due to the fact that the larger beam steered angles provide more accurate lateral displacement information and contribute to an improved lateral

SNR_e under 2D processing is applied. In Figure 5.6 the lateral SNR_e values range from 30 dB to 50 dB. These values are smaller than axial SNR_e values where the range is 50 dB to 70 dB. Note that the lateral SNR_e estimates obtained using the 2D axial approximation (2D_A) of the axial angular component of the displacement vector that is tracked using the 2D parallelogram kernel provides results that are similar, but slightly better than those obtained with only 1D tracking. This is due to the fact that lateral displacement information is not included with this approximation.

5.5 Quantitative Analysis on Ellipsoidal Phantoms

5.5.1. Strain Tensor Imaging of Ellipsoidal Phantoms

Four ellipsoidal unbound and bound inclusion phantoms described previously were also used to compare motion tracking performance among the 1D and 2D approaches. Figures 5.7-5.10 present the displacement, normal strain and shear strain images obtained using 1D and 2D approaches for the unbound, asymmetrical ellipsoidal inclusion phantom. Figure 5.7 presents compounded axial displacement images (a - d), and lateral displacement images (e - h) for the asymmetrical (30 °) unbound ellipsoidal phantom obtained with 1D (a, e), 2D_A (b, f), 2D with 2D filter (c, g) and 2D with 1D filter (d, h). We see that 2D motion tracking provides improved accuracy and precision for the axial displacement vector image, with obvious and precise mass/background interfaces shown in Figure 5.7 (b - d). While 1D processing also exhibits axial displacement vector images with improved accuracy above the focal depth (≤ 40 mm) (Figure 5.7 (a)), it fails to track the mass/background interface accurately near the bottom edges of the interface. The mass/background interface is blurred towards the bottom of the inclusion. This is partly due to the increased tracking errors with 1D processing, reduced signal-to-noise ratio of

the echo signals due to attenuation, and artifacts with beam-steered data at larger insonification angles. The axial displacement vector image of 2D_A presents comparable result to that obtained from both angular components of 2D motion tracking. As shown in Figure 5.7 (b - d), the lateral displacement vector image obtained using 2D motion tracking exhibits a smoother display and a more precise mass/background interface than the image obtained using 1D motion tracking. The lateral displacement vector image obtained using 2D_A presents better result than the image obtained using 1D motion tracking. However, it is worse than result obtained from both angular displacement components. As shown in Figure 5.7 (c, d, g, h), the displacement vector images obtained using 2D motion tracking with 2D median filter exhibit a smoother display at the cost of less detail.

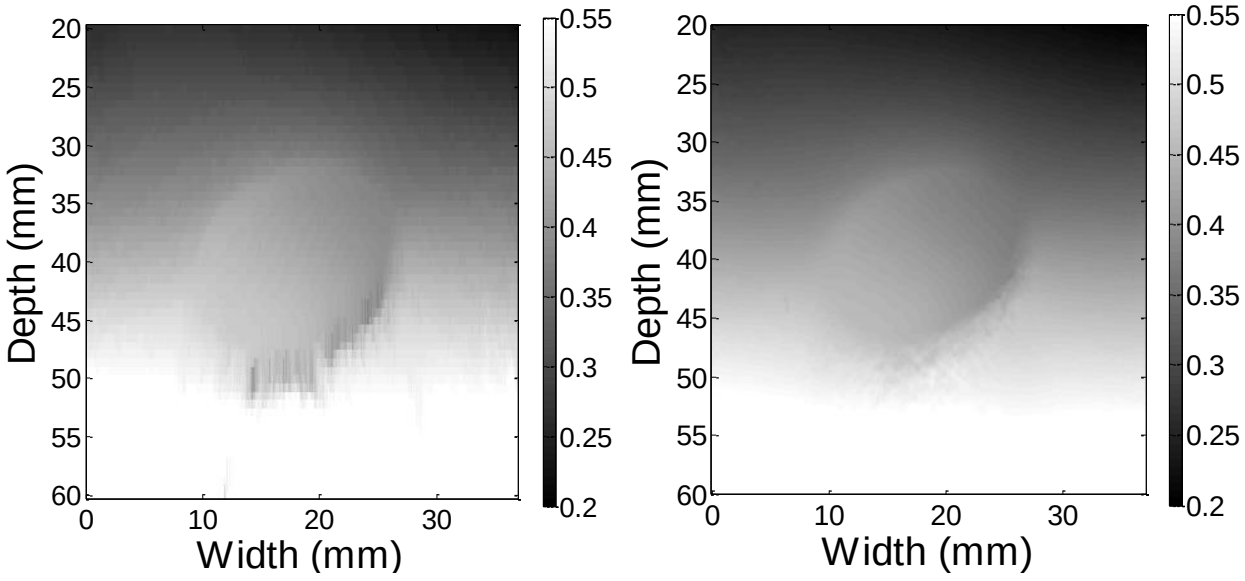

(a) (b)

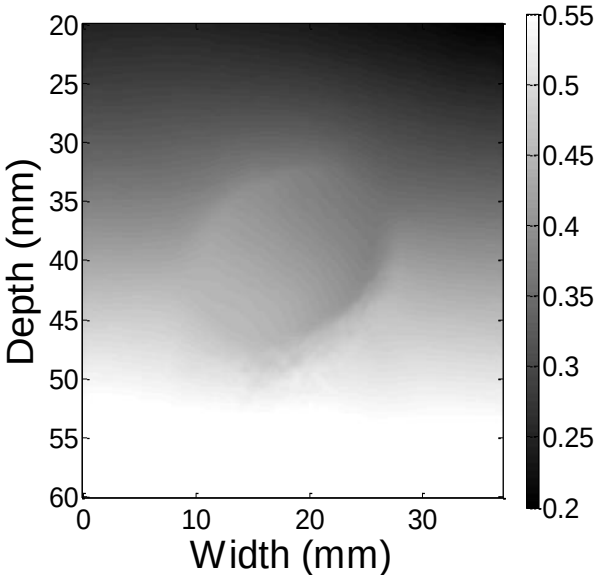
Depth (mm)
Width (mm)
20
25
30
35
40
45
50
55
60
0
10
20
30
0.55
0.5
0.45
0.4
0.35
0.3
0.25
0.2

(c)

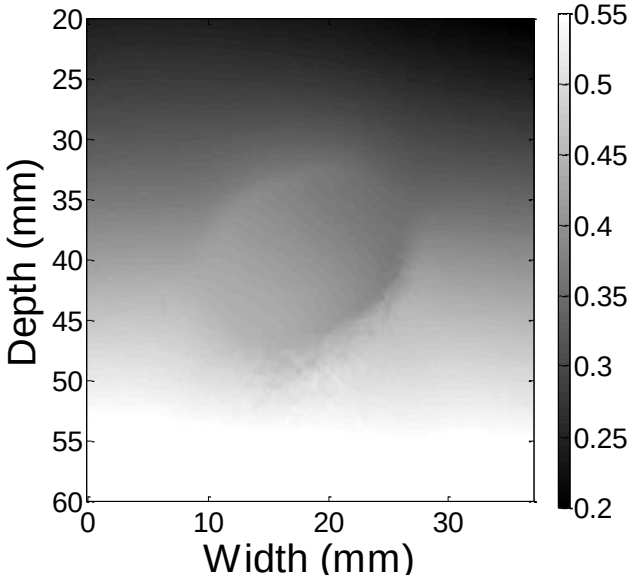
Depth (mm)
Width (mm)
20
25
30
35
40
45
50
55
60
0
10
20
30
0.55
0.5
0.45
0.4
0.35
0.3
0.25
0.2

(d)

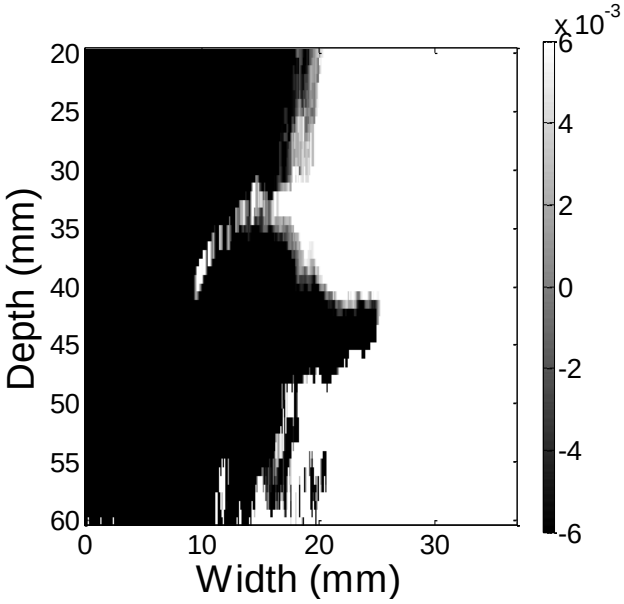
Depth (mm)
Width (mm)
x 10-3
20
25
30
35
40
45
50
55
60
0
10
20
30
6
4
2
0
-2
-4
-6

(e)

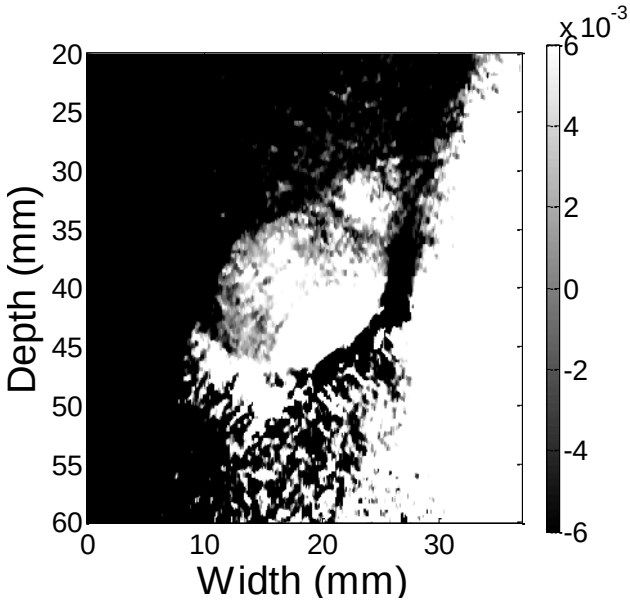
Depth (mm)
Width (mm)
x 10-3
20
25
30
35
40
45
50
55
60
0
10
20
30
6
4
2
0
-2
-4
-6

(f)

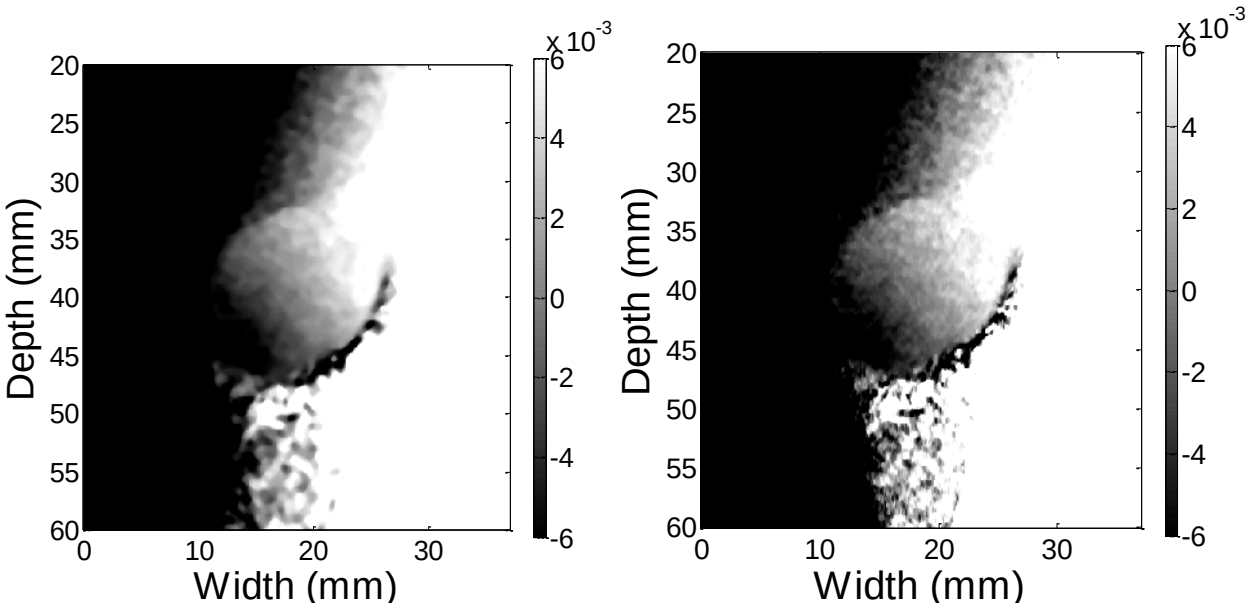

(g) (h)

Figure 5.7 Axial displacement (a - d) and lateral displacement (e - h) images obtained using 1D (a, e), 2D_A(b, f) 2D (c, g) with 2D filter, 2D (d, h) with 1D filter, beam steered data for the asymmetric (30 º) unbound ellipsoid TM phantom. The displacement colorbars are in millimeters.

These local displacement vector improvements obtained using 2D processing contribute to a significant enhancement of the corresponding axial and lateral strain tensor images when compared to 1D processing, as shown in Figure 5.8. The rectangular regions outlined in red show the selected ROIs within the inclusion and the background regions. The blue line represents the left edge of maximum beam steered angle (15 º) for the trapezoidal region previously mentioned. Figure 5.8 (c, d) suggest that 2D motion tracking provides precise mass/background interfaces with the inclusion size and shape accurately illustrated in the axial strain tensor image. The 1D tracking fails to yield strain tensors estimates below the focus depth (> 40 mm) for the lateral strain tensor (Figure 5.8 (e)) and below 50 mm for the axial strain tensor (Figure 5.8 (a)). These artifacts are not visible with 2D motion tracking, as illustrated in Figure 5.8 (b - d, g, h). When compared to images obtained from both angular components of 2D tracking, results obtained from 2D_A (axial angular component) are comparable for axial strain tensor (Figure 5.8 (b, d)),

but less detail for lateral strain tensor (Figure 5.8 (f, h)). The 2D motion tracking with angular displacements filtered by a 2D median filter will provide smooth results at the cost of less detail when compared to results obtained from angular displacements filtered by a 1D median filter (Figure 5.8(c, d, g, h)).

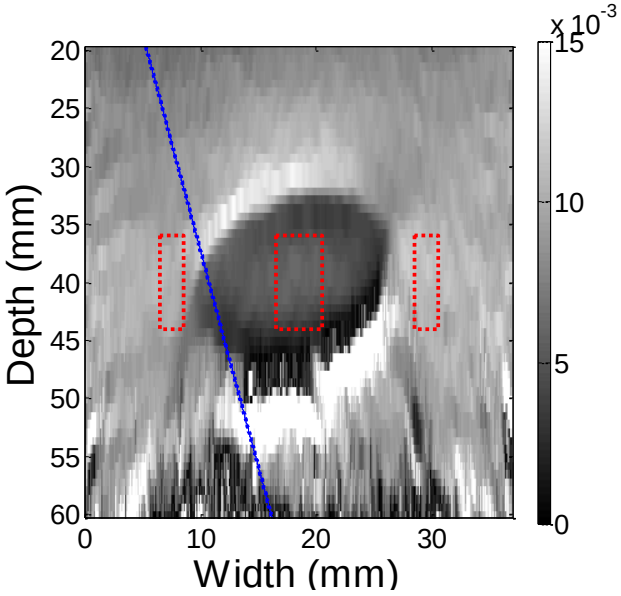

(a)

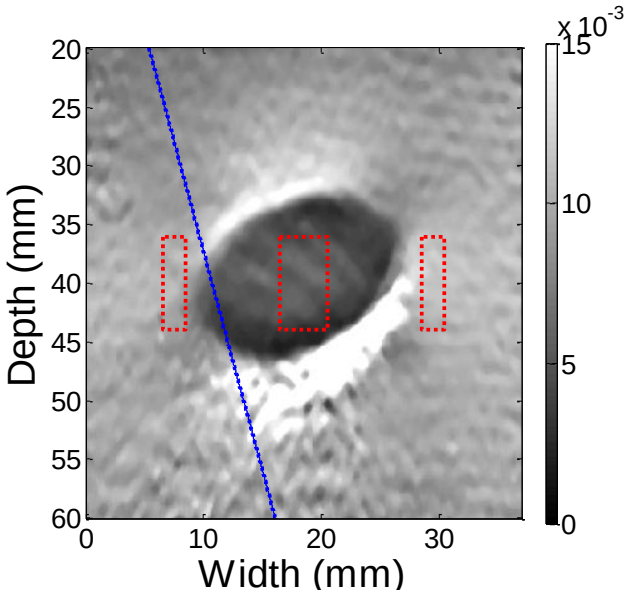

(b)

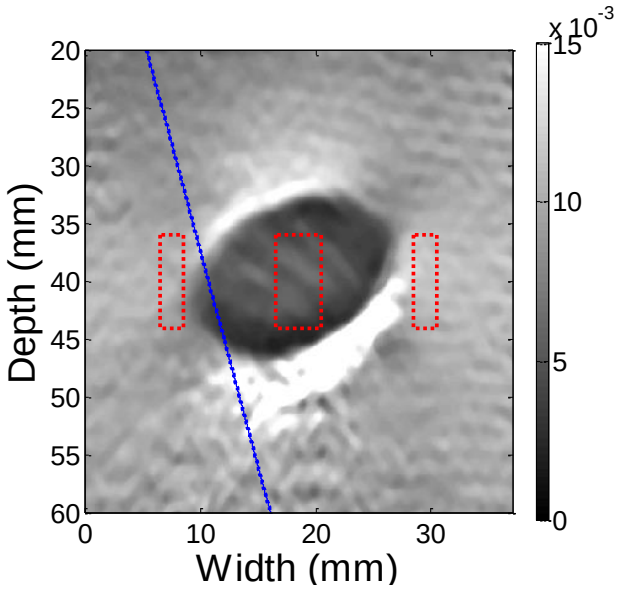

(c)

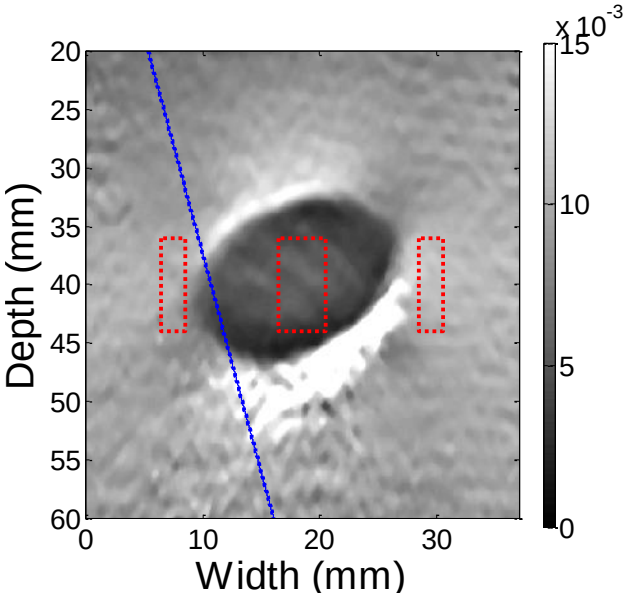

(d)

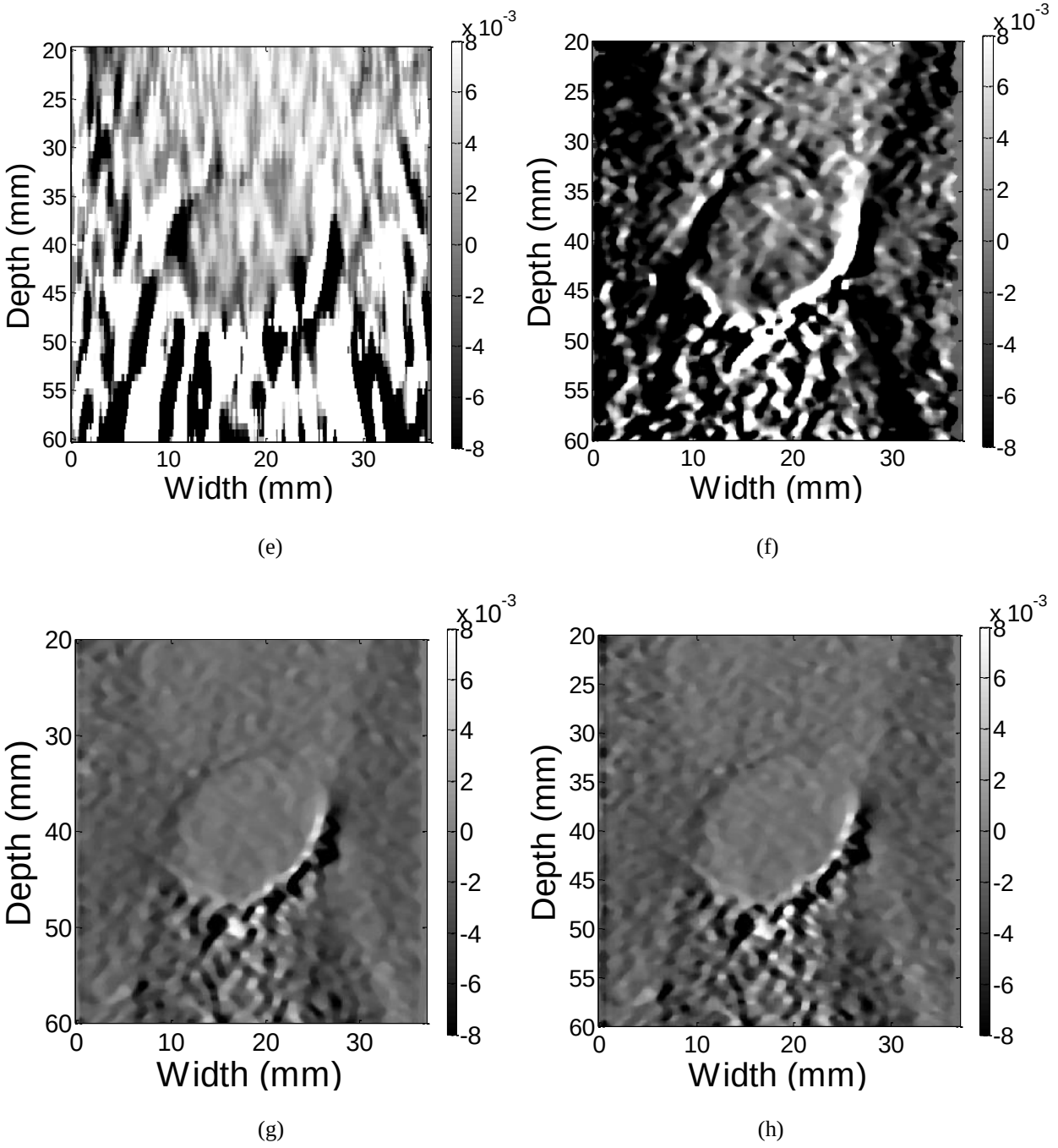

Figure 5.8 Axial strain (a - d) and lateral strain (e - h) images obtained using 1D (a, e), 2D_A(b, f), 2D with 2D filter (c, g) and 2D (d, h), beam steered data for the asymmetric (30 °) Unbound ellipsoid TM phantom. The 0.01 value on the colorbar represents 1% strain. The ROIs shown were used to estimate CNR_e and strain contrast. The blue line represents the maximum beam steered angle used for strain compounding.

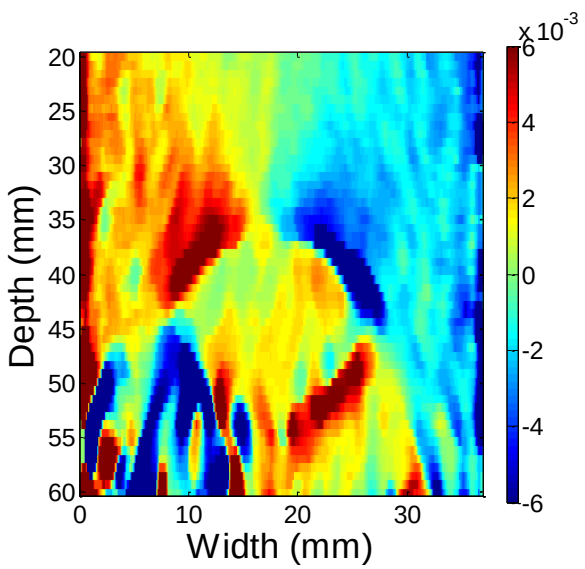
x 10^-3
6
4
2
0
-2
-4
-6
Depth (mm)
20
25
30
35
40
45
50
55
60
0
10
20
30
Width (mm)

(a)

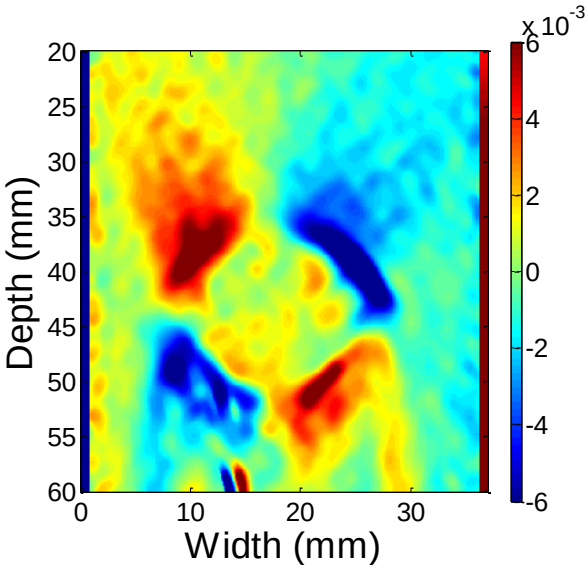
x 10^-3
6
4
2
0
-2
-4
-6
Depth (mm)
20
25
30
35
40
45
50
55
60
0
10
20
30
Width (mm)

(b)

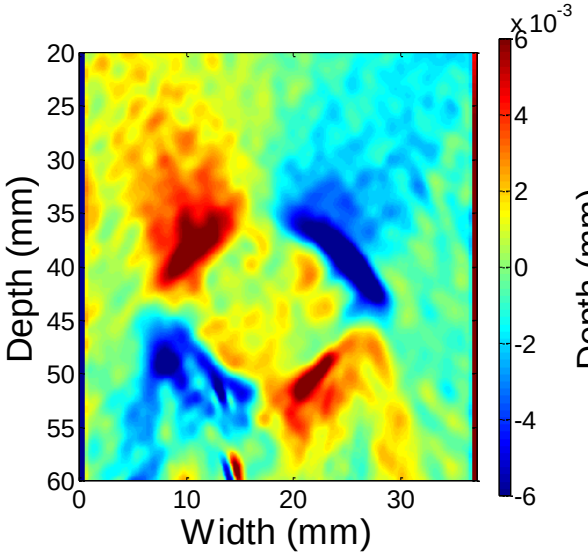
x 10^-3
6
4
2
0
-2
-4
-6
Depth (mm)
20
25
30
35
40
45
50
55
60
0
10
20
30
Width (mm)

(c)

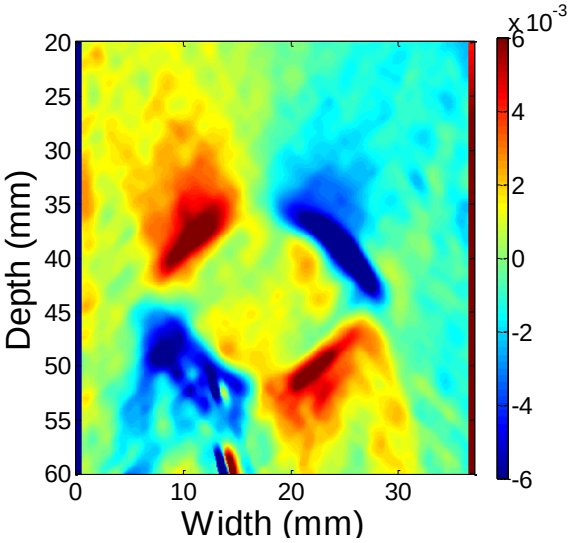
x 10^-3
6
4
2
0
-2
-4
-6
Depth (mm)
20
25
30
35
40
45
50
55
60
0
10
20
30
Width (mm)

(d)

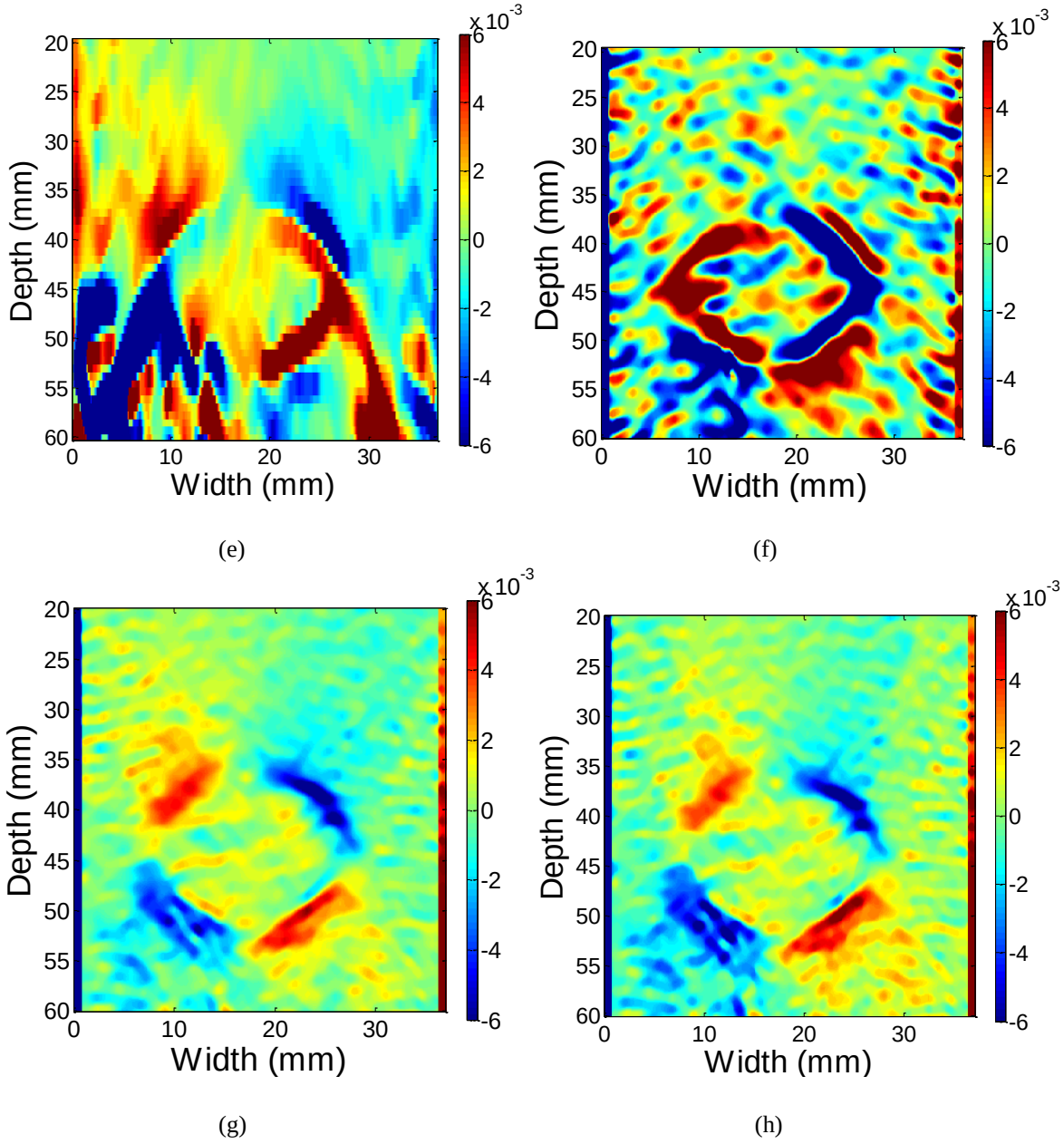

Figure 5.9 Axial-shear strain (a - d) and full-shear strain (e - h) images obtained using 1D (a, e), 2D_A (b, f), 2D with 2D filter (c, g) and 2D (d, h), beam steered data for the symmetric (0 °) Unbound ellipsoid TM phantom. The 0.01 value on the colorbar represents 1% strain. The ROIs shown were used to estimate CNR_e and strain contrast. The blue line represents the maximum beam steering angle used for strain compounding.

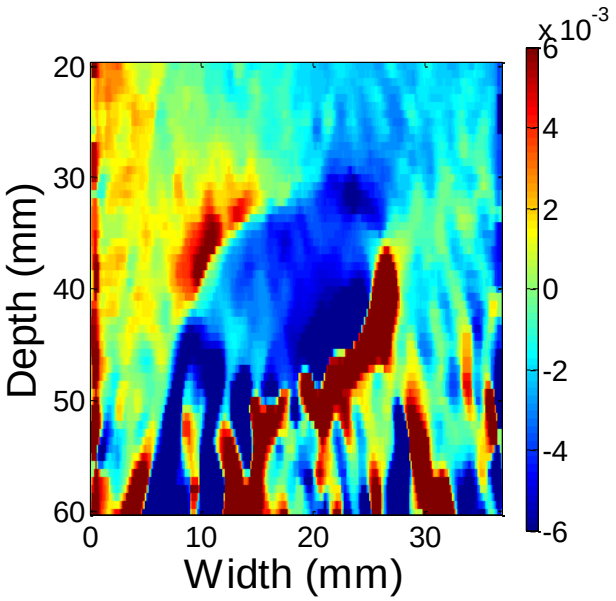
x 10^-3
6
4
2
0
-2
-4
-6
Depth (mm)
Width (mm)
20
30
40
50
60
0
10
20
30

(a)

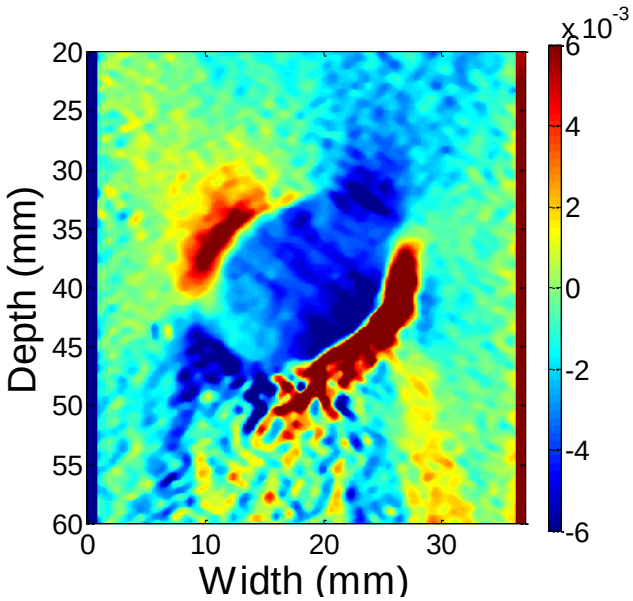
x 10^-3
6
4
2
0
-2
-4
-6
Depth (mm)
Width (mm)
20
25
30
35
40
45
50
55
60
0
10
20
30

(b)

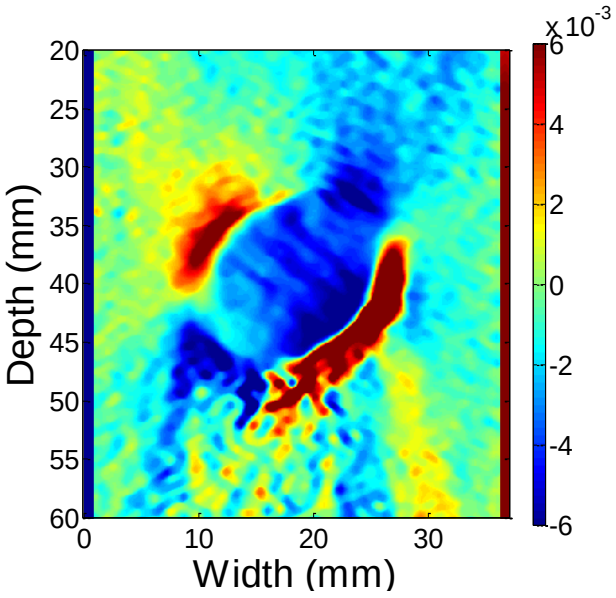
x 10^-3
6
4
2
0
-2
-4
-6
Depth (mm)
Width (mm)
20
25
30
35
40
45
50
55
60
0
10
20
30

(c)

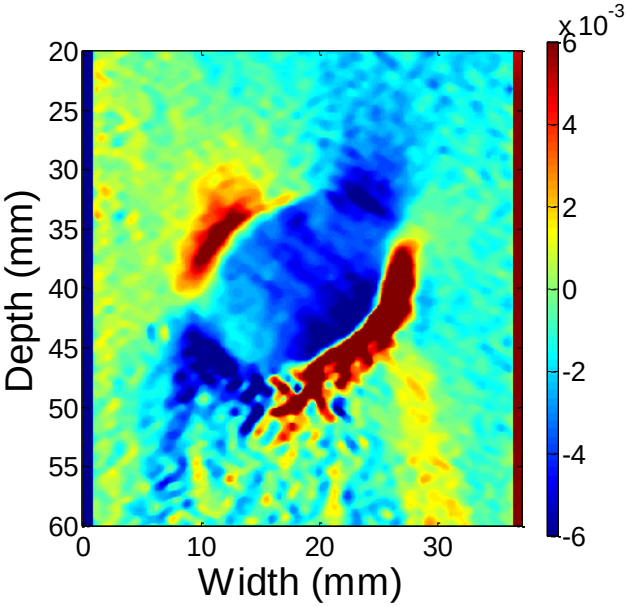
x 10^-3
6
4
2
0
-2
-4
-6
Depth (mm)
Width (mm)
20
25
30
35
40
45
50
55
60
0
10
20
30

(d)

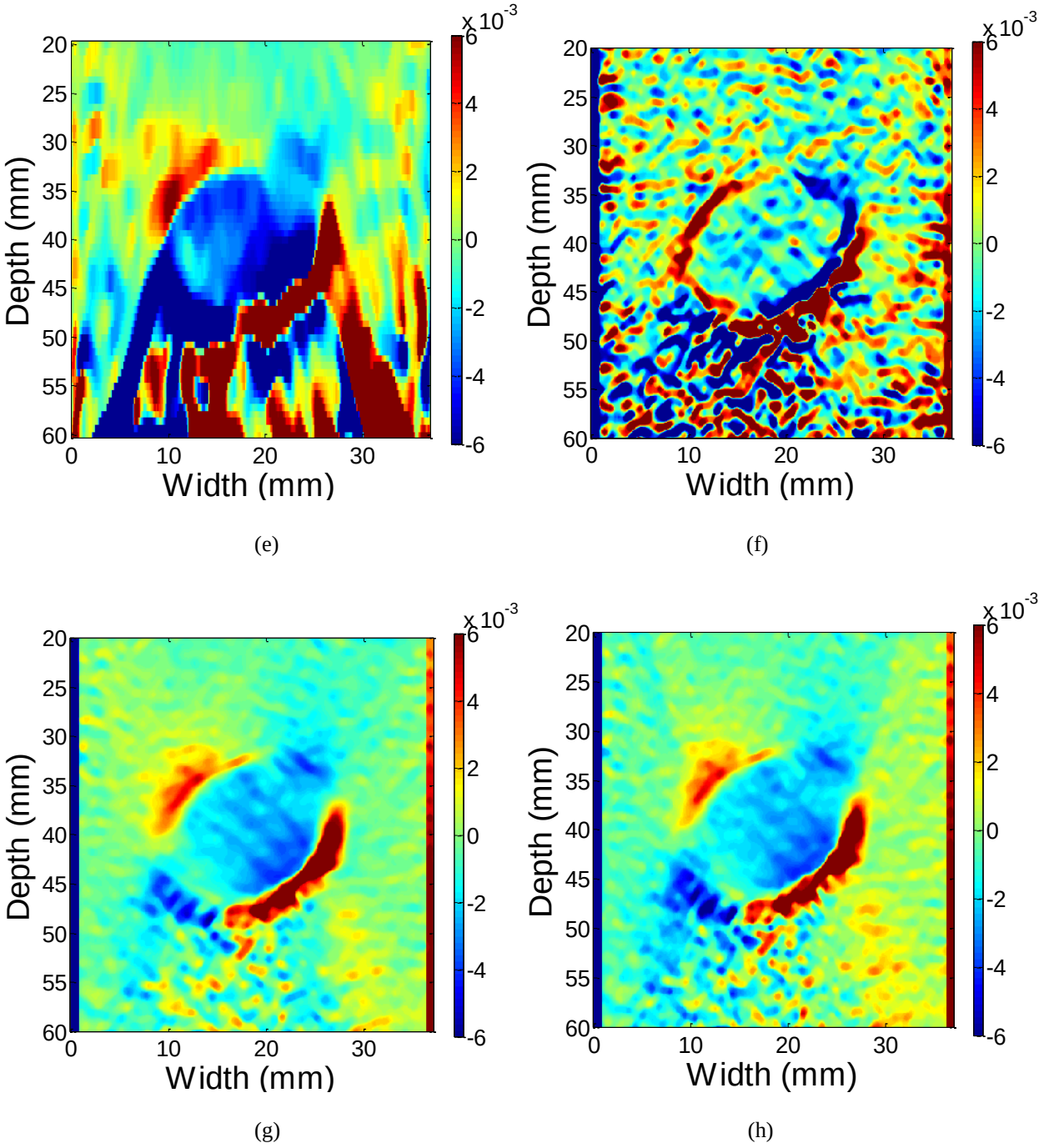

Figure 5.10 Axial-shear strain (a - d) and full-shear strain (e - h) images obtained using 1D (a, e), 2D_A(b, f), 2D with 2D filter (c, g) and 2D (d, h), beam steered data for the asymmetric (30 ٩) Unbound ellipsoid TM phantom. The 0.01 value on the colorbar represents 1% strain. The ROIs shown were used to estimate CNR_e and strain contrast. The blue line represents the maximum beam steering angle used for strain compounding.

Figures 5.9 and 5.10 present a qualitative comparison of axial-shear (a-d) and full-shear strain images (e-h) obtained using 1D (a, e) and 2D (b-d, f-h) motion tracking methods. Figure 5.9 presents results obtained from a symmetrical model, while Figure 5.10 presents image results obtained from an asymmetrical model. The blue and red colors in the figure represent different directions for the shear strain. The value of 0.01 on the colorbar represents a 1% strain. The fact that 1D motion tracking fails to track deformations deeper than 45 mm is evident in both the axial-shear strain and full-shear strain images. Also, 2D motion tracking provides improved accuracy and precision for the axial-shear and full-shear strain with precise shear strain regions around the mass/background interfaces as can be seen in Figure 5.9 and 5.10 (c-d, g-h). The inclusion shape and size are also clearly visualized. The red and blue shear noise artifacts that appear in the background in the images in Figure 5.9&5.10 (a, e) are also significantly reduced as observed in Figure 5.9 and 5.10 (d, f). Results obtained from 2D_A (axial angular component of 2D motion tracking) are comparable to results obtained from both components for axial-shear strain vector, however, noisy for full shear strain vector.

5.5.2. Comparison of *CNRe* for Axial Strain Tensor Imaging

Quantitative results demonstrating the improvements in the CNR_e obtained with 2D tracking are presented in this section. Figure 5.11 presents the impact of utilizing different beam steering angular increments in the data acquisition. Figure 5.11 (a) presents results for the symmetrical unbound ellipsoidal phantom; Figure 5.11 (b) is for the asymmetrical unbound ellipsoidal phantom; Figure 5.11 (c) represents the symmetrical bound ellipsoidal phantom; and Figure 5.11 (d) shows results for the asymmetrical bound ellipsoidal phantom. The error bars denote the standard deviation of the CNR_e estimated over ten independent experiments.

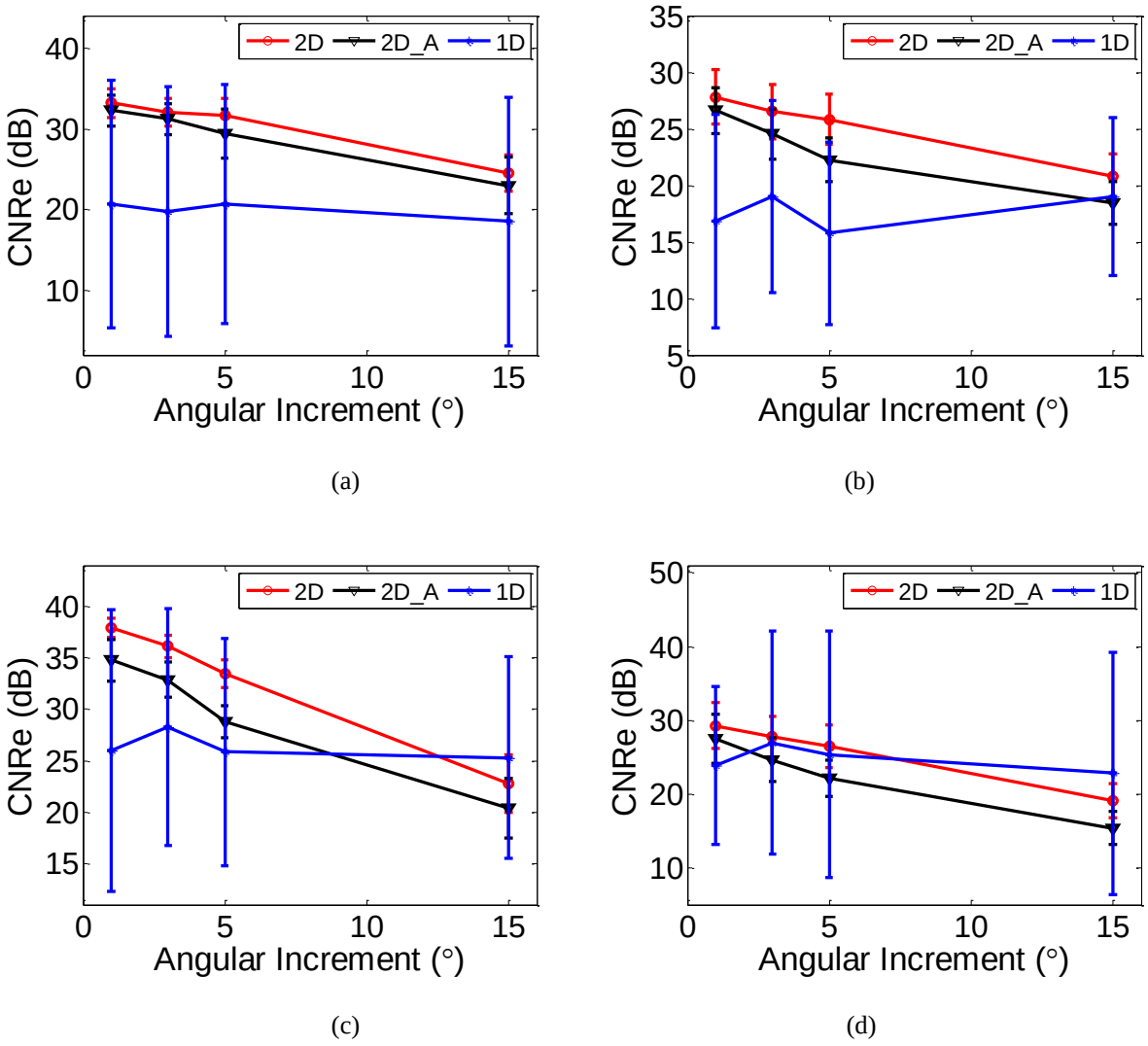

Figure 5.11 Plots of mean CNR_e and standard deviation (errorbars) over ten independent beam-steered RF data sets acquired on the four ellipsoid TM phantoms demonstrating the impact of beam steered angular increment for 1D, 2D_A and 2D compunding. The sub-plots represent results for (a) symmetric unbound, (b) asymmetric unbound, (c)symmetric bound, and (d)asymmetric bound phantoms respectively.

Results show that 2D motion tracking provides a higher mean CNR_e and significantly lower variance in the image than to 1D motion tracking for each of the ellipsoidal phantoms. The mean CNR_e for unbound masses utilizing the 2D motion tracking method is about 10 dB higher than that obtained using 1D motion tracking as shown in Figure 5.11 (a-b). It is about 6dB greater for bound masses, as seen in Figure 5.11 (c-d). For smaller angular increments (1^o up to 5^o), the

CNR_e is almost constant for the increases in the steered angular increment when using 2D processing. However, for larger angular increments, the mean CNR_e decreases with an increase in the angular increment. This is observed in results for all four phantoms. On the other hand, the CNR_e is relatively constant with an increase in the angular increment for 1D motion tracking. This is due to the concomitant increase in artifacts associated with the angular strain image obtained at larger beam steered angles, and the inability of 1D processing to accurately track the displacement in this region. Also note that the CNR_e estimates obtained using the 2D axial approximation (2D_A) to the axial angular component of displacement vector, tracked using the 2D parallelogram kernel present with a comparable mean and standard deviation when compared to the 2D tracking results. The results obtained using the 2D axial approximation (2D_A) is significantly better than that obtained with 1D tracking. In addition, the lateral displacement information present within the 2D tracking results contribute to about a 3 dB improvement in the CNR_e mean value when compared to the 2D axial approximation results (2D_A).

Mean and standard deviation values of the corresponding stiffness contrast estimated versus different beam-steered angular increments used to generate the compounded image is shown in Table 5.1. The mean and standard deviation were estimated over the ten independent experiments corresponding to the CNR_e variations evaluated previously. The actual modulus contrast for the symmetrical bound/unbound ellipsoidal phantom (0 ⁄90) was 4.2 while that for the asymmetrical bound/unbound ellipsoidal phantoms (30 ⁄60) was 3.2 respectively. Observe that strain contrast calculated from axial-strain images over ROI within the mass and ROI in the background was around 2.1 for the symmetrical phantoms, and 2.0 for the asymmetrical phantoms. Note that results obtained from 2D tracking method present lower variance when compared to results obtained from 1D tracking method though out all angular increments.

Results obtained from axial component alone (2D_A) presents comparable variance level to results obtained from full components of 2D tracking method.

Table 5.1 Mean and standard deviation of the strain contrast for the ellipsoidal inclusion TM phantoms for different angular increments for 1D, 2D and 2D_A.

Phantom	Contrast	Method		Angular Increments			
				1°	3°	5°	15°
Unbound Ellipsoid (0°/90°)	4.2	1D	Mean	2.11	2.12	2.17	1.95
			Std	0.29	0.30	0.27	0.22
		2D_A	Mean	2.12	2.12	2.09	2.07
			Std	0.04	0.05	0.06	0.07
		2D	Mean	2.18	2.19	2.18	2.16
			Std	0.03	0.03	0.03	0.05
Unbound Ellipsoid (30°/60°)	3.2	1D	Mean	2.09	2.05	2.13	2.08
			Std	0.23	0.14	0.23	0.11
		2D_A	Mean	1.98	1.96	1.93	1.91
			Std	0.05	0.04	0.04	0.08
		2D	Mean	2.04	2.00	1.99	1.97
			Std	0.03	0.07	0.08	0.12
Bound Ellipsoid (0°/90°)	4.2	1D	Mean	2.07	2.14	2.06	1.88
			Std	0.18	0.18	0.20	0.30
		2D_A	Mean	2.05	2.06	2.04	2.05
			Std	0.04	0.07	0.07	0.12
		2D	Mean	2.11	2.11	2.11	2.12
			Std	0.05	0.05	0.06	0.06
Bound Ellipsoid (30°/60°)	3.2	1D	Mean	2.2	2.19	2.06	1.60
			Std	0.58	0.61	0.40	0.44
		2D_A	Mean	1.86	1.85	1.82	1.75
			Std	0.06	0.06	0.07	0.06
		2D	Mean	1.96	1.95	1.94	1.91
			Std	0.04	0.04	0.06	0.06

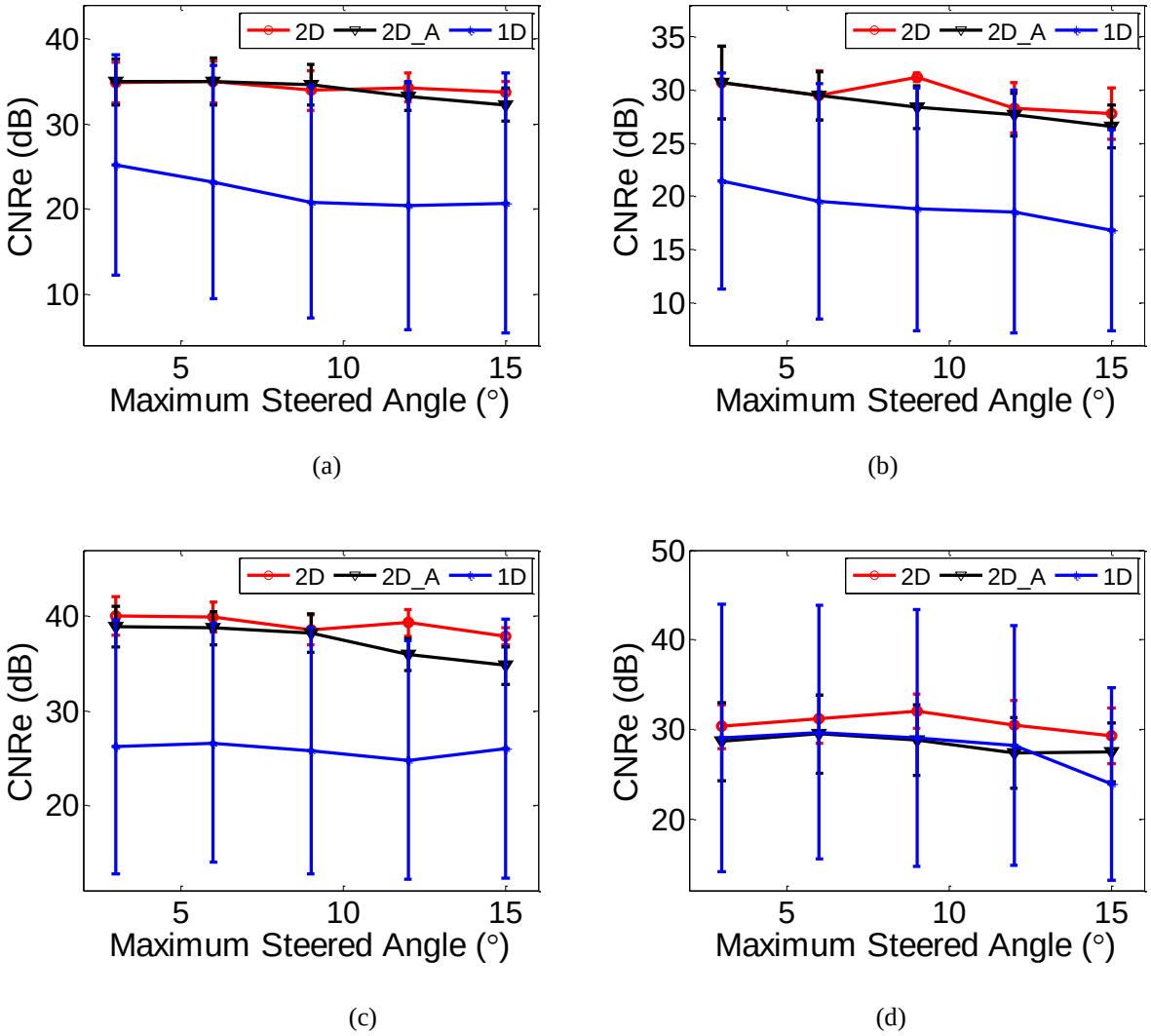

Figure 5.12 Plots of mean CNR_e and standard deviation (errorbars) over ten independent RF data sets acquired on the four ellipsoid TM phantoms demonstrating the impact of maximum angle for 1D, 2D and 2D_A compunding. The sub-plots represents results for the (a) symmetric unbound, (b) asymmetric unbound, (c) symmetric bound, and (d) asymmetric bound phantom respectively.

Figure5.12 presents plots of the CNR_e versus the maximum beam steered angle in increments of 1 °. Note that the mean CNR_e plot for the 1D motion tracking decreases with an increase in the maximum angle. This is due to the increased induced noise associated with larger beam steered angles. Larger beam steered angles provide additional lateral displacement information, however with the concomitant increase in noise artifacts due to the larger insonification angles. Note that

the standard deviation of the CNR_e plots vary greatly with increased maximum angle especially with 1D tracking. The mean CNR_e calculated using 2D motion tracking is about 10 dB higher than that estimated using 1D motion tracking. At a step of 1^o results obtained from angular displacement alone present comparable *CNRe* results as those obtained by full components.

Table 5.2 Mean and standard deviation of the strain contrast for the ellipsoidal inclusion TM phantoms for different maximum beam steered angles for 1D, 2D and 2D_A.

Phantom	Contrast	Method		Maximum Steered Angle (°)				
				3 °	6 °	9 °	12 °	15 °
Unbound Ellipsoid (0 ⁄90 °)	4.2	1D	Mean	2.15	2.16	2.20	2.17	2.11
			Std	0.12	0.16	0.29	0.30	0.29
		2D_A	Mean	2.21	2.21	2.19	2.16	2.12
			Std	0.03	0.03	0.04	0.03	0.04
		2D	Mean	2.21	2.21	2.23	2.20	2.18
			Std	0.02	0.03	0.05	0.02	0.03
Unbound Ellipsoid (30 ⁄60 °)	3.2	1D	Mean	2.14	2.17	2.17	2.13	2.09
			Std	0.14	0.19	0.21	0.20	0.23
		2D_A	Mean	2.06	2.06	2.04	2.04	1.98
			Std	0.07	0.05	0.04	0.05	0.05
		2D	Mean	2.13	2.05	2.03	2.06	2.04
			Std	0.07	0.05	0.11	0.04	0.03
Bound Ellipsoid (0 ⁄90 °)	4.2	1D	Mean	2.01	2.10	2.13	2.27	2.07
			Std	0.25	0.25	0.21	0.60	0.18
		2D_A	Mean	2.13	2.13	2.12	2.09	2.05
			Std	0.07	0.07	0.07	0.06	0.04
		2D	Mean	2.13	2.15	2.13	2.12	2.11
			Std	0.07	0.07	0.1	0.06	0.05
Bound Ellipsoid (30 ⁄60 °)	3.2	1D	Mean	2.01	2.10	2.13	2.27	2.2
			Std	0.25	0.25	0.21	0.60	0.58
		2D_A	Mean	1.98	1.97	1.96	1.92	1.86
			Std	0.06	0.07	0.08	0.07	0.06
		2D	Mean	2.00	2.00	2.04	1.98	1.96
			Std	0.04	0.04	0.06	0.04	0.04

Table 5.2 presents the corresponding strain contrast estimated for different maximum beam-steered angles. The strain contrast for the compounded strain images obtained using 2D motion

tracking provides consistent results over all the maximum angles used. The symmetrical unbound/bound ellipsoidal phantom pair has a strain contrast around 2.1. On the other hand, the asymmetrical unbound/bound ellipsoidal phantom pair has a strain contrast around 2.0, which is similar to the values reported in Table 5.1.

5.5.3. Comparison of *CNRe* for Lateral Strain Tensor Imaging

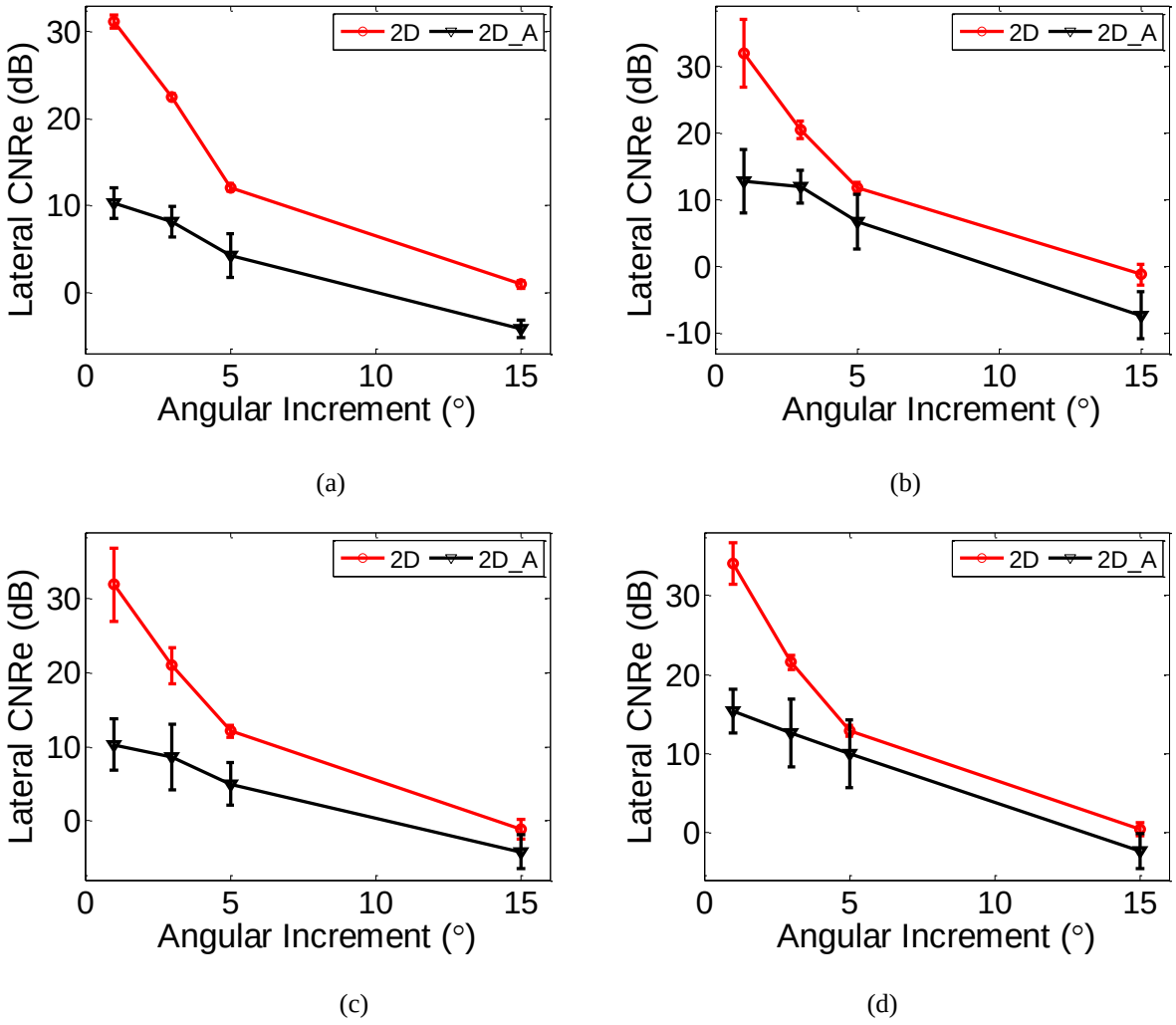

Figure 5.13 Plots of the CNR_e and standard deviation (errorbars) of the lateral strain tensor imagesover ten independent beam-steered RF data sets acquired on the four ellipsoid TM phantoms. The results demonstrate the impact of beam steered angular increment using only the axial component vs. the full (axial and lateral) components obtained using 2D tracking. The sub-plots represent results for (a) symmetric unbound, (b) asymmetric unbound, (c) symmetric bound, and (d) asymmetric bound phantoms respectively.

Figure 5.13 and 5.14 present the CNR_e for lateral strain tensor images obtained from the four ellipsoidal phantoms. Note that lateral strain tensor images using only 1D motion tracking present with more noise than signal as demonstrated in Figure 5.5 and 5.6, thus the plots only present results obtained using only the axial component, i.e. the 2D axial approximation (2D_A) versus the full (axial and lateral) component of 2D motion tracking. Figure 5.13 demonstrates the impact of the angular increment on the CNR_e estimated for lateral strain tensor images. Figure 5.13 (a) presents results for the symmetrical unbound ellipsoidal phantom; Figure 5.13 (b) for the asymmetrical unbound ellipsoidal phantom; Figure5.13 (c) for the symmetrical bound ellipsoidal phantom; and Figure 5.13 (d) for the asymmetrical bound ellipsoidal phantom. Observe that the mean CNR_e in the lateral strain images obtained using both the axial and lateral components or 2D tracking is about 5-20 dB higher than that obtained from that obtained using only the axial component or the 2D axial approximation (2D_A). These results demonstrate the contribution of the lateral angular displacement component to lateral displacement vector. Also note that the plots of lateral strain exhibit a larger standard deviation when compared to the axial strain tensor, which is due to the lower resolution along the lateral direction. Observe that the mean CNR_e of the lateral strain drops significant with an increase in the angular increment. An angular increment larger than 5^o will introduce more noise than signal when only axial component is used in the transformation. In addition, note that the results obtained using only the axial angular component, present with a larger standard deviation when compared to the complete 2D transformation using both the axial and lateral components.

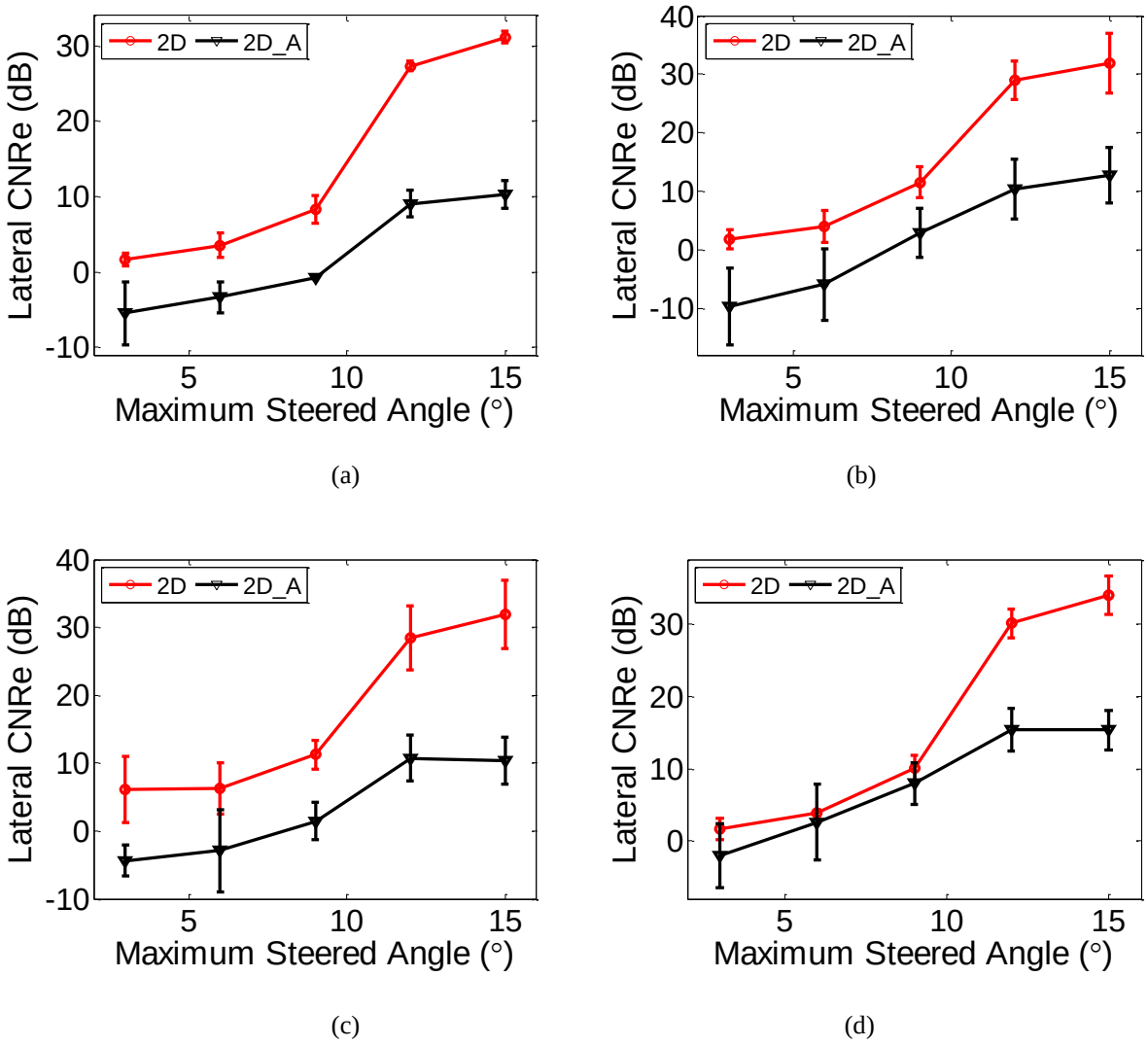

Figure 5.14 Plots of CNR_e and standard deviation(errorbars) of the lateral strain tensor imagesover ten independent RF data sets acquired on the four ellipsoid TM phantoms. The results demonstrate the impact of the maximum beam steered angle,using only theaxial component vs. the full (axial and lateral) components obtained using 2D tracking. The sub-plots represents results for the (a) symmetric unbound, (b) asymmetric unbound, (c) symmetric bound, and (d) asymmetric bound phantom respectively.

Figure5.14 presents plots of the CNR_e estimated on lateral strain images of the ellipsoidal phantoms versus the maximum beam steered angle in increments of 1 °. Note that the mean CNR_e plot for 2D motion tracking increases along with increased maximum angle. Thus larger beam steered angles can provide additional lateral displacement information, however, it also introduces additional noise artifacts associated with larger insonification angles. Results obtained

from lateral strain tensor images also exhibit larger standard deviation when compared to that obtained from axial strain tensor images. The mean CNR_e obtained using the2D transformation is about 20 dB higher than that obtained using only the axial- angular component and the resulting 1D transformation. In addition, note that abeam-steered angle larger than 6^o is required for the 2D axial approximation (2D_A) to provide positive CNR_e estimates.

5.6 Discussion

Results obtained with uniformly elastic phantoms in this chapter, demonstrate the significant improvement in the spatial resolution and SNR_e obtained with the use of the 2D parallelogram shaped processing kernels (0.385 mm × 3 A-lines) when compared to that obtained with 1D processing with 3 mm gated rectangular data segments. Spatial resolution improved by a factor around 7, while the axial SNR_e with 2D processing is approximately 40 dB better than that obtained with 1D processing. The ROI over which the SNR_e was computed corresponds to the trapezoidal region over which angular displacement estimates from all the beam-steered angles are included in the composite axial-strain image. For the same maximum beam steered angle, higher SNR_e is obtained with an increase in the number of angular displacements used to obtain the compounded strain images. On the other hand for the same angular increment, an increase in the maximum beam steered angle slightly reduces the axial SNR_e obtained using 2D motion tracking methods. 1D motion tracking presents similar declines in the SNR_e for maximum angles less than or equal to 6°, however, the performance drops rapidly for maximum angles greater than 6°. In addition, the standard deviation of the compounded axial strain images over ten independent RF data sets utilizing 2D motion tracking methods is 1/7 of that obtained utilizing 1D motion tracking, demonstrating that 2D motion tracking is both an accurate and robust

motion tracking method. An increase in the maximum beam steered angle can reduce variance of lateral SNR_e . The lateral strain tensor obtained from 1D motion tracking cannot provide enough signal, which results in negative mean SNR_e values. Results obtained from axial-angular displacement alone with 1D transform are around 3-5 dB higher than 1D processing, but around 35 dB lower than results obtained from full components with 2D transform.

Noise artifacts observed below the inclusion with 1D processing were not visible with 2D processing for displacement, strain and shear strain images, demonstrating the superior deformation tracking obtained with 2D tracking, especially for regions with lower signal-to-noise. Lateral strain images that were poorly tracked using the 1D motion tracking approach, are significantly improved with 2D processing. In addition, 2D motion tracking provide clear and smooth inclusion/background interfaces over the entire image, where these interfaces clearly differentiate the inclusions for both unbound and bound masses. Asymmetrical inclusion phantoms poorly tracked with 1D processing are clearly visualized with 2D processing. Background noise artifacts in strain images observed with 1D processing were significantly reduced using 2D processing.

Experimental results for the ellipsoidal phantoms show that 2D parallelogram shaped processing blocks for motion tracking provide a significant improvement in the CNR_e of 14 dB for unbound masses and 8 dB for bound masses, respectively, for a maximum angle of 15 °, when compared to results obtained using 1D motion tracking. The CNR_e curves presented in Figure 5.11 exhibit saturation for smaller angular increments, which corresponds to results presented in Rao et al. [75]. For smaller angular increments, the angular displacements obtained are highly correlated, and an angular increment of approximately 3 ° is necessary to obtain accurately

compounded strain images using either 1D or 2D motion tracking methods. Since the errorbars for 1D processing are significantly larger than that those for 2D processing, there is some overlap between the errorbars for the two methods. However, observe the length of the errorbars for 2D processing when compared to 1D motion tracking, which aptly indicates the robustness of the 2D motion tracking approach described in this chapter. The mean CNR_e obtained from lateral strain tensor images is around 20 dB lower than results obtained from axial strain tensor images. At the same angular increment ($1°$), larger maximum angle can provide better CNR_e performance for lateral strain tensor. A maximum angle larger than $6°$ is necessary to estimate lateral strain tensor images with a positive CNR_e value. The lateral mean CNR_e performance drops with larger angular increments. An angular increment smaller than $5°$ is recommended to obtain accurate lateral strain tensor images.

Chapter 6:

In-vivo Axial Shear Strain Imaging for Benign and Malignant Breast Masses

6.1 Introduction

As shown in the previous chapters, axial shear strain images of firmly bonded inclusions/masses in phantoms as well as images generated using FEA simulation exhibit larger shear-strain areas around the inclusion boundary than those generated when masses are loosely bonded. In this chapter, *in-vivo* axial-shear strain imaging of patients who have breast masses is performed. The subject material is in the form of radiofrequency (RF) echo data acquired previously during a freehand palpation imaging study [32]. The feasibility of using shear strain area estimates extracted from the axial shear strain images of these *in-vivo* data sets for breast tumor diagnosis is studied in this chapter. These area estimates exhibit larger values as the friction coefficient around the mass boundary increases.

In order to avoid any bias in the selection of the axial-shear strain region, the area included in this was estimated automatically using a computer program, that applied a threshold and then normalizing the shear strains, generating what we have called the normalized axial-shear strain area (NASSA) feature value. The detection performance using NASSA for breast tumor

Material in this chapter was adapted from:

Xu, H., Rao,M., Varghese, T., Baker, S., Sommer, A.M., Hall, TJ., Burnside, E.S., and Sisney, G.A., *Axial-shear strain imaging for differentiating benign and malignant breast masses.* Ultrasound Med Biol, 2010. **36**(11): p. 1813-24.

Xu, H., Varghese, T., J, Jiang., J.A. Zagzebski., "In vivo classification of breast masses using featuresderived from axial-strain and axial-shear images,"Ultrason Imaging **34**, (2012):p. 222-236

classification was quantitatively evaluated using the area under the curve (AUC), that describes the receiver operating characteristic (ROC) [140-143].

6.2 *In-vivo* Radio Frequency Data Acquisitions

In-vivo data on human patients, had been acquired during freehand "palpation imaging". This was performed by pressing the ultrasound transducer against the breast, and acquiring RF echo data during strain imaging. RF data loops were acquired at the University of Wisconsin Breast Center using a Siemens SONOLINE Antares clinical scanner (Siemens Healthcare, Malvern, PA, USA) equipped with a VFX13-5 linear array transducer pulsed at 10 MHz. The primary criterion for inclusion in the study was an adult female who gave informed consent and was scheduled for a biopsy of an isolated solid breast lesion (i.e. BI-RADS score 4 or 5), at the University of Wisconsin Hospitals and Clinics Breast Center. Only lesions that fit within the 4 cm width of the linear array transducer were scanned for this study. Exclusion criteria were patients with prior surgery or radiotherapy of the breast because of possible scarring. The study was approved by the UW-Madison institutional review board (IRB) protocol number 2003-074.

Patient scanning was performed in a manner consistent with a normal breast ultrasound examination. The breast was scanned with the patient (typically) in the supine position with her ipsilateral arm behind her head. RF data were acquired during a freehand palpation or deformation of the breast using the ultrasound transducer. Patients were alert during the ultrasound scans and therefore could provide immediate feedback to the sonographer regarding discomfort due to breast deformation. Freehand compression of up to 10% using the ultrasound transducer was utilized.

A total of 37 patients were scanned. The mean age was 46.2 ± 13.6 years with age ranging from 20-87 years. The mean height and width of the lesions were 1.39 ± 0.72 cm and 1.27 ± 0.76 cm respectively obtained from the ultrasound B-mode images. Madsen et al. (2005) have reported that lesions as small as 0.2 mm can be detected with axial strain imaging in tissue-mimicking phantoms. Histopathological results of the biopsy performed were considered the reference standard in the cases analyzed; 8 malignant masses and 29 fibroadenomas were included.

For each case, 160 RF data frames were collected, from which we select consecutive frame pairs, with the best axial strain image quality (based on the normalized correlation coefficient value, see below). In general, only a pair of pre-and post compression frames are required to generate the axial strain and axial-shear strain images. All the data processing for axial-shear strain images discussed in this chapter was performed offline.

Table 6.1 Number of patients diagnosed with benign and malignant breast masses based on needle core biopsy results. This was a subset of the complete data set based on the B-mode images where the mass could be segmented by the ultrasound scientist.

Hospitals	Ultrasound system	Benign	Malignant	B/M
UW-Madison Hospitals and Clinics	Siemens Antares, VFX 13-5	29	8	29/8
Mayo Clinic	Siemens Elegra, VFX 13-5	6	17	6/17
Charing Cross Hospitals	Siemens Elegra, VFX 13-5	23	26	23/26
Kansas University Medical Center	Siemens Elegra, VFX 13-5	7	7	7/7

Beside data acquired at UW, the project included data from scans done at three other sites. These are listed in Table 6.1. Data acquisition at the other sites was similar to the RF data

acquisition discussed previously for the UW-Madison site. A Siemens SONOLINE Elegra system with a VFX13-5 linear-array transducer pulsed at 10MHz or the 7.5L40 linear-array transducer pulsed at 7.2 MHz (Siemens Healthcare, Malvern, PA, USA) was used. RF echo data from three hospitals (Mayo Clinic, Rochester, MN; location B; Charing Cross Hospitals, London, UK; location C; and University of Kansas Medical Center; location KU) are included in the analysis described below. The study at the Mayo Clinic was approved by the Mayo Foundation IRB, and was compliant with the Health Insurance Portability and Accountability Act (HIPPA). Data acquisitions at Charing Cross hospital were approved by Riverside research ethics committee, Chelsea & Westminster Hospital (NHS Trust, for Charring Cross Hospital). Data acquired at Kansas University Medical Center were approved by the appropriate IRB. Patient consent was obtained prior to any studies being performed. Details of the patients scanned are presented in Burnside et al. [34], where the database was utilized in a observer study of the SR feature.

Table 6.2 Histopathology

Types and subtype (123 RF cases)	No.
Malignant	
IDC	32
IDC & DCIS	5
DCIS	3
Invasive Lobular	5
Invasive Mammary	1
LCIS & DCIS	1
Metastatic Phylloides	1
Intracystic Papillary	1
Ductal CA	1
CA	8
Benign	
Fibroadenoma	65

The number of patient RF data sets utilized from the different hospitals is shown in Table 6.1. The ratio B/M denotes the number of Benign to Malignant cases in each institution. In the combined data set, we report on 65 benign cases and 58 malignant cases. (Elegra B: B/M = 6/17, Elegra CC: B/M = 23/26, Elegra KU B/M = 7/7, Antares: B/M = 29/8). Histopathological analysis of the tissue biopsy from the breast mass from the 123 patients are shown in Table 6.2. Histopathology results indicate that 58 cases were from patients diagnosed with a malignant breast mass and 65 cases were from patients diagnosed with a benign breast mass.

6.3 Axial Strain and Axial-shear Strain Imaging

RF echo data loops were used to track the underlying local tissue displacements resulting from the deformation induced when the sonographer applied pressure to the transducer to deform the breast. The estimation process is shown in Figure 6.1. Local axial displacements were estimated using a two-dimensional (2D) multi-level motion tracking algorithm [20, 150]. The first step involves estimation of a coarse displacement utilizing sub-sampled B-mode or envelope signals. This coarse displacement estimate is then used to guide the final cross-correlation stage on RF data. We used a 2D kernel with a 75% overlap to compute the cross-correlation function and to determine the final displacement estimate. The 2D kernel was approximately five wavelengths along the axial direction (0.77 mm) and three A-lines along the lateral direction. For each step of this algorithm, the normalized cross-correlation coefficient value was used as the matching criteria. The peak value of the normalized cross-correlation function at each step was recorded to generate an image of the local correlation coefficients. The axial strain and the axial-shear strain tensor were estimated using a least squares strain estimator (LSQSE) [126] as defined in equation 4.1. All RF data frames in the data loop were processed to obtain axial strain

and axial-shear strain images and corresponding correlation coefficient maps. The frame with the highest mean correlation coefficient was regarded as the frame that produced the best quality axial strain image and was used for the study.

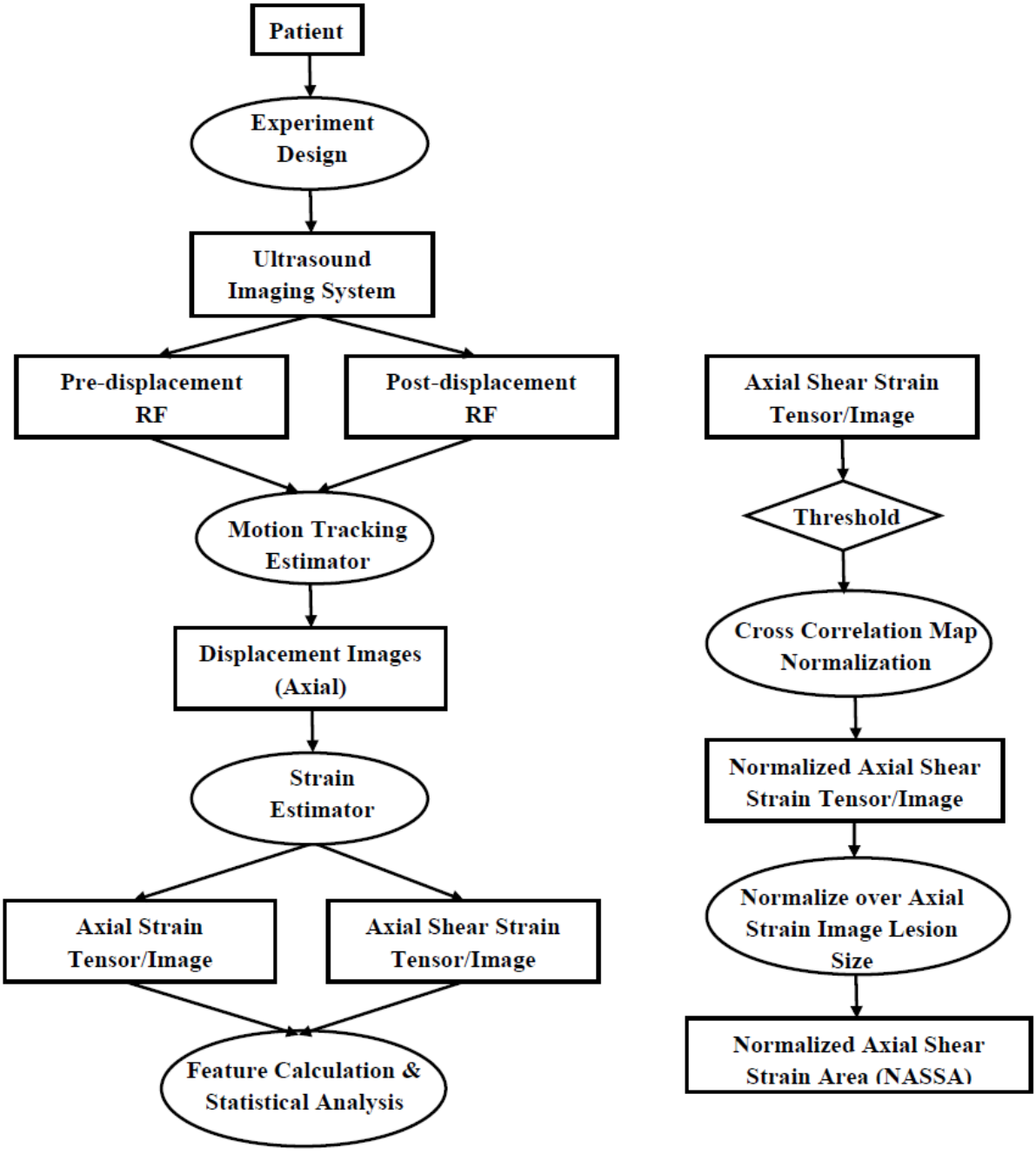

Figure 6.1 Flowchart for *in-vivo* RF data processing

Figures 6.2 and 6.3 present axial strain (a) and axial shear strain images (b) obtained from *in-vivo* data for two patients. One was diagnosed with a ductal carcinoma in situ (DCIS) tumor and the other had an invasive ductal carcinoma (IDC). Note that the axial shear strain tensor image for the carcinoma mass (Fig 6.2) exhibits axial shear strain areas with larger shear regions surround the lesion. Shear strain characteristics are similar to those described in both FEA simulations (Figure 3.4) and the phantom study (Figure 4.5) for firmly bound inclusions.

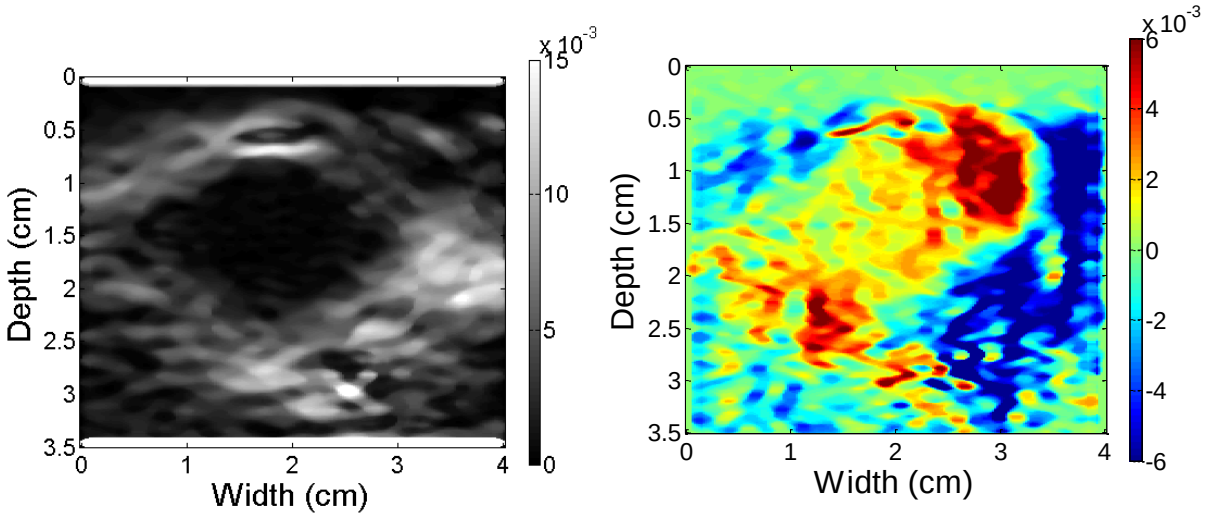

(a) (b)

Figure 6.2 Ultrasound axial strain (a), and axial shear strain image obtained from RF data of a patient diagnosed as having Ductal carcinoma in situ (DCIS). The colorbar range is the same for all the axial strain and shear strain images, where a 1% strain is depicted as a 0.01 level.

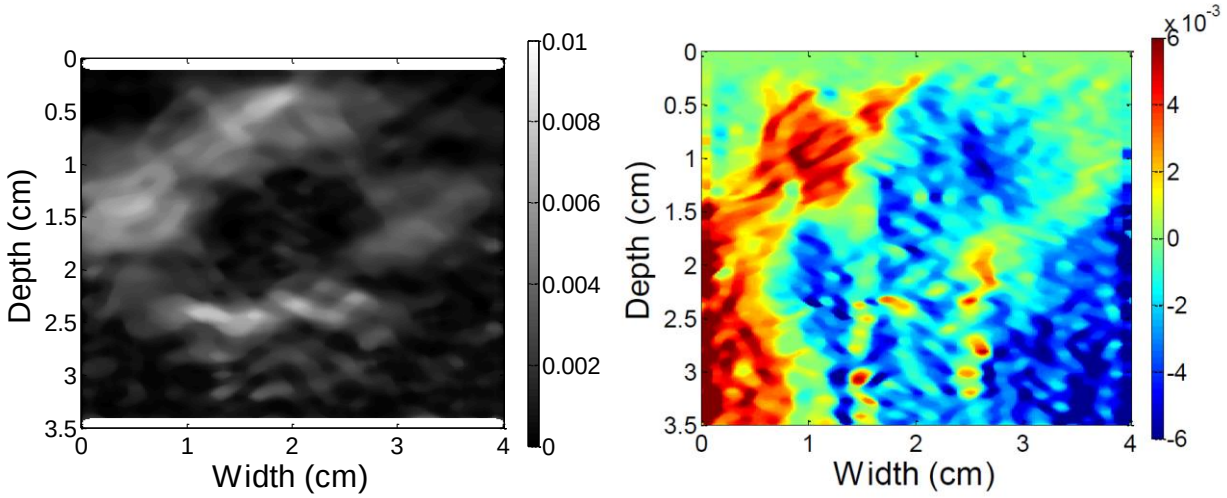

(a) (b)

Figure 6.3 Ultrasound axial strain (a), and axial shear strain image obtained from RF data of a patient diagnosed as having a invasive ductal carcinoma (IDC). The colorbar range is the same for all the axial strain and shear strain images, where a 1% strain is depicted as a 0.01 level.

Figures 6.4 - 6.6 present examples of axial strain (a) and axial-shear strain images (b) obtained from the data sets of patients diagnosed with fibroadenomas (benign masses loosely attached to surrounding tissue). Note the similarity of the shear strain patterns to those visualized with FEA simulations for inclusions with a low value of the friction coefficient (chapter 3-4) and the phantom study (chapter 4-5) for the loosely bound inclusions.

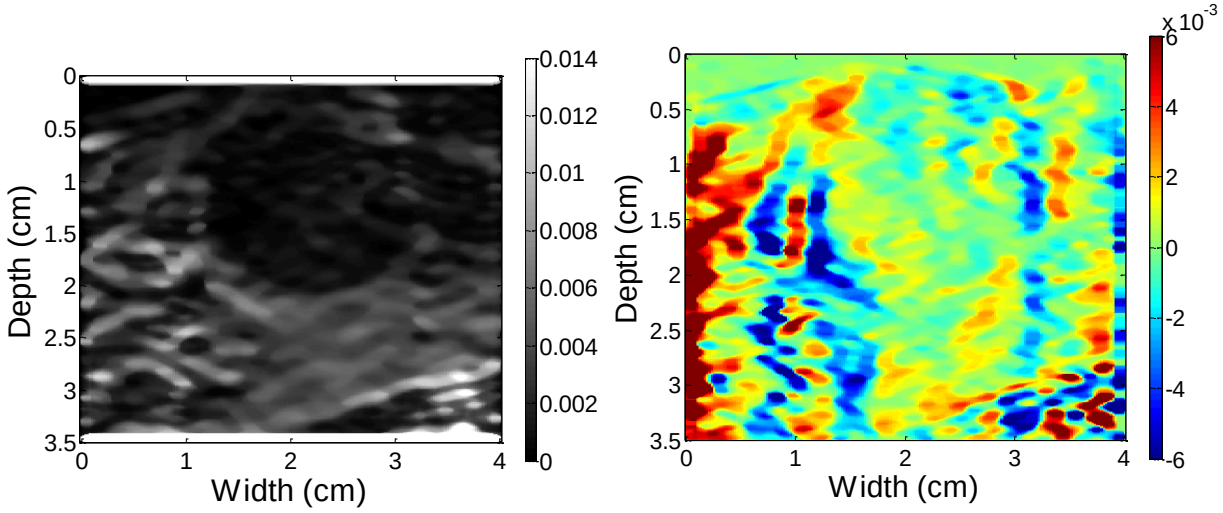

(a) (b)

Figure 6.4 Ultrasound axial strain (a), and axial shear strain image obtained from RF data of a patient diagnosed as having a fibroadenoma. The colorbar range is the same for all the axial strain and shear strain images, where a 1% strain is depicted as a 0.01 level.

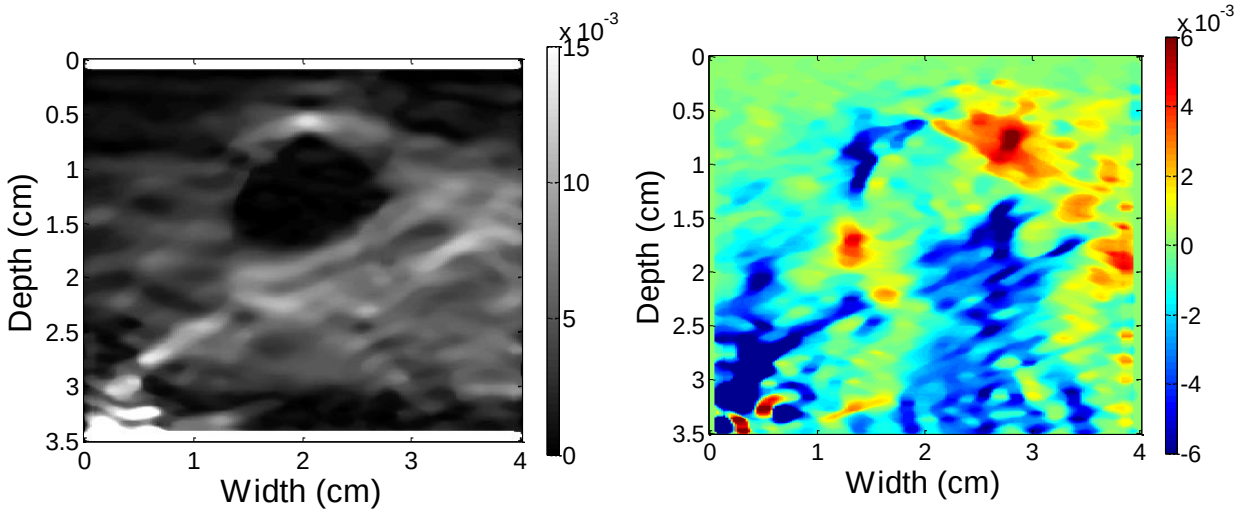

(a) (b)

Figure 6.5 Ultrasound axial strain (a), and axial shear strain image obtained from RF data of a patient diagnosed with a fibroadenoma. The colorbar range is the same for all the axial strain and shear strain images, where a 1% strain is depicted as a 0.01 level.

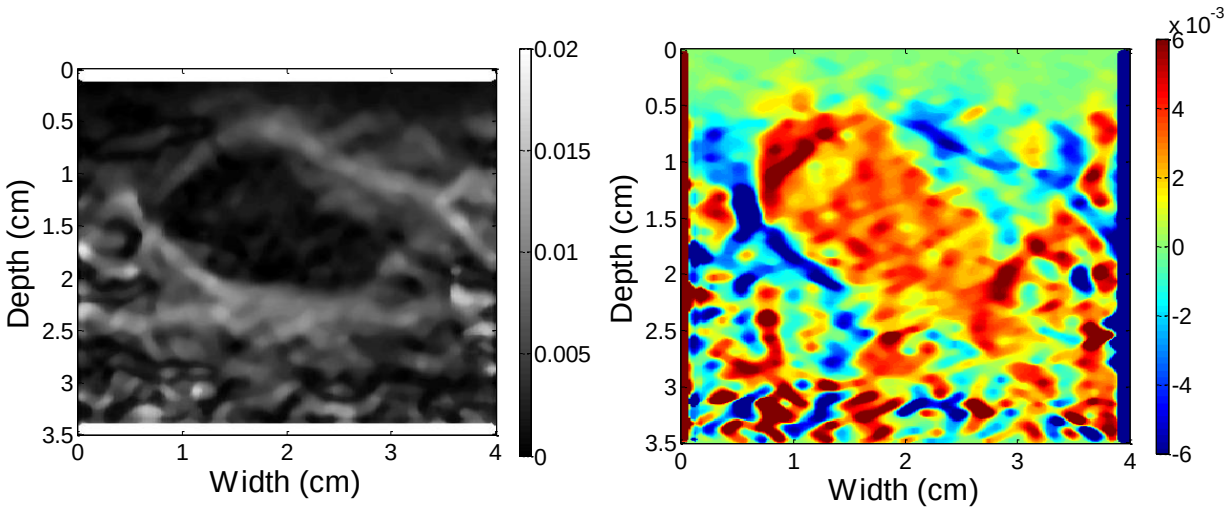

(a) (b)

Figure 6.6 Ultrasound axial strain (a), and axial shear strain image (b) obtained from RF data of a patient diagnosed with a fibroadenoma and sclerosing adenosis. The colorbar range is the same for all the axial strain and shear strain images, where a 1% strain is depicted as a 0.01 level.

The 'fill-in' shear strain pattern quantified as NASSA_IM within the mass is clearly observed in the benign mass that is asymmetrical to the applied deformation as shown in Figure 6.7. This also corresponds to the pattern reported using FEA and TM phantom studies (Figures 3.5 and 4.5). However, these 'fill-in' or NASSA_IM shear strain patterns also appear on malignant masses, as can be seen in both Figures 6.2 and 6.3, although this was not visualized on FEA and phantom results. In addition, with actual breast masses, we do not observe symmetric shear strain patterns in all of the quadrants around the breast mass. This may be due to different degrees of infiltration into the surrounding tissue for these masses. In addition, in many of the cases we observe more artifacts below the breast mass, probably due to the reduced ultrasonic signal-to-noise ratio under *in-vivo* imaging conditions. Note that the dark bands that appear on both the left and right sides of the axial-shear strain images, are introduced due to the finite length of the N points LSQSE estimation as discussed in chapter 4.

Several features extracted from the axial-shear strain images were computed to see whether they would help differentiate benign from malignant tumors. These are discussed in previous chapters. In this chapter, we will evaluate the feasibility of utilizing the "normalized axial-shear strain area (NASSA)" feature for *in-vivo* breast tumor diagnosis [20, 22, 151-152]. The normalization for applied axial compression and modulus contrast was done by setting the contour threshold for segmenting the axial-shear strain region as 20% of the mean applied axial strain times the background-tumor strain contrast as shown in Figure 6.1. This is discussed in chapter 3. Here the strain contrast is defined as the ratio between the mean axial strain estimated in the background to that estimated within the breast mass. Since the elastic modulus contrast is not known, we use the axial strain contrast to approximate the modulus contrast. The mean applied axial strain and the strain contrast were computed from the axial strain image. The mean applied strain is the same as the mean axial strain in the tissue background. The largest area of the breast mass was selected as the ROI for the mass, and two rectangular shaped ROIs at the same depth were selected for the background ROIs (Figures 6.7 – 6.13). The background strain was taken to be the average strain in these two ROIs. The mean axial strain value was then computed over the pixels within the selected ROIs.

For the computation of the NASSA feature, we utilize all the shear strain pixels within a square block that surrounded the mass delineated on the ultrasound axial-strain image. This is calculated to be the ratio of the summation of these pixel areas to the tumor inclusion area as seen on the B-mode image. In addition, a threshold cross correlation coefficient is utilized to further reduce the noise pixels in the axial-shear strain image, leaving only those pixels with axial-shear values greater than the normalized threshold and the corresponding normalized

correlation coefficient value greater than 0.75. These pixels were overlaid on the corresponding ultrasound axial strain image to obtain the composite image.

6.4 Normalized Axial-Shear Strain Area Feature

Figures 6.7 to 6.13 show examples of the ultrasound B-mode, axial strain, and axial-shear strain images superimposed on the corresponding ultrasound axial strain/B-mode images of malignant and benign breast masses. The blue regions indicate negative axial-shear strain values while the red areas represent positive values, which also represent the opposite direction to the applied deformation. The red dashed line shows the demarcated lesion boundary in both the axial strain image and the B-mode image. The blue dashed line shows the ROIs utilized to estimate the mean strain of the background region. In every case shown, the area of the axial-shear strain region is larger for malignant tumors than for benign masses. This finding is consistent with the result observed from simulations in chapter 3 [22]. Note also that the blue and red patterns occur further away from the borders of the malignant masses visualized on the corresponding B-mode image. This is in contrast to benign masses where the axial-shear strain patterns appear to be close to the lesion boundary. The location of the axial-shear strain patterns for malignant masses is consistent with the hypothesis that this is related to a desmoplastic reaction. The finding has, of course, been hypothesized to be a factor in the depiction of malignant breast masses having larger dimensions on measured axial strain images than apparent dimensions measured on the B-mode images [30, 32].

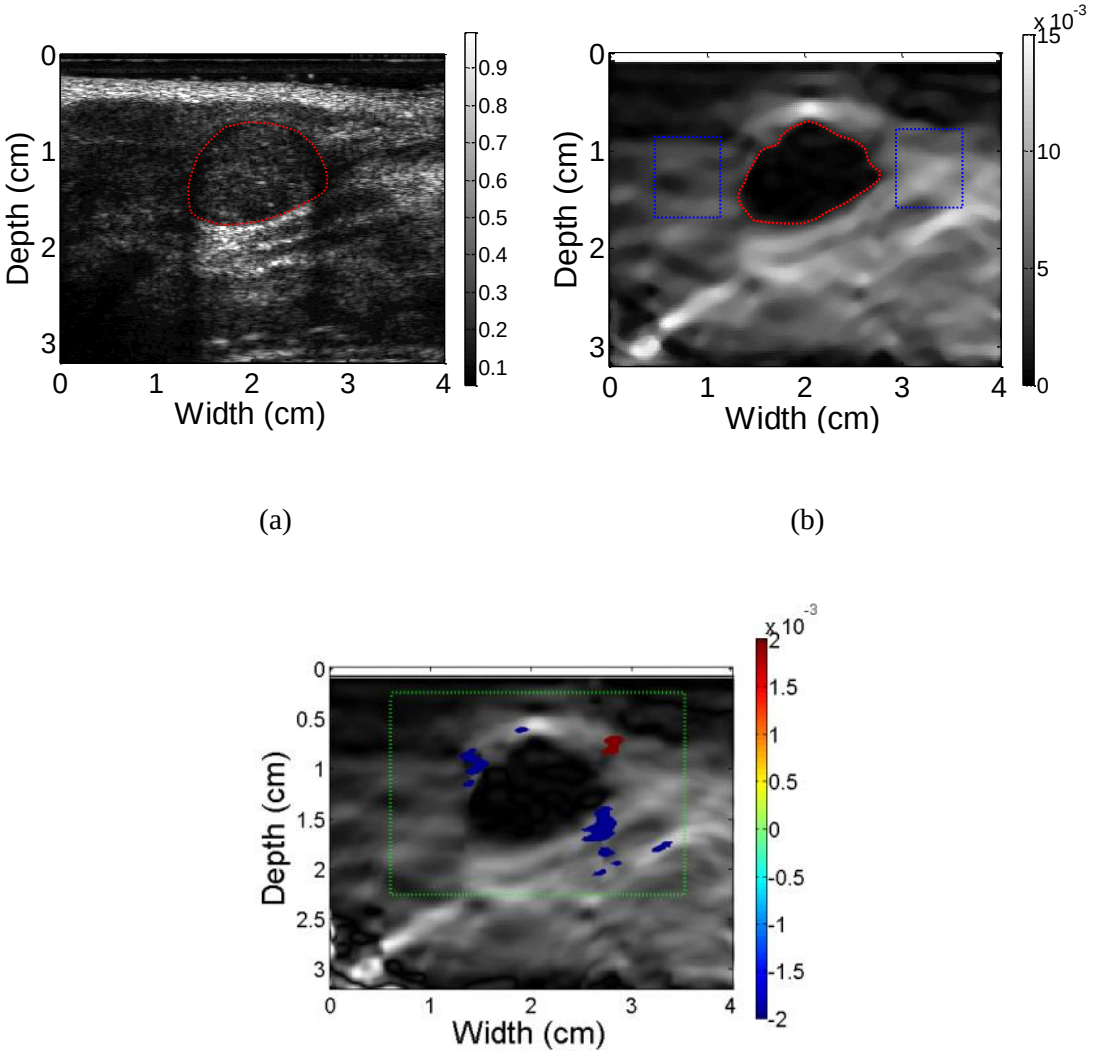

(a) (b)

(c)

Figure 6.7 Ultrasound B-mode (a), axial strain (b), and composite image obtained by superimposing the axial-shear strain data on the axial strain image (c) for a patient diagnosed with a fibroadenoma. In image c), positive axial shear strains are depicted in red and negative axial shear strains in blue. The NASSA value for this patient is 0.15. The colorbar range is the same for all the axial strain and shear strain images, where a 1% strain is depicted as a 0.01 level.

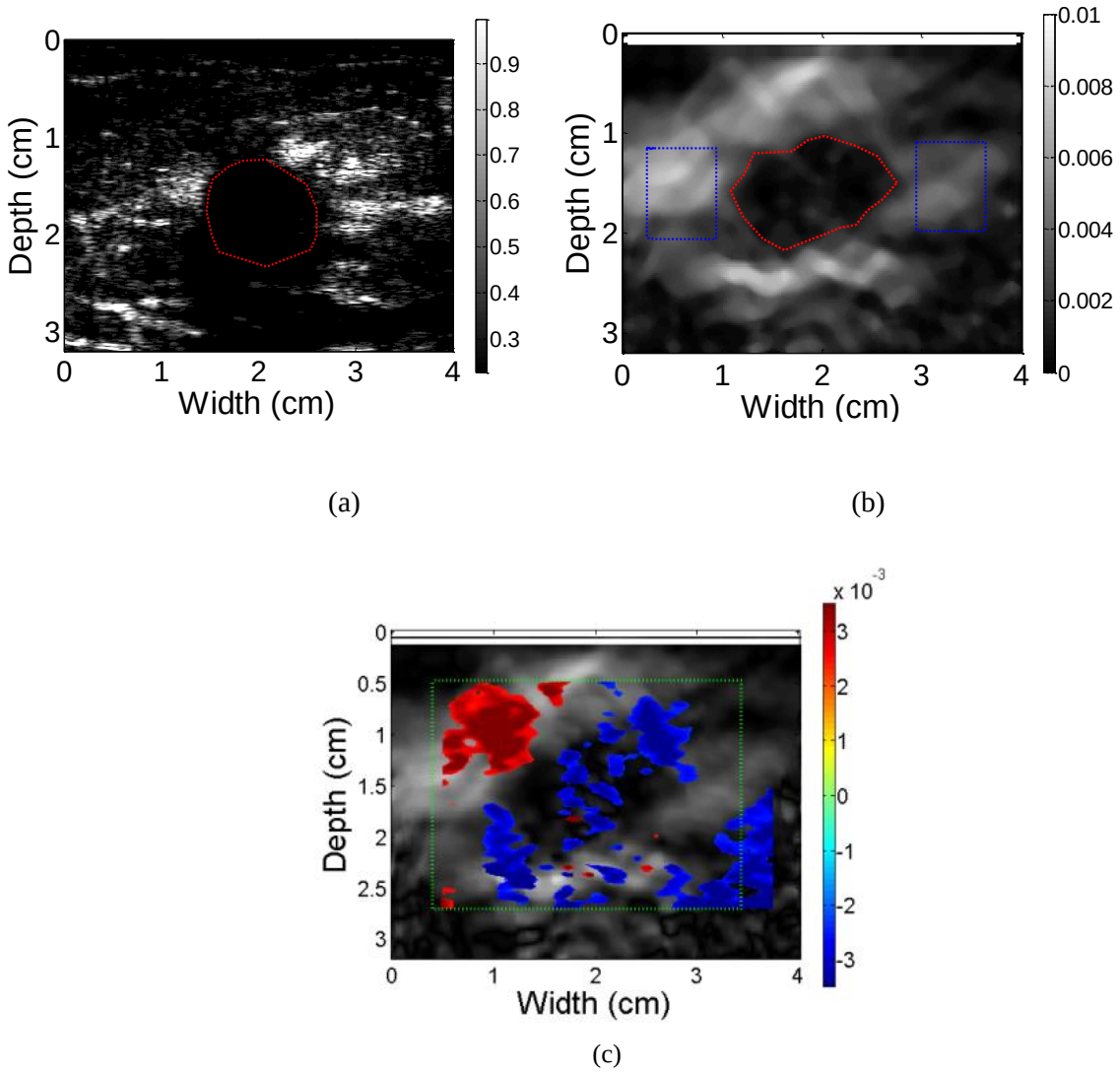

(a) (b)

(c)

Figure 6.8 Ultrasound B-mode (a), axial strain (b), and composite image obtained by superimposing the axial-shear strain data on the axial strain image (c) for a patient diagnosed with invasive ductal carcinoma (IDC). The NASSA value for this patient is 2.89.

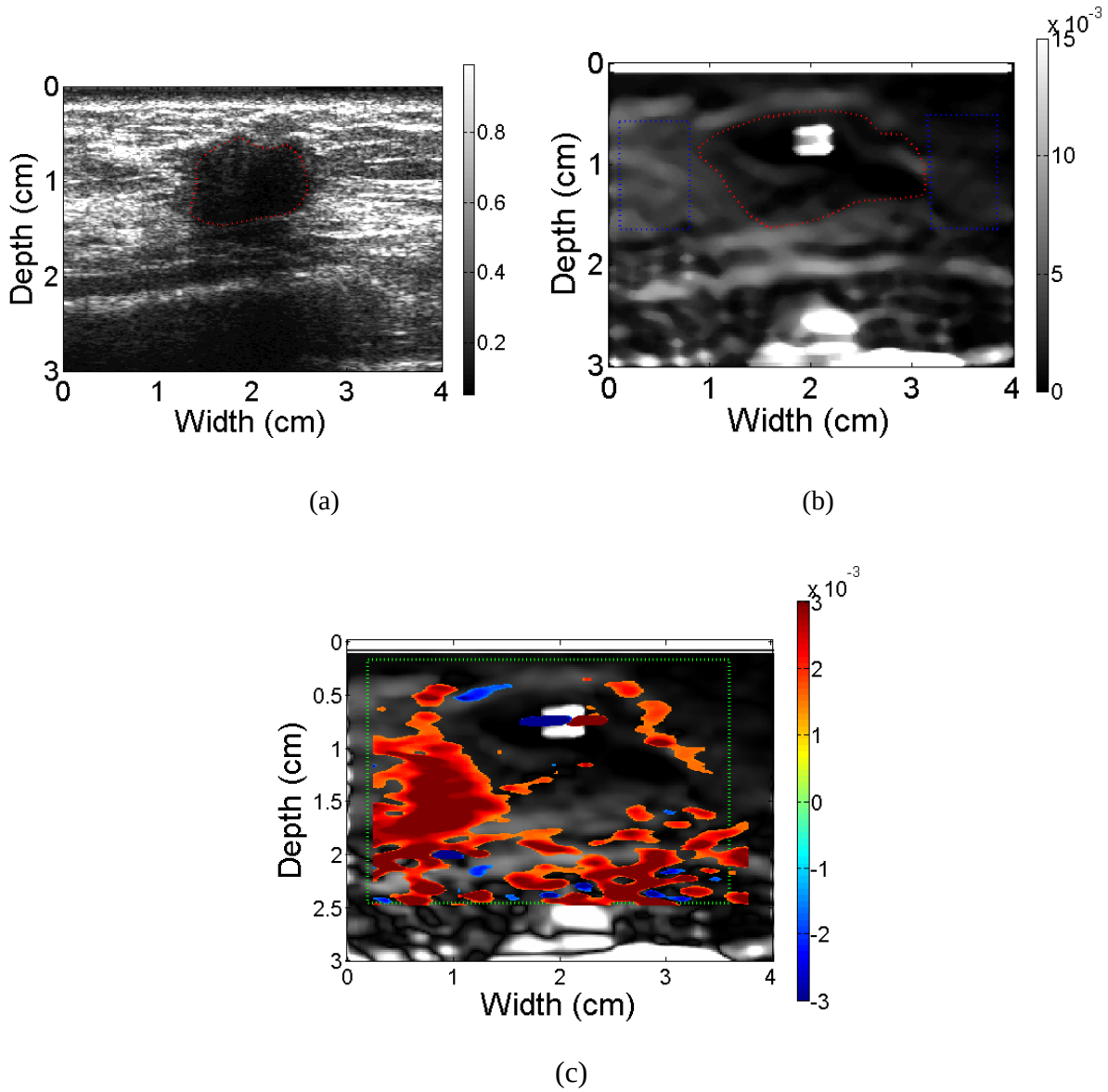

(a) (b)

(c)

Figure 6.9 Ultrasound B-mode (a), axial strain (b), and composite image obtained by superimposing the axial-shear strain data on the axial strain image (c) for a patient diagnosed with invasive lobular carcinoma. The NASSA value for this patient is 1.213.

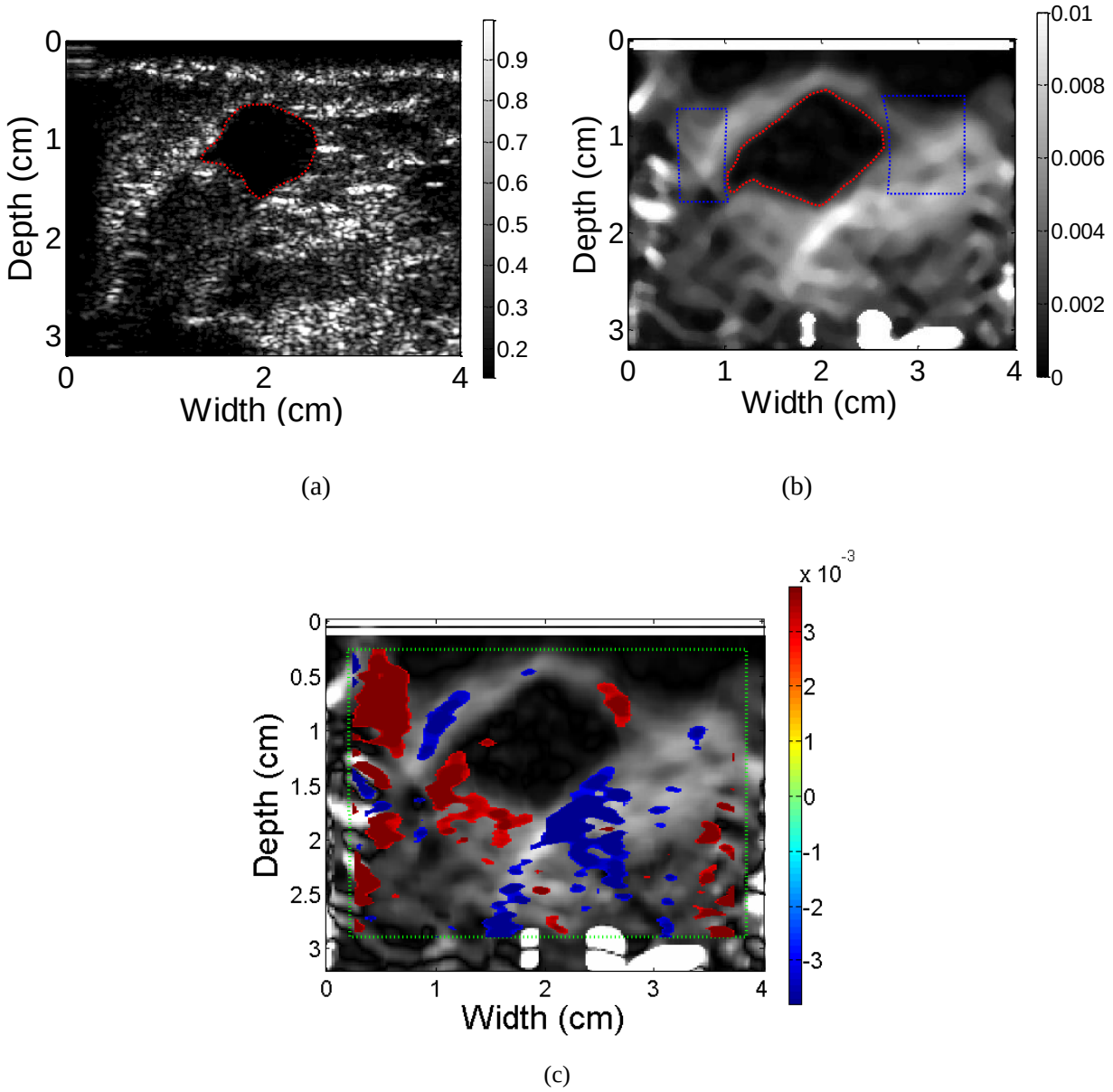

(a) (b)

(c)

Figure 6.10 Ultrasound B-mode (a), axial strain (b), and composite image obtained by superimposing the axial-shear strain data on the axial strain image (c) for a patient diagnosed with invasive ductal carcinoma (IDC). The NASSA value for this patient is 1.324.

In the *in-vivo* results for breast masses we do not observe symmetric normalized shear strain patterns in all four quadrants around the breast mass. This could be due to different degrees of infiltration into surrounding tissues for these masses. These results differ from simulation results shown in chapter 3 or the TM phantom results shown in chapters 4 and 5, where axial shear

strain imaging of masses that are fully bound or loosely bound to the background are presented. In addition, in many of the cases we only observe axial-shear strain patterns above the breast mass. This might be caused by complex *in-vivo* boundary conditions as well as a lower ultrasonic signal-to-noise ratio below the breast mass under *in-vivo* imaging conditions. However, in some instances, we are able to visualize the complete axial-shear strain pattern,, as illustrated in Figure 6.7, 6.8, 6.9. For benign masses such as fibroadenomas as shown in Figure 6.7, slippage is observed only around the boundary of the mass. In addition, while applying the deformation necessary for strain imaging, care is always taken to keep the breast mass within the imaging plane. Both of these factors contribute to the low levels of shear strain observed around the boundary of the fibroadenoma.

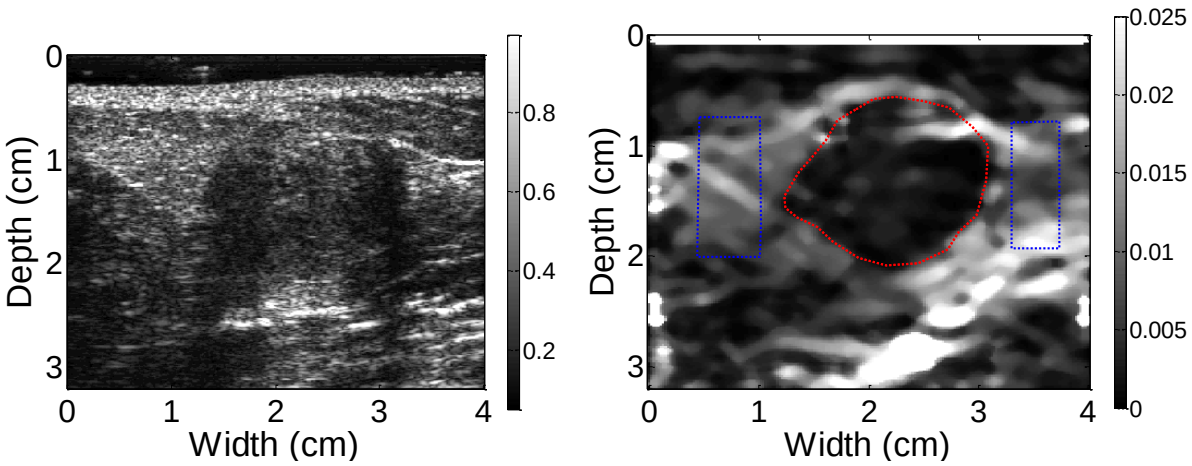

(a)

(b)

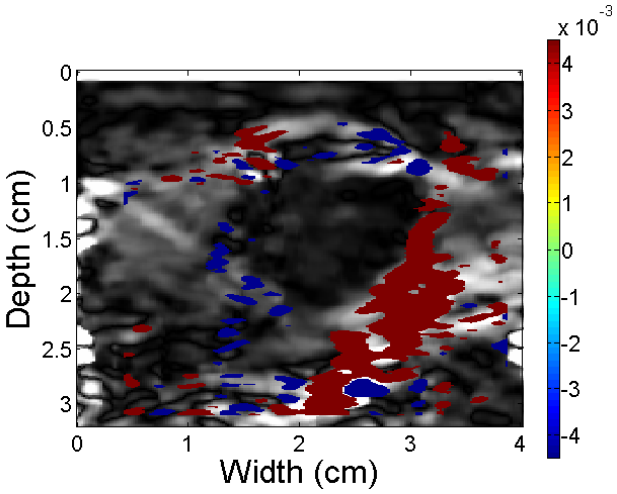

(c)

Figure 6.11 Ultrasound B-mode (a), axial strain(b), and composite image obtained by superimposing the axial-shear on the axial strain (c) for a patient diagnosed with a fibroadenoma. The NASSA value for this patient was 0.768.

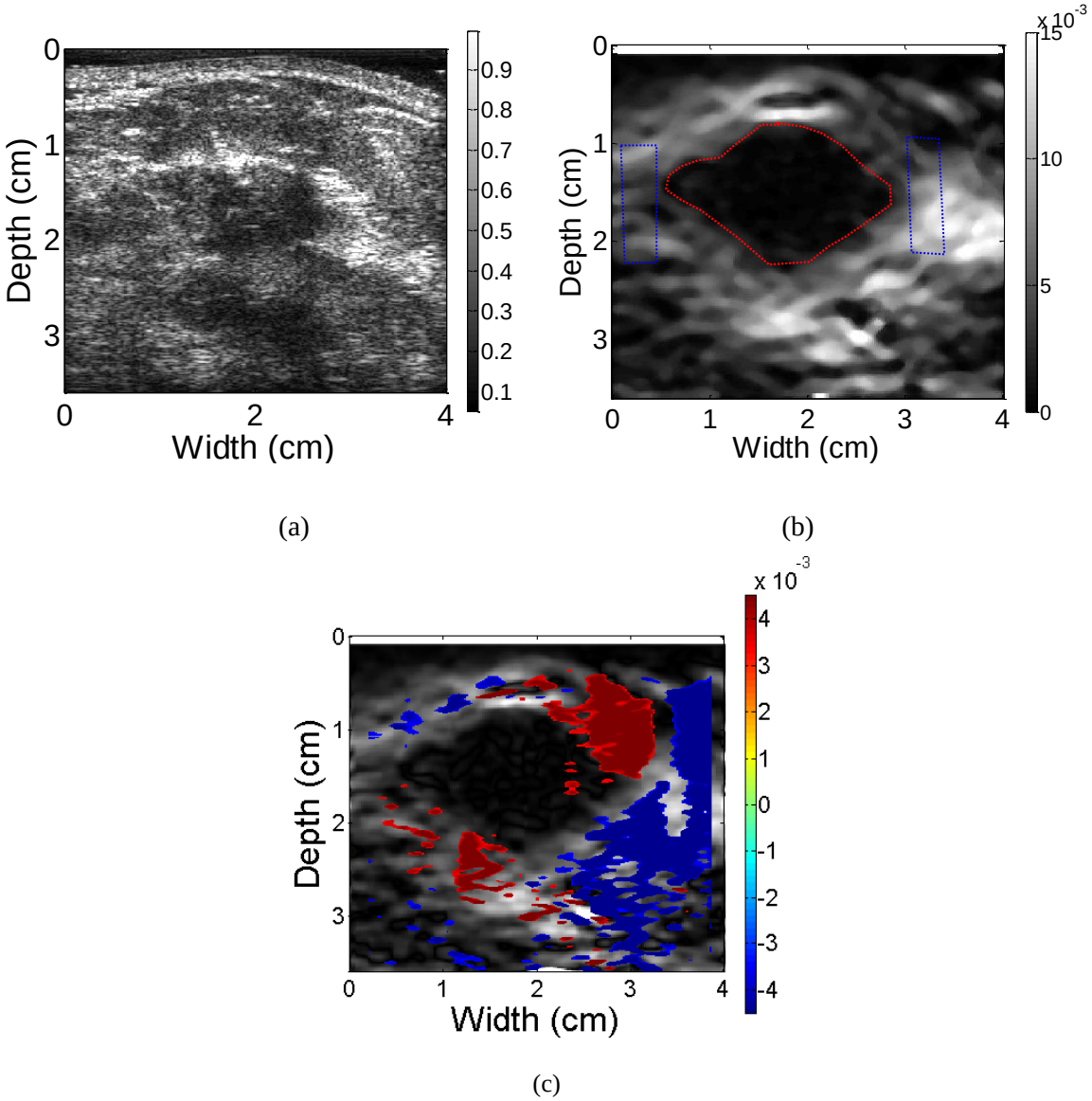

Figure 6.12 Ultrasound B-mode (a), axial strain(b), and composite image obtained by superimposing the axial-shear on the axial strain (c) for a patient diagnosed with an ductal carcinoma in situ (DCIS). The NASSA value for this patient was 1.53 suggesting this mass is malignant.

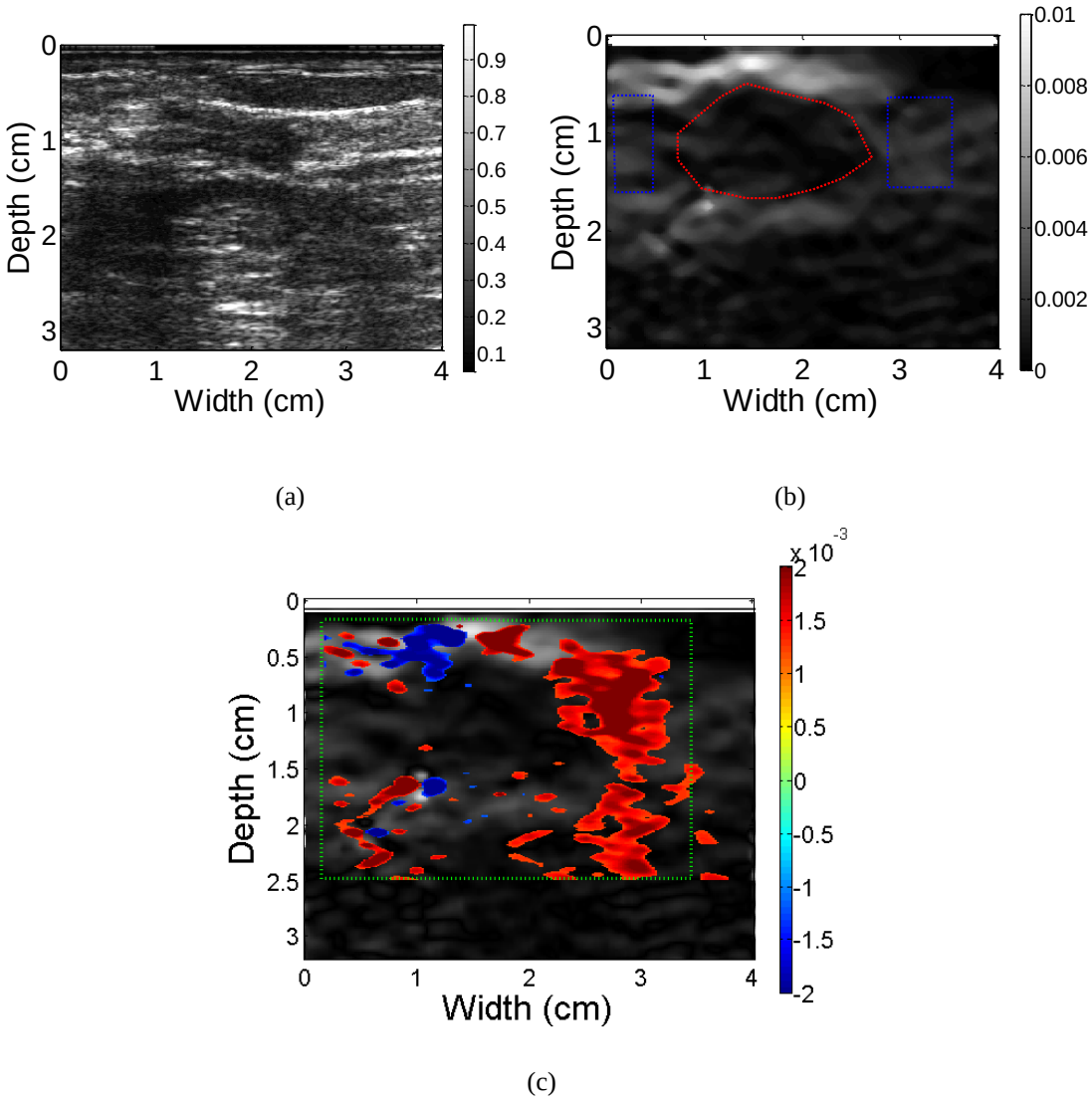

Figure 6.13 B-mode (a), axial strain (b), and composite image obtained by superimposing the axial-shear on the axial strain (c) for a patient diagnosed with carcinoma. Note the difficulty in visualizing the size or contour of the breast mass on the axial strain (a), but the mass is clearly seen on the strain image (b). However, the NASSA value of 1.41 identifies this mass as malignant.

Also note that normalization of the shear strain features using features from the B-mode image is complicated by the fact that identification of the breast mass extent from B-mode images is quite difficult in many cases. Examples of such case are shown in Figures 6.11 - 6.13. The breast mass in Figure 6.13 is almost indistinguishable in B-mode, with a very small region

being identified. However, the mass is clearly seen on the axial strain image, and the larger NASSA feature value of 1.41 suggests that this mass may be malignant.

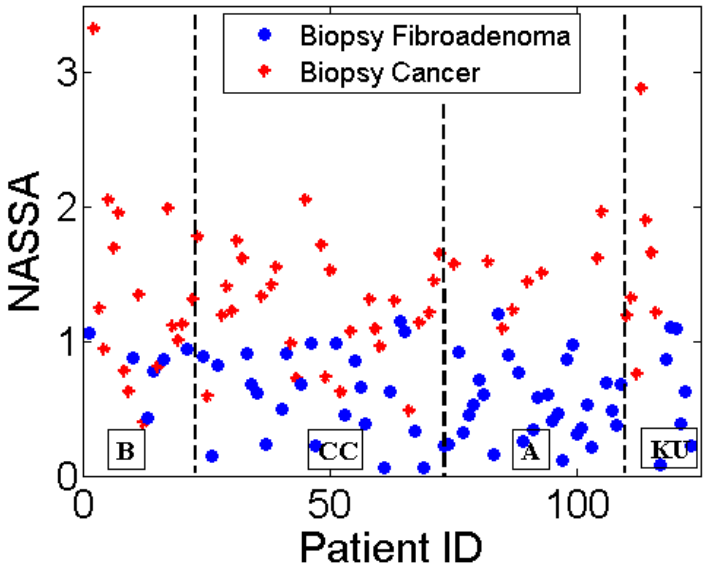

Figure 6.14 Scatter plots of *in vivo* differentiation between patients with cancers and fibroadenomas using the NASSA feature on a combined data set (where B, CC and KU denote Elegra data obtained from three different clinical hospitals and A denotes Antares data).

Figure 6.14, presents scatter plots of the NASSA feature values for all 123 patients in this study. Cases are separated according to the different institutions over which the data were collected. The x-axis of the scatter plot represents the patient ID from the four institutions, while the y-axis represents the computed NASSA feature values. The scatter plot shows that most of the malignant masses exhibit a NASSA value greater than 1.2, while most benign masses have a NASSA value less than 1.2.

ROC analysis was also performed using the NASSA values obtained from the patient data sets. The reference metric for differentiation was the pathology report from a core needle biopsy obtained on the patient. For the ROC analysis, we choose the NASSA values for the 58 malignant tumors (identified by 'M') as the true category and the NASSA values of the 65 benign

tumors (identified by 'B') as the false category. We set a threshold that increases from 0 to the maximum NASSA value, and the step increase was set to 0.001. The true positive faction (TPF) represents the rate of truly classified positive cases during each step. Similarly, the false positive fraction (FPF) denotes the rate of benign breast masses being falsely classified as positive cases during each step. Finally we plot TPF along the y-axis and 1-FPF along the x-axis to obtain the ROC curve. The AUC is a nonparametric value that describes the performance of the test.

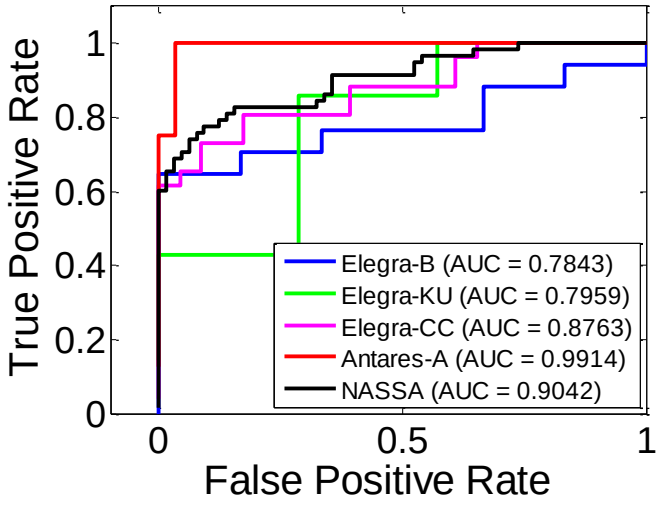

Figure 6.15 ROC curves for the NASSA obtained from Mayo clinic (B/M = 6/17) (blue curve), Kansas University Medical Center (B/M= 7/7) (green), Charing Cross Hospitals (B/M = 23/26) (purple), UW-Madison Hospitals and Clinics (B/M= 29/8) (red) and their combined data sets for 123 patients (B/M= 65/58) (black). B/M stands for Benign case numbers/Malignant case numbers.

The ROC results for the NASSA features obtained from patient data from the four different hospitals as well as their overall performance, are illustrated in Figure 6.15. For 23 *in-vivo* data sets (Benign case numbers/Malignant case numbers (B/M = 6/17) obtained from Mayo clinic, the AUC is 0.78; 14 *in-vivo* data sets (B/M= 7/7) obtained from Kansas University Medical Center provides an AUC value of 0.78; the AUC of 49 *in-vivo* data sets (B/M= 23/26) obtained from Kansas University Medical Center is 0.88; the AUC of 37 *in-vivo* data sets (B/M= 29/8) acquired from UW-Madison hospitals and clinics is 0.99. The combined data sets (B/M=65/58) yield a

AUC value of 0.90. Among these centers, the two smaller data sets (Mayo clinic: 23, Kansas University Medical center: 14) present much smaller AUC values when compared to data sets for the other groups. This is due to the existence of outliers that affect the smaller data sets more than larger data sets. Figure 6.16 presents ROC analysis based on which scanners were used for data acquisition. The AUC for 86 *in-vivo* data sets (B/M = 36/50) obtained using the Siemens Elegra system was 0.85, while the AUC for 37 data sets (B/M= 29/8) utilizing the Siemens Antares system was 0.99. However, note that the results obtained using the Elegra system were based on a larger number of data sets than the number using the Antares system. Thus, a larger patient data obtained using the Antares system would be necessary to demonstrate that for the same feature values, newly imaging system, potentially with higher resolution would improve the discrimination performance.

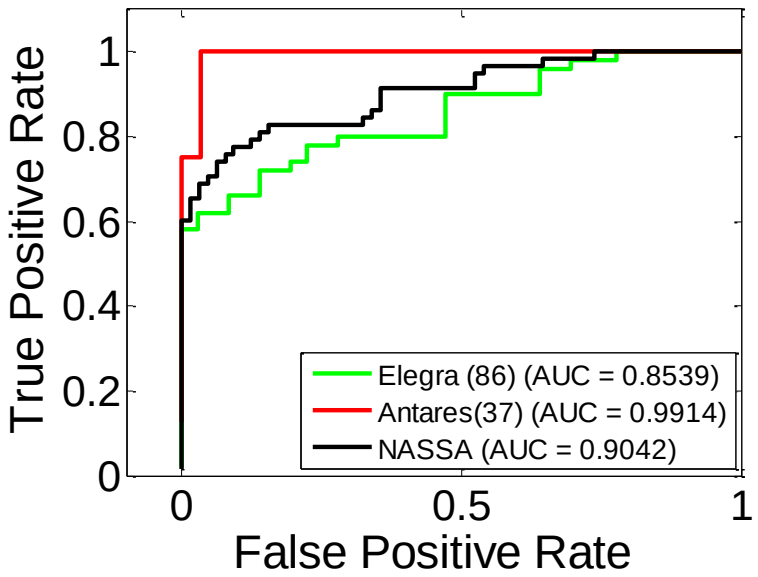

Figure 6.16 ROC curves for the NASSA feature obtained using the Siemens Elegra system (B/M = 36/50) (green curve), Siemens Antares system(B/M= 29/8) (red) and combined data set for 123 patients(B/M= 65/58) (black).

6.5 Discussion

In this chapter we illustrate the feasibility of obtaining axial-shear strain images under *in-vivo* imaging conditions. Both axial strain and axial-shear strain images were obtained from the same RF pre- and post-deformation data set. Axial-shear strain images exhibit features corresponding to FEA and Phantom results. The axial strain image provides information on the dimensions of the tumor and tumor/background strain contrast, which is utilized to normalize the axial-shear strain area feature obtained from axial-shear strain images. The results show that one "NASSA" feature, exacted from axial-shear strain images, exhibits values larger than 1.2 for most malignant cases, while most of the benign cases studies exhibit a NASSA feature value less than 1.2. Thus the axial-shear strain images provide additional information along with axial strain and B-mode images, to improve the performance of breast tumor classification.

In this chapter, the data acquisition involved free-hand deformations, which is convenient to perform but is more likely to introduce errors due to lateral and elevational tissue motion. A total of 90 to 160 RF frames were acquired for each patient and used to estimate frame to frame axial displacements and hence, strains. However, only axial strain and axial-shear strain images with high values of the normalized correlation coefficient value were selected for classification. Stepper motor controlled compression could be applied to obtain a specified deformation increment using fewer data sets for processing. Another advantage of motor controlled compression is that the applied deformation is known and there is no need to estimate the average compression from the axial strain image, as was measured in this study. This would also make it easier to set the threshold for segmenting the axial-shear strain region. However, stepper motor controlled compression require five degrees of freedom (three translational and two

rotational motorized stages for adequate motion control and is not as flexible as freehand scanning of the patient.

In order to avoid bias in the choice of the axial-shear strain region, a computer based feature selection approach was utilized. As shown in Figures 6.9 and 6.13 we do not obtain a symmetric pattern in all the quadrants around the tumor as depicted in the simulation results shown in chapter 3 and phantom results shown in chapter 4 and 5. Therefore, we take into consideration the entire area of the axial-shear strain region that overlaps on the B-mode image to estimate the NASSA value rather than choosing one or two quadrants as described by [124]. In addition, all pixels with NASSA values greater than the threshold value and corresponding correlation coefficient values greater than 0.75 were selected to be overlaid on the ultrasound B-mode image.

The entire data set used for the *in-vivo* classification study consisted of 65 benign and 58 malignant breast tumor cases. Even though the size of the data set reported is not large, the preliminary data demonstrates the potential of axial-shear strain elastography for the classification and differentiation of breast masses. It is expected that we would encounter an increased variety of axial-shear strain distribution patterns with an increase in the data set. However, the discriminant feature value, namely NASSA, should be stabilized by incorporating additional studies on larger patient datasets that involve more observers. Close inspection of the malignant masses in our population may also prove instructive. As expected, the majority of malignancies were invasive ductal carcinoma (32) but two interesting histological subtypes were encountered in our dataset: a ductal cancer, and an intracystic papillary carcinoma. Each of these malignancies is low grade, has a low risk of positive margins at definitive surgical resection, and

carries a substantially improved prognosis. Interestingly our axial-shear strain data indicates firm attachment of the tumor to the background tissue for both of these cases. In addition, our single case of lobular carcinoma, a malignancy that is well known to be more extensive on pathology than on imaging shows high axial-shear strain. This possibly indicates disease beyond the margins identified on B-mode imaging, as illustrated in Figures 6.7 and 6.13. Based on the preliminary data presented in this chapter, axial-shear strain imaging may be valuable in assessing the extent of disease beyond the image margins, thus more accurately assessing their size as well as differentiating benign from malignant tumors. Further research to validate this hypothesis is warranted.

Improvements in the signal-to-noise ratios in the axial-strain and axial-shear strain images can also significantly improve the classification performance. For the ROC analysis reported with the RF data acquired using the Siemens Antares system in Xu et al. [22, 151] we obtained an AUC value of 0.99, but with a small data set. The RF data obtained with the Antares have improved electronic SNR when compared to data acquired with the Siemens Elegra system. Figure 6.16 suggests a higher value for the AUC during ROC analysis for the Antares data than the Elegra data. Thus a larger data set can further demonstrate the feasibility of using NASSA for breast tumor classification. In addition, for axial-strain and axial-shear images generated for *in-vivo* breast masses the mass definition and shear strain patterns below the mass are not always clearly defined. In some instances significant noise artifacts are observed below the mass. Approaches such as angular compounding [51, 73, 153] that can improve the elastographic signal-to-noise ratio may improve mass delineation and reduce noise artifacts in the discriminant features. If so, this may lead to improved differentiation and classification of breast masses.

Chapter 7:

Statistical Analysis for Breast Mass Classification

7.1 Introduction

Emerging non-ionizing and noninvasive ultrasound based approaches are immensely important because of the need for sensitive methods to differentiate breast masses [154-155]. In the previous chapters 3-5, we have demonstrated the feasibility of utilizing both a "NASSA" feature derived from axial-shear strain imaging and "NFSSA" feature obtained from full-shear strain imaging for breast tumor classification. Previous results indicate that axial-strain imaging may improve breast mass classification [30-33] utilizing the stiffness contrast (CN: defined as the ratio of the lesion stiffness to that of normal background tissue estimated from the axial strain image) [30, 156] and the "size-ratio" (SR: defined as the ratio of the lesion area on the axial strain image to that obtained on the B-mode image) [26, 30, 32, 34-35]. Many benign breast masses such as fibroadenomas and fibrocystic nodules tend to have low CN values with mechanical testing, while cancers frequently are stiffer than surrounding breast tissue [55]. However, some fibroadenomas, have similar modulus distributions as infiltrating ductal carcinomas [55]. Hence, the CN feature obtained from axial strain imaging alone likely will not provide sufficient information to assess the malignancy of a detected lesion [32]. The size ratio

Material in this chapter was adapted from:

Xu, H., Varghese, T., J, Jiang., J.A. Zagzebski., "In vivo classification of breast masses using features derived from axial-strain and axial-shear images," Ultrason Imaging **34**, (2012):p. 222-236

feature was first described by Garra et al. [30]. It utilizes discrepancies between the size of a lesion on a B-mode image and the size on a corresponding axial strain image to distinguish benign from malignant lesions. Malignant lesions tend to appear larger on axial strain images when compared to their depiction on B-mode images, while benign lesions usually appear smaller or of the same size on axial strain than on B-mode images [30, 32]. This difference in size ratio between benign and malignant lesions has been attributed to axial-strain images also depicting regions around the tumor that have undergone desmoplastic reaction and have become stiffer [30, 32], while these changes are not captured on B-mode images.

We have shown the ability of the NASSA feature for breast mass differentiation in Chapter 6. The ability of CN, SR and NASSA as individual features for breast lesion differentiation has been investigated in several clinical studies [20, 22, 26, 30-32, 34-35, 151, 157-158]. In this chapter, our objective is to evaluate the utility of combining these three features for the differentiation of benign breast masses from malignant breast cancers *in-vivo*. The three features are evaluated both as single features as well as in different possible combinations to determine possible improvements in differentiation performance. Performance for all possible combinations are quantitatively evaluated using the area under the curve (AUC) describing the receiver operating characteristic (ROC) [140-143] for the feature combination. The ROC curve is generated by assuming the malignant cases and the benign cases follow (overlapping), normal distributions [144-149]. The AUC may be interpreted as the average value of the sensitivity over all possible values of the specificity (between 0 and 1) or vice-versa.

In this chapter, ROC analysis was used to investigate the potential for lesion classification based on analysis with single parameters and combination of parameters. ROC analysis was

performed using both LIBSVM [159] and ROCKIT software (Version 1.0.3 beta, Kurt Rossmann Laboratories, University of Chicago, Chicago, Illinois) to estimate classification performance. Since only a small number of biopsy-proven malignant cases were available, the data set was not separated into training and testing groups. Instead, ROC analysis was performed using a leave-one-out classifier to estimate the potential of these features both individually and in combination for breast mass differentiation. The leave-one-out excludes the data from the patient being tested when training the classifier, and then tests the classifier performance on that excluded data set. This process is repeated across the entire data set to obtain an estimate of the average performance of the classifier. The training and testing is therefore performed on different data sets, thereby producing a conservative estimate of the feature's performance.

7.2 Methods

As discussed in chapter 6, RF echo signal data sets from 123 patients, acquired from four different hospitals were utilized in this study, and previously shown in Table 6.1. RF echo data loops were used to derive the underlying tissue displacements to compute an axial strain and an axial-shear strain image as discussed in chapter 6. The CN was calculated as the ratio of the mean strain estimated within an region of interest (ROI) in the breast mass to the corresponding average in background ROIs on either side of the mass [20, 151]. The largest area of mass was selected as the ROI in the breast mass, at the same time, two rectangular shaped ROIs at the same depth were selected for the background ROIs. The applied strain was determined from the average strain in the background ROIs. The SR is defined as the ratio of the largest area of the mass on the axial strain image to that on the B-mode image. An axial-strain image with the maximum cross correlation map and with the most obvious boundary was selected for analysis.

The corresponding B-mode and axial-shear strain image were used to estimate the NASSA feature respectively. Lesion areas were segmented manually on these B-mode and strain images using Matlab software. Fibroadenomas generally appear as lesions with similar areas on both B-mode and strain images such that SR ≈ 1 or lower. On the other hand carcinomas typically appear larger on the strain image when compared to the B-mode depiction and thus would have a SR greater than 1.

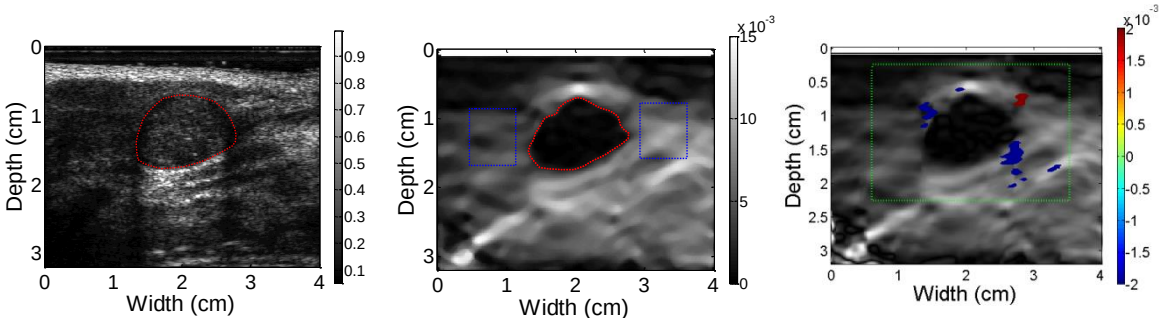

(a) (b) (c)

Figure 7.1 B-mode (a), axial strain (b), and composite image obtained by superimposing the axial-shear on the axial strain (c) for a patient diagnosed with a fibroadenoma. Note that the NASA value for this patient was 0.15, the SR was 0.87, and the CN value was 6.77.

Normalization of the axial-shear strain area has been previously described in chapter 6. The applied strain for normalization was estimated from ROIs in the background tissue which, along with an ROI in the breast mass, was also used to estimate the CN value. The composite image of the axial-shear patterns superimposed on the B-mode and axial-strain image depict locations where the axial-shear estimate exceeds a threshold set at 20% of the applied deformation [20, 22, 151], and possesses a normalized cross-correlation coefficient value greater than 0.75 to ensure high signal-to-noise ratios for the NASSA feature values [157-158]. In the composite image, areas depicted in red represent positive values of the axial-shear, while those in blue depict negative or opposite shearing strains. An example is shown in figure 7.1.

ROC analysis was used in this study to evaluate the accuracy, sensitivity and specificity of the CN, SR and the NASSA features to differentiate benign from malignant breast masses. A classifier that utilizes the leave-one-out approach was first utilized [140, 142]. For ROC analysis, the reference metric for differentiation was the pathology report from core needle biopsy obtained on the patient. We used the LIBSVM library[159] for the implementation of a linear support vector machine (SVM) using MATLAB (The Mathworks, Natick, RI). *In-vivo* data together with feature values and the class or biopsy label (±1) were organized into N (equal to the total number of patient data sets) data sets using a leave-one-out approach; i.e. we sequentially chose a patient data set as the validation data set, and all the remaining N-1 data sets as the training set. A linear SVM [160] classifier using a C value of 1 was used to train the training set. The validation data set was tested based on the training set to obtain a decision value and the predicted label (±1). Finally, the decision value and class label for all of the validated data sets were sorted and used to plot the ROC curve and to calculate the AUC. Since each patient data set was only tested once, the accuracy is estimated from the percentage of cases that were correctly classified from the entire testing dataset (N). ROC analysis for a single feature (CN, SR, NASSA) or that using combined features (SR & CN, SR & NASSA, NASSA & CN, NASSA & SR & CN) were performed using leave-one-out independently. In addition, specificity at 100% sensitivity was also computed from each trapezoidal ROC curve.

For single features, ROCKIT software was also used to estimate the upper and lower boundary of classification at a 95% confidence interval, along with the sensitivity and specificity. The two sides of 95% confidence interval for each AUC were estimated using the nonparametric bootstrap method.

A two sample t-test with two separate and independent groups comprising the benign and malignant patients was utilized to evaluate the statistical significance of the results. For the t-test analysis, we set the feature values of benign tumors as a group, while the feature values of patients diagnosed as malignant tumors comprise the second group. The two groups have different sample sizes and are assumed to be independent with unequal variance. The Null Hypothesis is that the mean feature value (NASSA/SR/CN) of benign masses is larger than or equal to the mean feature values of the malignant masses.

7.3 Results

Figure 7.1 presents imaging results for a benign breast mass. Shown from left to right are the B-mode image, the axial-strain image and the axial-shear images superimposed on the corresponding axial-strain image. The red dashed lines indicate the inclusion boundary generated in both B-mode and axial-strain images. The blue dashed line shows the ROIs utilized to estimate the mean strain of the background region. The green dashed region indicates the selected normalized axial-shear strain region. The CN estimated from the axial-strain image, was 6.77 and the SR was 0.87. The NASSA value computed for this patient was 0.15. Figure 7.2 presents analogous images for a patient diagnosed with invasive ductal carcinoma. For this patient, the CN value was 4.58, the SR value was 1.08, and the NASSA feature value was 2.89. Note that the CN for this mass is lower than the value for the benign mass in figure 7.1. Importantly, the SR is greater than 1, and the axial-shear strain region is significantly larger for this mass than for the benign mass in figure 7.1.

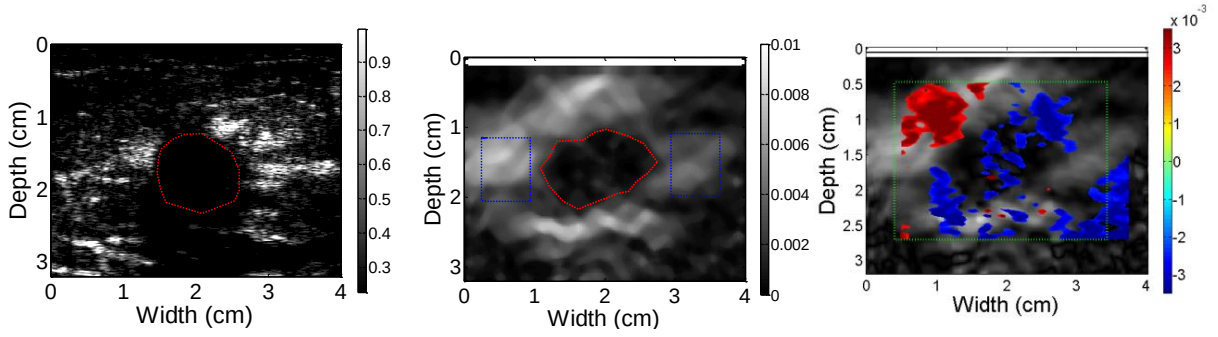

(a) (b) (c)

Figure 7.2 B-mode (a), axial strain (b), and composite image obtained by superimposing the axial-shear on the axial strain (c) for a patient diagnosed with invasive ductal carcinoma. Note that the NASSA value for this patient was 2.89, the SR was 1.08 and the CN value was 4.58.

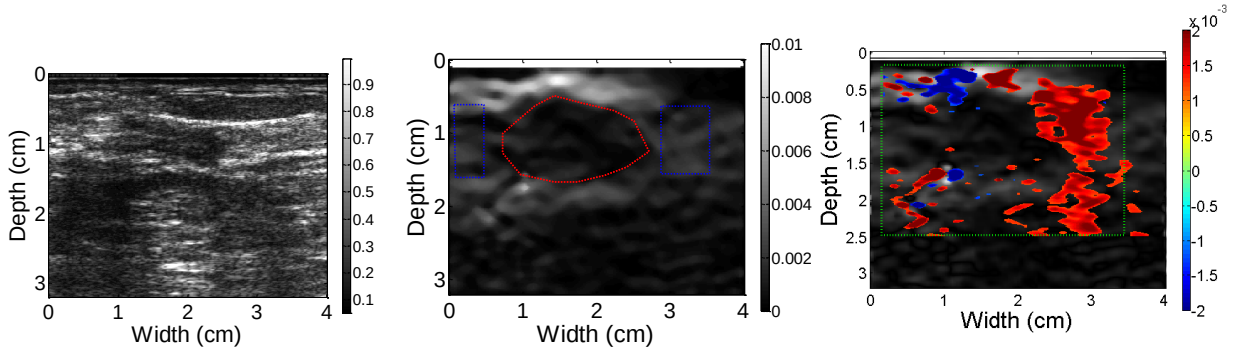

(a) (b) (c)

Figure 7.3 B-mode (a), axial strain (b), and composite image obtained by superimposing the axial-shear on the axial strain (c) for a patient diagnosed with carcinoma. Note the difficulty in visualizing the size or contour of the breast mass on the B-mode (a), but clearly seen on the strain image (b). However, the NASSA value of 1.41 identifies this mass as malignant. The CN is 2.19.

Calculation of the SR is complicated by the fact that identification of the breast mass extent from B-mode images is quite difficult, as shown in Figure 7.3 for a patient diagnosed with a carcinoma. The breast mass is almost indistinguishable in B-mode with a very small region being identified. However, the mass is clearly seen on the axial-strain image, and the NASSA feature value of 1.41 suggests that this mass is malignant. The CN was 2.19. Diagnosis based on the SR feature in Figure 7.3 fails to provide accurate differentiation results. The SR estimate is biased by the poor boundary delineation on the B-mode image. The NASSA feature on the other hand accurately classifies the breast mass as malignant. Since no obvious breast mass boundaries were visualized on 21 of the B-mode images that were isoechoic or similar to that of the background

tissue, SR estimates could be obtained on only 102 data sets. Visualization and segmentation of the mass was performed by an ultrasound scientist, and improved delineation might be obtained with a radiologist reading the same scans.

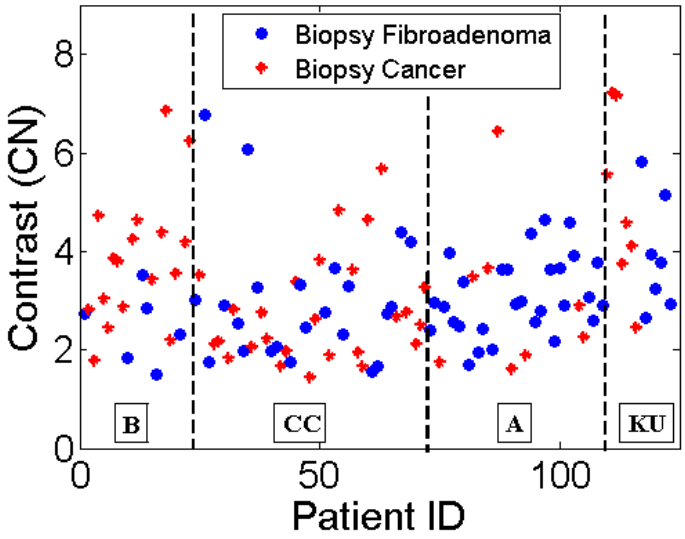

(a)

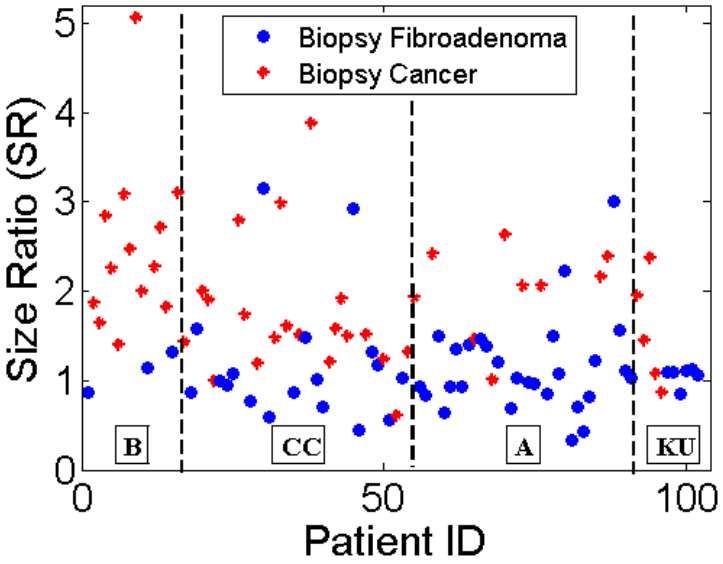

(b)

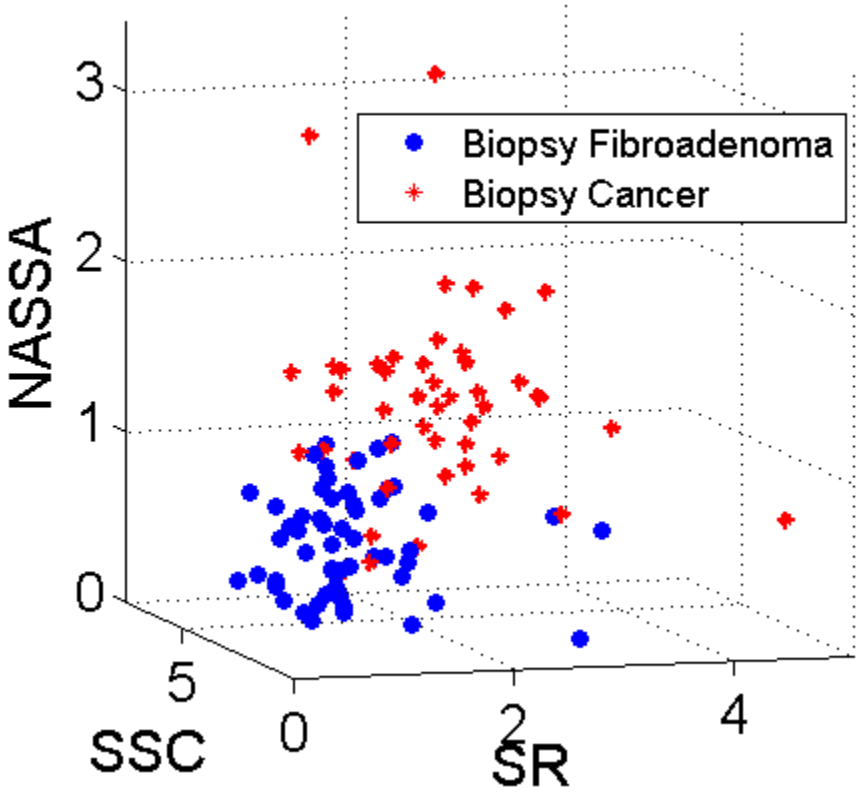

(c)

Figure 7.4 Scatter plots of *in vivo* differentiation between patients with cancers and fibroadenomas using the CN (a), SR (b) and 3D plots of integer NASSA with CN and SR(c) feature on a combined data set.

Figure 7.4, presents scatter plots of the CN, SR and the integer feature values for the patients in this study. Cases are separated according to the different institutions over which the data were collected. The x-axis of the scatter plot represents patient ID from the four institutions, while the y-axis represents the computed feature values. The CN and the NASSA feature values are shown over all 123 subjects in Figure 7.4 (a). The SR feature value on the other hand is shown for only 102 patients in Figure 7.4 (b) (c). The CN feature values alone do not provide effective classification between benign and malignant masses alone as shown in Figure 7.4 (a). However, the SR feature and the NASSA feature as shown in Figure 7.4(c) provide good differentiation between benign and malignant disease. In figure 7.4 (b) with few examinations value of the SR

feature from subjects diagnosed with malignant masses is larger than for subjects diagnosed with benign masses. Data in figure 7.4 (b, c) show that most of the malignant masses exhibit a NASSA value larger than 1.2 with a larger SR feature value, while benign masses have a NASSA value lower than 1.2 with a relatively small SR feature value.

Table 7.1 Area Under Curve (AUC) of single feature using both SVM based linear analysis with the conservative leave-one -out method and ROCKIT software.

Strain & Shear features	AUC (LibSVM)	AUC (ROCKIT)	95% (CI_{upper}-CI_{lower})	Sensitivity	Specificity
Stiffness Contrast (CN)	0.5239	0.5308	0.6355-0.4260	0.597	0.500
Size Ratio (SR)	0.8398	0.8468	0.9285-0.7651	0.804	0.715
NASSA	0.9042	0.9106	0.9631-0.8582	0.862	0.800

For the ROC analysis, the true positive rate indicates the fraction of biopsy proven malignant masses that are classified positive by the 'True' category. As previously mentioned the leave-one-out approach was utilized for this analysis. The ROC results presented in Figure 7.5 demonstrate the enhanced discrimination capability of the NASSA feature when compared to either the CN or the SR feature. The CN feature provides an AUC value of only 0.52, compared to an AUC for the SR feature of 0.84. The Area under the curve for the NASSA feature was 0.90. Combined all these features resulted in a AUC of 0.93 using LibSVM.

ROCKIT software was also utilized to evaluate single feature performance including AUC at both sides of the 95% confidence interval, and the sensitivity and specificity values from the ROC curve. Results are presented in Table 7.1. AUC values estimated from ROCKIT software were consistent with the AUC values estimated using LibSVM, however, the AUC values were

lower for the classifier using LibSVM. This is due to the conservative leave-one-out classifier used with LibSVM. The AUC of CN was 0.52 using the support vector machine (SVM) and 0.53 using ROCKIT software. SR provided an AUC value of 0.84 using LibSVM and 0.85 using ROCKIT software. Finally for the NASSA feature the AUC values were 0.90 using LibSVM and 0.91 using ROCKIT software.

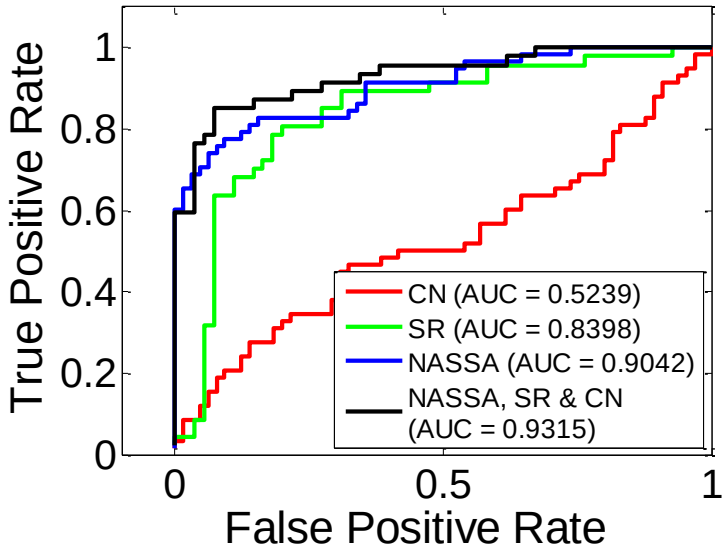

Figure 7.5 ROC curves for the NASSA (black curve), SR (red) and contrast (blue) feature from the *in-vivo* data acquired on the combined data set (A, B, CC and KU) for 102 patients (B/N = 55/47).

The diagnostic accuracy of CN, the stiffness contrast alone was 57.73% (95% CI, 0.6355-0.4260). The accuracy was 77.45% for the SR feature (95% CI, 0.9285-0.7651), and 82.93% (95% CI, 0.9631-0.8582) for the NASSA feature alone. Keep in mind that the AUC for the SR feature is subjective, since it will vary with the observer and their visualization of the mass on the B-mode image. However trained observers (i.e. radiologists) with sufficient time allocated to segment images have achieved an ROC area of about 0.93 [26, 32, 34]. The sensitivity and specificity of each classifier were also obtained from each binormal fitting curve. Our results

shown that the sensitivity and specificity improve greatly from use of the CN pattern to using SR to use of the NASSA feature.

Table 7.2 AUC, accuracy, sensitivity, specificity and specificity for a 100% sensitivity for different combined features using SVM based linear analysis using the conservative leave-one -out classifier.

Strain & Shear features	AUC (LibSVM)	Accuracy (LibSVM)	Sensitivity (LibSVM)	Specificity (LibSVM)	Specificity at 100% Sensitivity
SR & CN	0.8333	77.45% (79/102)	0.6383	0.8909	0.091
NASSA & SR	0.9342	88.24% (90/102)	0.8298	0.9273	0.309
NASSA & CN	0.906	85.29% (87/102)	0.7872	0.9091	0.291
NASSA & SR & CN	0.9315	89.22% (91/102)	0.8511	0.9273	0.328

The combined performances of these three features were also evaluated using the linear SVM based approach previously described to evaluate classification patterns [161] using the leave-one-out approach. The SVM was utilized to combine two or three of the features described above to obtain a combined discriminant for each patient to evaluate the ability of the combined feature data set to improve discrimination performance. The ROC results obtained using a linear classifier and the leave-one-out method for a combination of two and three of the features are illustrated in Figure 7.6. ROC curves that incorporate the SR values are far as 102 patients. The AUC values exhibit significant improvement with the incorporation of the NASSA feature, either with CN (0.90) or NASSA with SR (0.93). This data are also shown in Table 7.3. Though the AUC value with the incorporation of the NASSA feature with SR is greater than the classifier incorporating all the three features, one more data set (fibroadenoma) was discriminated when

CN was added to the classifier. 90 out of 102 data sets were accurately classified by NASSA and SR. This improved to 89.22% (91 out of 102) by incorporating NASSA, SR and CN. 102 of the 123 cases were accurately classified with the NASSA feature alone, with an accuracy rate 82.93%. In addition, the p-values of the CN, SR and NASSA features using a regression model for each of these variables were 1.88×10^{-3}, 1.37×10^{-7} and 1.78×10^{-5}, respectively. The t-test analysis indicates that the feature values (CN/SR/NASSA) for malignant cases are significantly higher than those for benign masses, with the difference being statistically significant.

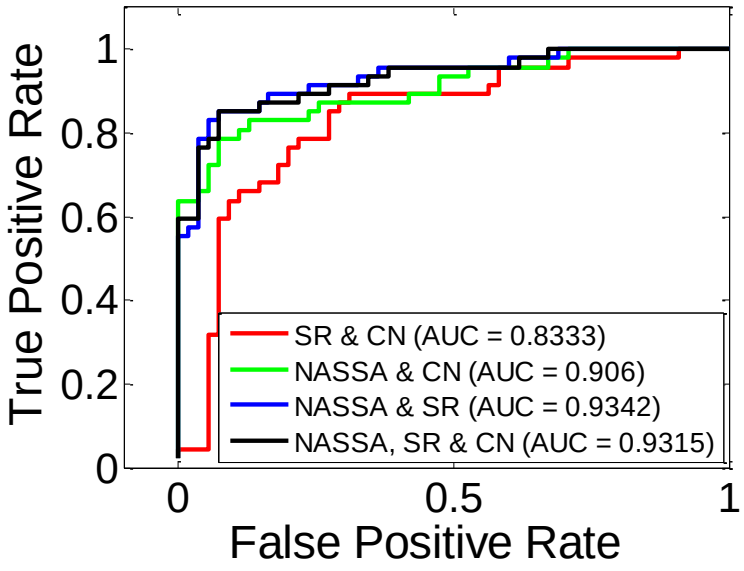

Figure 7.6 ROC curves for the combined features for the 102 patients (B/N = 55/47).

Since the ramifications of missing a cancer is significantly higher than a biopsy of a benign tissue, we also present specificity values for 100% sensitivity in the last column in Table 7.2. These are obtained directly from the ROC curves. The specificity using a linear SVM for the three features (NASSA + CN + SR) was 0.33, while the specificity for NASSA& SR was 0.31, for NASSA & CN was 0.29, and for SR & CN was 0.09. As suggested in the scatter plot in Figure 7.1, the presence of outliers greatly reduces the specificity values for a 100% sensitivity.

Table 7.3 Improved performance with the combined features over a single feature for both benign and malignant masses for the 102[a] *in vivo* data sets.

102 Data Sets (B/M: 55/47)	Improvement over CN		Improvement over SR	
	Benign	Malignant	Benign	Malignant
SR	12	15	0	0
NASSA	17	17	5	2
CN + SR	8	19	-4	4
NASSA + CN	17	18	5	3
NASSA + SR	19	19	7	4
NASSA+SR+CN	20	19	8	4

[a] Note that 21 data sets could not be utilized to determine the SR feature, thus the performance results over only 102 data sets were compared in this chapter.

The improved detection performance of both single and combined features is evident from data in Table 7.3. For the 102 (B/M: 55/47) *in vivo* data sets, 52 (B/M: 28/24) masses were classified using CN alone, 79 (B/M: 40/39) masses were discriminated by SR alone, and 86 (B/M: 47/39) masses were accurately classified using NASSA alone. Compared to the single feature i.e. CN, we obtained an improvement in the classification of 12 benign cases and 15 malignant cases with SR, NASSA further improves the benign mass discrimination performance by 5 cases and malignant mass discrimination performance by 2 cases for our analysis. Adding the CN feature to either the SR or NASSA feature improves the detection of malignant masses, but at the expense of reducing benign mass discrimination. As a result, the combined CN + SR feature does not improve the overall performance obtained with SR alone, and the combined NASSA + CN features improved the discrimination by only 1 case when compared to using only the NASSA feature. However, the combined NASSA + SR feature greatly improves the performance over the use of only the SR feature by 7 benign and 4 malignant masses, which can be further improved by adding the CN feature.

Table 7.4 Performance with single and combined feature for malignant masses over the 47 malignant masses out of 102*in-vivo* data sets

Types (47+**11**/102+**21**) (M : 47+**11**)	No.	Detected Malignant Mass Number						
		CN	**SR**	**NASSA**	**CN & SR**	**CN & NASSA**	**SR & NASSA**	**CN & SR & NASSA**
IDC	26+6	13+9	23	21+6	24	22+6	24	24
IDC & DCIS	4+1	3+1	2	3	2	3+1	2	2
DCIS	3	1+1	3	3	3	3	3	3
Invasive Lobular	4+1	2	4	4-1	4	4-1	4	4
Invasive Mammary	1	0	1	1-1	1	1-1	1	1
LCIS & DCIS	1	0	0	1	1	1	1	1
Metastatic Phylloides	1	0+1	1	1-1	1	1	1	1
Intracystic Papillary	1	0+1	0	1	1	1	1	1
Ductal CA	1	1-1	1	1	1	1	1	1
CA	5+3	2+1	4	5+2	5	5+2	5	5
Total number	47+11	22+13	39	41+5	43	42+7	43	43

The pathology performance of multi-features for malignant masses over the 47 malignant masses out of 102 (or 58 malignant masses out of 123) *in-vivo* data sets is shown in Table 7.4. SR alone only detected 39 out of 47 malignant masses, however, it significantly improved to 43 out of 47 combined with other features derived from strain and shear strain images. NASSA could detect 41 out of 47 malignant masses, and this improved to 43 out of 47 cases when other features were included with NASSA. Observe that the performance of the CN feature alone is relatively low (22/47) for malignant cases without isoechoic masses. Note that 35 out of 58 cases were correctly distinguished using CN alone. After adding 11 isoechoic malignant masses that cannot be detected using the SR feature, 7 more malignant masses were detected using the combined NASSA & CN feature.

7.4 Discussion & Conclusions

In this chapter, we present a leave-one-out classifier utilizing the stiffness contrast, size-ratio and the normalized axial shear strain area features for breast mass differentiation. Although some of these features have been independently evaluated by other investigators [26, 30-32, 34-35, 162], improvements in the differentiation obtained using a multi-feature analysis has not been evaluated thus far. These features, extracted from both the axial-strain and axial-shear strain images, demonstrate the potential for accurate classification of *in-vivo* breast masses as being either benign or malignant. Utilization of features such as the CN and NASSA that can be derived from the axial-strain and axial-shear images may also enable automated breast mass classification. In particular the normalization of the NASSA feature using features derived from the axial-strain image as described in this chapter and Xu et al. [20, 22, 151] can reduce the subjectivity associated with mass delineation on B-mode images reported by Thitaikumar et al. [157-158]. Breast mass delineation from B-mode images may require a radiologist or commercial segmentation software, while the breast mass can be easily segmented on the axial-strain images using automated approaches because of the large CN, as shown in Figure 8.1(a) where all masses have CN values greater than 1.5.

In our analysis we had to discard 21 scans since we were unable to determine the SR feature for these patients since the breast mass could not be accurately demarcated on the B-mode image. The SR and combined feature analysis were therefore only performed on 102 data sets (B/M = 55/47). This is a limitation since some breast masses are not clearly visualized in B-mode and drawing the mass boundary is subjective and varies with the observer [34]. Stravos [163] describes that a large percentage of fibroadenomas and around a third of the malignant masses are depicted on ultrasound B-mode images as isoechoic. This uncertainty with mass delineation on B-mode images can also lead to errors in the normalization of the NASSA feature

value as proposed by Thitaikumar et al. [157-158]. However, this is not the case when the mass boundary from the axial strain image is utilized for normalization as in Xu et al. [20, 22, 151].

Core needle biopsies are the standard for breast mass diagnosis with an approximate accuracy of 96% [164]. A majority of the core needle biopsies performed has been reported to fall into three categories i.e. normal (BI-RADS 1 or B1), benign/negative (B2) or malignant (B6) cases [165]. Variations with excision histology results [166] have been reported for borderline categories, i.e. masses that are suspicious for malignancy (B4 and B5) and lesions of uncertain malignant potential (B3) [167-169]. Inter-observer variability between pathologists for B3 and B4 masses has also been documented [170]. Studies have reported that only one-fifth [167] to one-sixth [169] of B3 core needle biopsies proved to be malignant on excision histological analysis. In addition, as expected, the likelihood of malignancy varied significantly for different malignancy subtypes [167-168]

Chapter 8:

Contributions & Future Work

The goal of this dissertation was to develop shear strain imaging and evaluate features derived from these images for breast mass differentiation and classification. We have developed a new 2D displacement tracking and strain estimation algorithm using parallelogram shaped kernels to estimate the displacement vector and normal and shear strain tensor images using beam-steered data. Our new algorithm provides significantly improved strain tensor image quality when compared to the previously utilized 1D tracking. In this chapter, we briefly summarize the contributions of this dissertation and provide suggestions for future work in this area of research.

8.1 Contributions of this Dissertation

1) A comprehensive analysis of features derived from axial strain and axial-shear strain images for breast tumor classification was presented in this dissertation. The impact of these different features on the classification and differentiation of breast masses into benign and malignant classes was also investigated in this dissertation.

In chapter 3, we created both 2D and 3D FEA models to simulate breast masses with different bonding condition (based on the friction coefficient), and orientation with respect to the direction of applied deformation direction. Local axial and lateral displacements vectors obtained from FEA were interpolated and incorporated into an ultrasound simulation. Displacement was

then tracked and estimated using our algorithms. A least squares strain estimator (LSQSE) estimator is utilized to obtain both normal and shear strain images. The results showed that on one hand, firmly bonded masses exhibit larger shearing areas with smaller magnitudes outside the inclusion, while the loosely bonded masses exhibit less shear, however exhibit higher magnitude values both within ("fill-in") and outside the inclusion. The feasibility of using Normalized axial-shear strain area (NASSA), negative normalized axial-shear strain area (N-NASSA), positive axial-shear strain area (P-NASSA) and normalized axial-shear strain magnitude (NASSM) features derived and normalized from axial shear strain images to differentiate tumor masses for different bounding conditions was also demonstrated in this chapter. We showed that the NASSA feature provides better discrimination results. A 20% normalized threshold was selected based on the simulation study. The results also showed that asymmetric lesions introduce additional "fill-in" artifacts in shear strain images.

Chapter 4 compared the performance between the NASSA feature obtained from axial-shear strain images and the NFSSA feature obtained from full-shear strain images. The use of different features derived from shear strain images for tumor classification was also investigated in this chapter. This was done by characterizing a tumor model using FEA with various stiffness ratio, tumor shapes, applied deformation and orientation of the mass with the applied deformation. Axial shear strain images obtained from tissue-mimicking (TM) phantoms using 1D tracking were also estimated in this chapter to demonstrate the feasibility of using the NASSA feature for breast tumor classification. The results showed that lesion size or shape for symmetric positioning of the mass within the background (or applied deformation) doesn't affect the detection performance. However, for asymmetric masses (masses at an angle to the applied deformation), artifacts termed the 'fill-in' reduce detection performance. Thus, our results

recommend placement of the transducer surface to be parallel to the breast mass whenever possible for data acquisition on patients. The results presented also show that higher stiffness ratios between the mass and background can improve the detection performance. However, larger deformations (>5%) will reduce the detectability due to the non-linear effects, where larger deformations will cause quasi-static assumption cannot be hold anymore. When compared to the NASSA feature, the NFSSA feature is more robust to noise (electronic, attenuation etc) and provide better performance for asymmetric masses. We also demonstrated that the 1D motion tracking method with beam-steered data, fails to track deformation at depths larger than 40mm due to increased attenuation with depth and signal decorrelation, which indicates the need to develop a new two-dimensional (2D) algorithm, that would enable the use of smaller processing kernels along the beam direction, to accurately estimate the displacement vector along both axial and lateral directions from angular beam steered radiofrequency (RF) data.

2) A new 2D deformation tracking algorithm for beam-steered data that incorporates 2Dparallelogram shaped 2D kernels was developed and evaluated in this dissertation to obtain full shear strain images as shown in chapter 5. This 2D kernel was used to estimate the 2D angular displacement vector from pre- and post- RF data pairs at different beam steered angles under a quasi-static deformation. Orthogonal components (axial and lateral) were calculated from the 2D angular displacements at various beam steered angles using a least-square compounding approach. Axial shear strain images were obtained from only the axial displacement vector using the LSQSE method. Four TM phantom models with symmetric/asymmetric, and bound/unbound tumor masses were utilized in this study to generate and compare axial and full shear strain images based on the new parallelogram

shaped 2D deformation tracking approach. Plots of the signal-to-noise (SNR_e) and contrast-to-noise (CNR_e) over ten independent RF data sets acquired on a uniformly elastic and inclusion TM phantoms were utilized to demonstrate the improved strain image quality using the new 2D deformation tracking when compared to the 1D approach. The impact of the angular increment and maximum steered angle were also investigated based on the plots of CNR_e and SNR_e. Results obtained with the uniformly elastic phantoms in this chapter demonstrated the significant improvement in the spatial resolution from 3 mm along the beam direction with the 1D method to 0.385mm in the 2D method. The SNR_e with 2D tracking is significantly better, while the CNR_e is approximately 8-14 dB better than the results obtained using 1D tracking and analysis. We also demonstrate that an angular beam-steered increment smaller than 5 °with a maximum angle larger than 6 °is necessary to obtain the compounded strain images.

3) We have demonstrated the ability of shear strain imaging to assess bonding and mobility of breast masses with the surrounding background tissue. Features derived from shear strain images can be utilized to differentiate benign from malignant breast masses. This was demonstrated on a multi-institutional *in-vivo* RF data set acquired at three different clinical locations equipped with different ultrasound systems. Breast mass differentiation was investigated using the NASSA feature in a classifier. In addition, a multi-feature classifier that integrated the NASSA feature with other previously proposed features (namely the size-ratio (SR) and stiffness contrast (CN)) to study the combined classification performance.

Chapter 6 verified the feasibility of using the NASSA feature obtained from axial shear strain images of *in-vivo* data sets for breast tumor diagnosis. Scatter plots of NASSA feature values

versus patient IDs were presented along with ROC curves to demonstrate the potential of using the axial-shear strain tensor for breast tumor classification.

In chapter 7, the NASSA feature was integrated with previously proposed features such as CN and SR to investigate the combined classification performance. ROC analysis was performed using a leave-one-out classifier to evaluate the potential of combining these features for breast mass differentiation.

8.2 Future Work

Based on the results and discussion in this dissertation, possible future work, in this research area includes:

1) Note that the viscoelastic model for tissue mechanics includes 81 independent parameters. Most of the current researches create tissue models using an orthotropic assumption to reduce the number of parameters from 81 to 27. The homogeneity assumption is then used to further reduce it to 12. Finally, with the isotropic assumption, the model now only requires two parameters to represent the entire viscoelastic deformation. Future research in this area, should utilize and create a more realistic mathematical model, with fewer assumptions for breast mass differentiation. A non-linear model that could incorporate isotropic-transverse, orthotropic and anisotropic parameters to model viscoelastic tissue is needed.
2) A median filter is generally used to filter noise artifacts and outliers from the displacement and strain estimated. An adaptive filter design can be used to further improve image pre-processing. Development of adaptive interpolation techniques can also improve the displacement accuracy. Strain estimators other than LSQSE can also be utilized to improve

both strain and shear strain image quality. The development of an adaptive breast mass segmentation method on strain images can also be utilized to automate the analysis.

3) Development of real time 2D deformation tracking and registration algorithms for bream steered data can also help the clinical utility of *in-vivo* shear strain images for breast tumor classification. The sum of absolute difference or squares can be used as the similarity matrix in the first level to provide initial coarse motion tracking displacement values. An effective and adaptive interpolation method can also reduce the necessary search region dimensions for the final level calculation using cross-correlation as the similarity matrix.

4) An effective RF data compression method can also help to acquire 3D pre- and post- volume RF data with 2D array transducers efficiently. A precise and robust 3D motion tracking algorithm can also help to locate the tumor and provide accurate classification results.

8.3 References

[1] ACS, "Breast Cancer Overview," 2013.

[2] E. a. T. Ueno, E. and Itoh, K., "Classification and diagnostic criteria in breast echography," *Jpn J Med Ultrasonics,* vol. 13, pp. 19-31, 1986 1986.

[3] E. Konofagou and J. Ophir, "A new elastographic method for estimation and imaging of lateral displacements, lateral strains, corrected axial strains and Poisson's ratios in tissues," *Ultrasound Med Biol,* vol. 24, pp. 1183-99, Oct 1998.

[4] C. Cole-Beuglet, R. Z. Soriano, A. B. Kurtz, and B. B. Goldberg, "Fibroadenoma of the breast: sonomammography correlated with pathology in 122 patients," *AJR Am J Roentgenol,* vol. 140, pp. 369-75, Feb 1983.

[5] A. J. Leibman, M. Lewis, and B. Kruse, "Tubular carcinoma of the breast: mammographic appearance," *AJR Am J Roentgenol,* vol. 160, pp. 263-5, Feb 1993.

[6] P. Skaane and K. Engedal, "Analysis of sonographic features in the differentiation of fibroadenoma and invasive ductal carcinoma," *AJR Am J Roentgenol,* vol. 170, pp. 109-114, 1998.

[7] E. J. Chen, R. S. Adler, P. L. Carson, W. K. Jenkins, and W. D. O'Brien, Jr., "Ultrasound tissue displacement imaging with application to breast cancer," *Ultrasound Med Biol,* vol. 21, pp. 1153-62, 1995.

[8] T. M. Kolb, J. Lichy, and J. H. Newhouse, "Comparison of the performance of screening mammography, physical examination, and breast US and evaluation of factors that influence them: an analysis of 27,825 patient evaluations," *Radiology,* vol. 225, pp. 165-75, Oct 2002.

[9] W. A. Berg, L. Gutierrez, M. S. NessAiver, W. B. Carter, M. Bhargavan, R. S. Lewis, and O. B. Ioffe, "Diagnostic accuracy of mammography, clinical examination, US, and MR imaging in preoperative assessment of breast cancer," *Radiology,* vol. 233, pp. 830-49, Dec 2004.

[10] W. A. Berg, Z. Zhang, D. Lehrer, R. A. Jong, E. D. Pisano, R. G. Barr, M. Bohm-Velez, M. C. Mahoney, W. P. Evans, 3rd, L. H. Larsen, M. J. Morton, E. B. Mendelson, D. M. Farria, J. B. Cormack, H. S. Marques, A. Adams, N. M. Yeh, and G. Gabrielli, "Detection of breast cancer with addition of annual screening ultrasound or a single screening MRI to mammography in women with elevated breast cancer risk," *JAMA,* vol. 307, pp. 1394-404, Apr 4 2012.

[11] W. A. Berg, J. D. Blume, A. M. Adams, R. A. Jong, R. G. Barr, D. E. Lehrer, E. D. Pisano, W. P. Evans, 3rd, M. C. Mahoney, L. Hovanessian Larsen, G. J. Gabrielli, and E. B. Mendelson, "Reasons women at elevated risk of breast cancer refuse breast MR imaging screening: ACRIN 6666," *Radiology,* vol. 254, pp. 79-87, Jan 2010.

[12] W. A. Berg, J. D. Blume, J. B. Cormack, E. B. Mendelson, D. Lehrer, M. Bohm-Velez, E. D. Pisano, R. A. Jong, W. P. Evans, M. J. Morton, M. C. Mahoney, L. H. Larsen, R. G. Barr, D. M. Farria, H. S. Marques, and K. Boparai, "Combined screening with ultrasound and mammography vs mammography alone in women at elevated risk of breast cancer," *JAMA,* vol. 299, pp. 2151-63, May 14 2008.

[13] C. K. Kuhl, S. Schrading, C. C. Leutner, N. Morakkabati-Spitz, E. Wardelmann, R. Fimmers, W. Kuhn, and H. H. Schild, "Mammography, breast ultrasound, and magnetic resonance imaging for surveillance of women at high familial risk for breast cancer," *J Clin Oncol,* vol. 23, pp. 8469-76, Nov 20 2005.

[14] B. E. Sirovich and H. C. Sox, Jr., "Breast cancer screening," *Surg Clin North Am,* vol. 79, pp. 961-90, Oct 1999.

[15] K. Kerlikowske, R. Smith-Bindman, B. M. Ljung, and D. Grady, "Evaluation of abnormal mammography results and palpable breast abnormalities," *Ann Intern Med,* vol. 139, pp. 274-84, Aug 19 2003.

[16] D. Gur, L. P. Wallace, A. H. Klym, L. A. Hardesty, G. S. Abrams, R. Shah, and J. H. Sumkin, "Trends in recall, biopsy, and positive biopsy rates for screening mammography in an academic practice," *Radiology,* vol. 235, pp. 396-401, May 2005.

[17] K. R. Nightingale, P. J. Kornguth, W. F. Walker, B. A. McDermott, and G. E. Trahey, "A novel ultrasonic technique for differentiating cysts from solid lesions: preliminary results in the breast," *Ultrasound Med Biol,* vol. 21, pp. 745-51, 1995.

[18] K. R. Nightingale, P. J. Kornguth, and G. E. Trahey, "The use of acoustic streaming in breast lesion diagnosis: a clinical study," *Ultrasound Med Biol,* vol. 25, pp. 75-87, Jan 1999.

[19] K. Nightingale, M. S. Soo, R. Nightingale, and G. Trahey, "Acoustic radiation force impulse imaging: in vivo demonstration of clinical feasibility," *Ultrasound Med Biol,* vol. 28, pp. 227-35, 2002.

[20] H. Xu, M. Rao, T. Varghese, A. Sommer, S. Baker, T. J. Hall, G. A. Sisney, and E. S. Burnside, "Axial-shear strain imaging for differentiating benign and malignant breast masses," *Ultrasound Med Biol,* vol. 36, pp. 1813-24, Nov 2010.

[21] H. Xu and T. Varghese, "Normal and shear strain imaging using 2D deformation tracking on beam steered linear array datasets," *Med Phys,* vol. 40, p. 012902, Jan 2013.

[22] H. Xu, T. Varghese, and E. L. Madsen, "Analysis of shear strain imaging for classifying breast masses: finite element and phantom results," *Med Phys,* vol. 38, pp. 6119-27, Nov 2011.

[23] E. S. Burnside, T. J. Hall, A. M. Sommer, G. K. Hesley, G. A. Sisney, W. E. Svensson, J. P. Fine, J. Jiang, and N. J. Hangiandreou, "Differentiating benign from malignant solid breast masses with US strain imaging," *Radiology,* vol. 245, pp. 401-10, Nov 2007.

[24] M. Tanter, J. Bercoff, A. Athanasiou, T. Deffieux, J. L. Gennisson, G. Montaldo, M. Muller, A. Tardivon, and M. Fink, "Quantitative assessment of breast lesion viscoelasticity: initial clinical results using supersonic shear imaging," *Ultrasound Med Biol,* vol. 34, pp. 1373-86, Sep 2008.

[25] H. Frey, "[Realtime elastography. A new ultrasound procedure for the reconstruction of tissue elasticity]," *Radiologe,* vol. 43, pp. 850-5, Oct 2003.

[26] D. M. Regner, G. K. Hesley, N. J. Hangiandreou, M. J. Morton, M. R. Nordland, D. D. Meixner, T. J. Hall, M. A. Farrell, J. N. Mandrekar, W. S. Harmsen, and J. W. Charboneau, "Breast lesions: evaluation with US strain imaging--clinical experience of multiple observers," *Radiology,* vol. 238, pp. 425-37, Feb 2006.

[27] P. Ricci, E. Maggini, E. Mancuso, P. Lodise, V. Cantisani, and C. Catalano, "Clinical application of breast elastography: State of the art," *Eur J Radiol,* Jun 17 2013.

[28] A. Yi, N. Cho, J. M. Chang, H. R. Koo, B. La Yun, and W. K. Moon, "Sonoelastography for 1786 non-palpable breast masses: diagnostic value in the decision to biopsy," *Eur Radiol,* Nov 25 2011.

[29] J. Ophir, I. Cespedes, H. Ponnekanti, Y. Yazdi, and X. Li, "Elastography: a quantitative method for imaging the elasticity of biological tissues," *Ultrasonic Imaging,* vol. 13, pp. 111-34, 1991.

[30] B. S. Garra, E. I. Cespedes, J. Ophir, S. R. Spratt, R. A. Zuurbier, C. M. Magnant, and M. F. Pennanen, "Elastography of breast lesions: initial clinical results," *Radiology,* vol. 202, pp. 79-86, Jan 1997.

[31] K. M. Hiltawsky, M. Kruger, C. Starke, L. Heuser, H. Ermert, and A. Jensen, "Freehand ultrasound elastography of breast lesions: clinical results," *Ultrasound Med Biol,* vol. 27, pp. 1461-9, 2001.

[32] T. J. Hall, Y. Zhu, and C. S. Spalding, "In vivo real-time freehand palpation imaging,," *Ultrasound Med Biol,* vol. 29, pp. 427-435, 2003.

[33] T. Varghese, "Quasi-static ultrasound elastography," *Ultrasound Clinics,* vol. 4, pp. 323-338, 2009.

[34] E. S. Burnside, T. J. Hall, A. M. Sommer, G. K. Hesley, G. A. Sisney, W. E. Svensson, J. P. Fine, J. Jiang, and N. J. Hangiandreou, "Differentiating benign from malignant solid breast masses with US strain imaging," *Radiology:,* vol. 245, pp. 401-10, 2007.

[35] R. G. Barr, "Real-time ultrasound elasticity of the breast: initial clinical results," *Ultrasound Q,* vol. 26, pp. 61-66, 2010.

[36] K. Taylor, S. O'Keeffe, P. D. Britton, M. G. Wallis, G. M. Treece, J. Housden, D. Parashar, S. Bond, and R. Sinnatamby, "Ultrasound elastography as an adjuvant to conventional

ultrasound in the preoperative assessment of axillary lymph nodes in suspected breast cancer: a pilot study," *Clin Radiol,* vol. 66, pp. 1064-71, Nov 2011.

[37] P. N. Wells and H. D. Liang, "Medical ultrasound: imaging of soft tissue strain and elasticity," *J R Soc Interface,* vol. 8, pp. 1521-49, Nov 7 2011.

[38] S. Korukonda and M. M. Doyley, "Estimating axial and lateral strain using a synthetic aperture elastographic imaging system," *Ultrasound Med Biol,* vol. 37, pp. 1893-908, Nov 2011.

[39] Y. Qiu, M. Sridhar, J. K. Tsou, K. K. Lindfors, and M. F. Insana, "Ultrasonic viscoelasticity imaging of nonpalpable breast tumors: preliminary results," *Acad Radiol,* vol. 15, pp. 1526-33, Dec 2008.

[40] W. A. Berg, D. O. Cosgrove, C. J. Dore, F. K. Schafer, W. E. Svensson, R. J. Hooley, R. Ohlinger, E. B. Mendelson, C. Balu-Maestro, M. Locatelli, C. Tourasse, B. C. Cavanaugh, V. Juhan, A. T. Stavros, A. Tardivon, J. Gay, J. P. Henry, and C. Cohen-Bacrie, "Shear-wave elastography improves the specificity of breast US: the BE1 multinational study of 939 masses," *Radiology,* vol. 262, pp. 435-49, Feb 2012.

[41] J. J. Wild and J. M. Reid, "Echographic visualization of lesions of the living intact human breast," *Cancer Res,* vol. 14, pp. 277-82, May 1954.

[42] W. A. Berg, "Beyond standard mammographic screening: mammography at age extremes, ultrasound, and MR imaging," *Radiol Clin North Am,* vol. 45, pp. 895-906, vii, Sep 2007.

[43] ACS, "Breast Cancer Overview," 2010.

[44] C. H. Lee, D. D. Dershaw, D. Kopans, P. Evans, B. Monsees, D. Monticciolo, R. J. Brenner, L. Bassett, W. Berg, S. Feig, E. Hendrick, E. Mendelson, C. D'Orsi, E. Sickles, and L. W. Burhenne, "Breast cancer screening with imaging: recommendations from the Society of Breast Imaging and the ACR on the use of mammography, breast MRI, breast ultrasound, and other technologies for the detection of clinically occult breast cancer," *J Am Coll Radiol,* vol. 7, pp. 18-27, Jan 2010.

[45] J. G. Elmore, K. Armstrong, C. D. Lehman, and S. W. Fletcher, "Screening for breast cancer," *JAMA,* vol. 293, pp. 1245-56, Mar 9 2005.

[46] M. B. A.Goddi, S.Alessi, "Breast elastography: A literature review," *Journal of Ultrasound,* 2012.

[47] H. M. Dobson, "Screening for breast cancer: an overview," *Scottish Medical Journal,* vol. 53, pp. 36-41, Aug 2008.

[48] K. Horsch, M. L. Giger, C. J. Vyborny, L. Lan, E. B. Mendelson, and R. E. Hendrick, "Classification of breast lesions with multimodality computer-aided diagnosis: observer study results on an independent clinical data set," *Radiology,* vol. 240, pp. 357-68, Aug 2006.

[49] A. T. Stavros, D. Thickman, C. L. Rapp, M. A. Dennis, S. H. Parker, and G. A. Sisney, "Solid breast nodules: use of sonography to distinguish between benign and malignant lesions," *Radiology,* vol. 196, pp. 123-34, Jul 1995.

[50] W. K. Moon, J. S. Myung, Y. J. Lee, I. A. Park, D. Y. Noh, and Y. G. Im, "US of ductal carcinoma in situ," *Radiographics,* vol. 22, pp. 269-280, Mar-Apr 2002.

[51] U. Techavipoo, Q. Chen, T. Varghese, J. A. Zagzebski, and E. L. Madsen, "Noise reduction using spatial-angular compounding for elastography," *IEEE Trans Ultrason Ferroel Freq Cont,* vol. 51, pp. 510-520, 2004.

[52] Y. W. Chang, K. H. Kwon, D. E. Goo, D. L. Choi, H. K. Lee, and S. B. Yang, "Sonographic differentiation of benign and malignant cystic lesions of the breast," *J Ultrasound Med,* vol. 26, pp. 47-53, Jan 2007.

[53] A. S. Hong, E. L. Rosen, M. S. Soo, and J. A. Baker, "BI-RADS for sonography: positive and negative predictive values of sonographic features," *AJR Am J Roentgenol,* vol. 184, pp. 1260-5, Apr 2005.

[54] M. B. Mainiero, A. Goldkamp, E. Lazarus, L. Livingston, S. L. Koelliker, B. Schepps, and W. W. Mayo-Smith, "Characterization of breast masses with sonography: can biopsy of some solid masses be deferred?," *J Ultrasound Med,* vol. 24, pp. 161-7, Feb 2005.

[55] T. A. Krouskop, T. M. Wheeler, F. Kallel, and T. Hall, "The elastic moduli of breast and prostate tissues under compression," *Ultrasonic Imaging,* vol. 20, pp. 260-274, 1998.

[56] K. M. Hiltawsky, M. Kruger, C. Starke, L. Heuser, H. Ermert, and A. Jensen, "Freehand ultrasound elastography of breast lesions: clinical results," *Ultrasound in Medicine & Biology,* vol. 27, pp. 1461-9, 2001.

[57] J. Ophir, S. K. Alam, B. Garra, F. Kallel, E. Konofagou, T. Krouskop, and T. Varghese, "Elastography: ultrasonic estimation and imaging of the elastic properties of tissues," *Proc Inst Mech Eng [H],* vol. 213, pp. 203-33., 1999.

[58] T. A. Krouskop, D. R. Dougherty, and F. S. Vinson, "A pulsed Doppler ultrasonic system for making noninvasive measurements of the mechanical properties of soft tissue," *Journal Rehab. Res. Dev,* vol. 24, pp. 1-8, 1987.

[59] K. J. Parker, S. R. Huang, R. A. Musulin, and R. M. Lerner, "Tissue response to mechanical vibrations for 'sonoelasticity imaging'," *Ultrasound in Medicine & Biology,* vol. 16, pp. 241-6, 1990.

[60] G. C. C. Charles H.Knapp, "The Generalized Correlation Method for Estimation of Time Delay," *IEEE Trans on Acoustics, Speech and Signal Processing,* vol. 24, Aug 1976 1976.

[61] P. Chaturvedi, M. F. Insana, and T. J. Hall, "2-D companding for noise reduction in strain imaging," *IEEE Trans Ultrason Ferroelectr Freq Control,* vol. 45, pp. 179-91, 1998.

[62] Y. Zhu and T. J. Hall, "A modified block matching method for real-time freehand strain imaging," *Ultrason Imaging,* vol. 24, pp. 161-76, Jul 2002.

[63] F. Kallel and J. Ophir, "Three-dimensional tissue motion and its effect on image noise in elastography," *IEEE Trans Ultrason Ferroel Freq Cont,* vol. 44, pp. 1286-96, 1997.

[64] X. Chen, H. Xie, R. Erkamp, K. Kim, C. Jia, J. M. Rubin, and M. O'Donnell, "3-D correlation-based speckle tracking," *Ultrason Imaging,* vol. 27, pp. 21-36, Jan 2005.

[65] M. O'Donnell, A. R. Skovoroda, B. M. Shapo, and S. Y. Emelianov, "Internal displacement and strain imaging using ultrasonic speckle tracking," *IEEE Trans Ultrason Ferroel Freq Cont,* vol. 41, pp. 314-25, 1994.

[66] T. Varghese, J. Ophir, E. Konofagou, F. Kallel, and R. Righetti, "Tradeoffs in elastographic imaging," *Ultrason Imaging,* vol. 23, pp. 216-48, Oct 2001.

[67] M. A. Lubinski, S. Y. Emelianov, K. R. Raghavan, A. E. Yagle, A. R. Skovoroda, and O. D. M, "Lateral displacement estimation using tissue incompressibility," *IEEE Trans Ultrason Ferroel Freq Cont,* vol. 43, pp. 247-56, 1996.

[68] I. Cespedes, Y. Huang, J. Ophir, and S. Spratt, "Methods for estimation of subsample time delays of digitized echo signals," *Ultrason Imaging,* vol. 17, pp. 142-71, Apr 1995.

[69] F. Viola and W. F. Walker, "A spline-based algorithm for continuous time-delay estimation using sampled data," *IEEE Trans Ultrason Ferroelectr Freq Control,* vol. 52, pp. 80-93, Jan 2005.

[70] R. G. Lopata, M. M. Nillesen, H. H. Hansen, I. H. Gerrits, J. M. Thijssen, and C. L. de Korte, "Performance evaluation of methods for two-dimensional displacement and strain estimation using ultrasound radio frequency data," *Ultrasound Med Biol,* vol. 35, pp. 796-812, May 2009.

[71] F. Viola, R. L. Coe, K. Owen, D. A. Guenther, and W. F. Walker, "MUlti-Dimensional Spline-Based Estimator (MUSE) for motion estimation: algorithm development and initial results," *Ann Biomed Eng,* vol. 36, pp. 1942-60, Dec 2008.

[72] U. Techavipoo, Q. Chen, T. Varghese, and J. Zagzebski, "Estimation of displacement vectors and strain tensors in elastography using angular insonifications," *IEEE Trans Med Imaging,* vol. 23, pp. 1479-1489, 2004.

[73] M. Rao, Q. Chen, H. Shi, and T. Varghese, "Spatial-Angular Compounding for Elastography Using Beam Steering on Linear Array Transducers," *Med Phys,* vol. 33, pp. 618-26, 2006.

[74] M. Rao and T. Varghese, "Correlation analysis for angular compounding in strain imaging," *IEEE Trans Ultrason Ferroelectr Freq Control,* vol. 54, pp. 1903-7, Sep 2007.

[75] M. Rao and T. Varghese, "Spatial angular compounding for elastography without the incompressibility assumption," *Ultrason Imaging,* vol. 27, pp. 256-70, Oct 2005.

[76] H. Chen and T. Varghese, "Noise analysis and improvement of displacement vector estimation from angular displacements," *Med Phys,* vol. 35, pp. 2007-17, May 2008.

[77] G. M. Treece, A. H. Gee, and R. W. Prager, "Ultrasound compounding with automatic attenuation compensation using paired angle scans," *Ultrasound Med Biol,* vol. 33, pp. 630-42, Apr 2007.

[78] R. Zahiri Azar, A. Baghani, S. E. Salcudean, and R. Rohling, "2-D high-frame-rate dynamic elastography using delay compensated and angularly compounded motion vectors: preliminary results," *IEEE Trans Ultrason Ferroelectr Freq Control,* vol. 57, pp. 2421-36, Nov 2010.

[79] H. H. Hansen, R. G. Lopata, T. Idzenga, and C. L. de Korte, "Full 2D displacement vector and strain tensor estimation for superficial tissue using beam-steered ultrasound imaging," *Phys Med Biol,* vol. 55, pp. 3201-18, Jun 7 2010.

[80] E. E. Konofagou, T. Harrigan, and J. Ophir, "Shear strain estimation and lesion mobility assessment in elastography," *Ultrasonics,* vol. 38, pp. 400-4, 2000.

[81] J. R. McLaughlin, D., "Shear wave speed recovery in transient elastography and supersonic imaging using propagating fronts," *Inverse Prob.,* vol. 22, pp. 681-706, 2006.

[82] M. L. Palmeri, M. H. Wang, J. J. Dahl, K. D. Frinkley, and K. R. Nightingale, "Quantifying hepatic shear modulus in vivo using acoustic radiation force," *Ultrasound Med Biol,* vol. 34, pp. 546-58, Apr 2008.

[83] J. Bercoff, M. Tanter, and M. Fink, "Supersonic shear imaging: a new technique for soft tissue elasticity mapping," *IEEE Trans Ultrason Ferroelectr Freq Control,* vol. 51, pp. 396-409, Apr 2004.

[84] J. R. Doherty, G. E. Trahey, K. R. Nightingale, and M. L. Palmeri, "Acoustic radiation force elasticity imaging in diagnostic ultrasound," *IEEE Trans Ultrason Ferroelectr Freq Control,* vol. 60, pp. 685-701, Apr 2013.

[85] S. F. Levinson, M. Shinagawa, and T. Sato, "Sonoelastic determination of human skeletal muscle elasticity," *Journal of Biomechanics,* vol. 28, pp. 1145-54, 1995.

[86] N. Cho, W. K. Moon, H. Y. Kim, J. M. Chang, S. H. Park, and C. Y. Lyou, "Sonoelastographic strain index for differentiation of benign and malignant nonpalpable breast masses," *J Ultrasound Med,* vol. 29, pp. 1-7, Jan 2010.

[87] S. Y. Chung, W. K. Moon, J. W. Choi, N. Cho, M. Jang, and K. G. Kim, "Differentiation of benign from malignant nonpalpable breast masses: a comparison of computer-assisted quantification and visual assessment of lesion stiffness with the use of sonographic elastography," *Acta Radiol,* vol. 51, pp. 9-14, Feb 2010.

[88] W. K. Moon, C. S. Huang, W. C. Shen, E. Takada, R. F. Chang, J. Joe, M. Nakajima, and M. Kobayashi, "Analysis of elastographic and B-mode features at sonoelastography for breast tumor classification," *Ultrasound in Medicine and Biology,* vol. 35, pp. 1794-802, Nov 2009.

[89] F. K. Schaefer, I. Heer, P. J. Schaefer, C. Mundhenke, S. Osterholz, B. M. Order, N. Hofheinz, J. Hedderich, M. Heller, W. Jonat, and I. Schreer, "Breast ultrasound elastography-Results of 193 breast lesions in a prospective study with histopathologic correlation," *Eur J Radiol,* Sep 19 2009.

[90] A. Itoh, E. Ueno, E. Tohno, H. Kamma, H. Takahashi, T. Shiina, M. Yamakawa, and T. Matsumura, "Breast disease: clinical application of US elastography for diagnosis," *Radiology,* vol. 239, pp. 341-50, May 2006.

[91] T. Shiina, N. Nitta, E. Ueno, and J. Bamber, "Real time tissue elasticity imaging using the combined autocorrelation method," *J Med Ultrason,* vol. 29, pp. 119-128, 2002.

[92] B. J. Mendelson EB, Berg WA, et al., "BI-RADS:Ultrasound," *American College of Radiology,* 2003.

[93] G. Rizzatto, "Real-time Elastography of the Breast in Clinical Practice - The Italian experience," *Department of Diagnostic Imaging ASS 2 Isontina, Gorizia, Italy,* 2006.

[94] A. L. Rizzatto G, Baldassarre S, Bulzacki A, Della Sala S, Locatelli M, et al., "Characterization of brest lesions with real-time sonoelastography: results from the Italian multicenter clinical trial," presented at the RSNA, Chicago, USA, 2006.

[95] R. G. Barr, "Real-time ultrasound elasticity of the breast: initial clinical results," *Ultrasound Q,* vol. 26, pp. 61-6, Jun 2010.

[96] R. G. Barr, S. Destounis, L. B. Lackey, 2nd, W. E. Svensson, C. Balleyguier, and C. Smith, "Evaluation of breast lesions using sonographic elasticity imaging: a multicenter trial," *J Ultrasound Med,* vol. 31, pp. 281-7, Feb 2012.

[97] K. R. Nightingale, R. W. Nightingale, M. L. Palmeri, and G. E. Trahey, "A finite element model of remote palpation of breast lesions using radiation force: factors affecting tissue displacement," *Ultrason Imaging,* vol. 22, pp. 35-54, Jan 2000.

[98] W. Meng, G. Zhang, C. Wu, G. Wu, Y. Song, and Z. Lu, "Preliminary results of acoustic radiation force impulse (ARFI) ultrasound imaging of breast lesions," *Ultrasound Med Biol,* vol. 37, pp. 1436-43, Sep 2011.

[99] A. C. Sharma, Soo, M.S., Trahey, G.E. & Nightingale, K.R., "Acoustic radiation force impulse imaging of *in vivo* breast masses," *IEEE Ultrasonics Symp,* vol. 1, pp. 728 -731, 2004.

[100] M. L. Palmeri and K. R. Nightingale, "Acoustic radiation force-based elasticity imaging methods," *Interface Focus,* vol. 1, pp. 553-64, Aug 6 2011.

[101] M. Tozaki, S. Isobe, and E. Fukuma, "Preliminary study of ultrasonographic tissue quantification of the breast using the acoustic radiation force impulse (ARFI) technology," *Eur J Radiol,* vol. 80, pp. e182-7, Nov 2011.

[102] M. Tozaki, S. Isobe, and M. Sakamoto, "Combination of elastography and tissue quantification using the acoustic radiation force impulse (ARFI) technology for differential diagnosis of breast masses," *Jpn J Radiol,* Jul 18 2012.

[103] A. P. Sarvazyan, O. V. Rudenko, S. D. Swanson, J. B. Fowlkes, and S. Y. Emelianov, "Shear wave elasticity imaging: a new ultrasonic technology of medical diagnostics," *Ultrasound Med Biol,* vol. 24, pp. 1419-35, Nov 1998.

[104] A. P. Sarvazyan, *Elastic Properties of Soft Tissue*, 2001.

[105] M. H. Wang, M. L. Palmeri, V. M. Rotemberg, N. C. Rouze, and K. R. Nightingale, "Improving the robustness of time-of-flight based shear wave speed reconstruction methods using RANSAC in human liver in vivo," *Ultrasound Med Biol,* vol. 36, pp. 802-13, May 2010.

[106] M. Tanter, J. Bercoff, L. Sandrin, and M. Fink, "Ultrafast compound imaging for 2-D motion vector estimation: application to transient elastography," *IEEE Trans Ultrason Ferroelectr Freq Control,* vol. 49, pp. 1363-74, Oct 2002.

[107] J. M. Chang, I. A. Park, S. H. Lee, W. H. Kim, M. S. Bae, H. R. Koo, A. Yi, S. J. Kim, N. Cho, and W. K. Moon, "Stiffness of tumours measured by shear-wave elastography correlated with subtypes of breast cancer," *Eur Radiol,* vol. 23, pp. 2450-8, Sep 2013.

[108] J. H. Youk, H. M. Gweon, E. J. Son, K. H. Han, and J. A. Kim, "Diagnostic value of commercially available shear-wave elastography for breast cancers: integration into BI-RADS classification with subcategories of category 4," *Eur Radiol,* vol. 23, pp. 2695-704, Oct 2013.

[109] S. H. Lee, N. Cho, J. M. Chang, H. R. Koo, J. Y. Kim, W. H. Kim, M. S. Bae, A. Yi, and W. K. Moon, "Two-View versus Single-View Shear-Wave Elastography: Comparison of Observer Performance in Differentiating Benign from Malignant Breast Masses," *Radiology,* Sep 12 2013.

[110] K. J. Parker, S. R. Huang, R. A. Musulin, and R. M. Lerner, "Tissue response to mechanical vibrations for "sonoelasticity imaging"," *Ultrasound Med Biol,* vol. 16, pp. 241-6, 1990.

[111] L. S. Taylor, B. C. Porter, D. J. Rubens, and K. J. Parker, "Three-dimensional sonoelastography: principles and practices," *Phys Med Biol,* vol. 45, pp. 1477-94, Jun 2000.

[112] T. A. Krouskop, D. R. Dougherty, and F. S. Vinson, "A pulsed Doppler ultrasonic system for making noninvasive measurements of the mechanical properties of soft tissue," *J Rehabil Res Dev,* vol. 24, pp. 1-8, Spring 1987.

[113] R. M. Lerner, S. R. Huang, and K. J. Parker, ""Sonoelasticity" images derived from ultrasound signals in mechanically vibrated tissues," *Ultrasound Med Biol,* vol. 16, pp. 231-9, 1990.

[114] M. Fatemi and J. F. Greenleaf, "Ultrasound-stimulated vibro-acoustic spectrography," *Science,* vol. 280, pp. 82-5, Apr 3 1998.

[115] M. Fatemi and J. F. Greenleaf, "Vibro-acoustography: an imaging modality based on ultrasound-stimulated acoustic emission," *Proc Natl Acad Sci U S A,* vol. 96, pp. 6603-8, Jun 8 1999.

[116] M. W. Urban, M. Fatemi, and J. F. Greenleaf, "Modulation of ultrasound to produce multifrequency radiation force," *J Acoust Soc Am,* vol. 127, pp. 1228-38, Mar 2010.

[117] A. Alizad, M. Fatemi, D. H. Whaley, and J. F. Greenleaf, "Application of vibro-acoustography for detection of calcified arteries in breast tissue," *J Ultrasound Med,* vol. 23, pp. 267-73, Feb 2004.

[118] A. Alizad, D. H. Whaley, M. W. Urban, R. E. Carter, R. R. Kinnick, J. F. Greenleaf, and M. Fatemi, "Breast vibro-acoustography: initial results show promise," *Breast Cancer Res,* vol. 14, p. R128, Sep 29 2012.

[119] A. Samani, J. Zubovits, and D. Plewes, "Elastic moduli of normal and pathological human breast tissues: an inversion-technique-based investigation of 169 samples," *Phys Med Biol,* vol. 52, pp. 1565-76, Mar 21 2007.

[120] A. Samani, J. Bishop, and D. B. Plewes, "A constrained modulus reconstruction technique for breast cancer assessment," *IEEE Trans Med Imaging,* vol. 20, pp. 877-85, Sep 2001.

[121] Y. Zhu, T. J. Hall, and J. Jiang, "A finite-element approach for Young's modulus reconstruction," *IEEE Trans Med Imaging,* vol. 22, pp. 890-901, Jul 2003.

[122] M. Rao, Q. Chen, H. Shi, T. Varghese, E. L. Madsen, and J. A. Zagzebski, "Normal and Shear Strain Estimation Using Beam Steering on Linear-Array Transducers," *Ultrasound Med Biol.,* vol. 33, pp. 57-66, 2007.

[123] A. Thitaikumar, L. M. Mobbs, C. M. Kraemer-Chant, B. S. Garra, and J. Ophir, "Breast tumor classification using axial shear strain elastography: a feasibility study," *Phys Med Biol,* vol. 53, pp. 4809-23, 2008.

[124] A. Thitaikumar, T. A. Krouskop, B. S. Garra, and J. Ophir, "Visualization of bonding at an inclusion boundary using axial-shear strain elastography: a feasibility study," *Phys Med Biol,* vol. 52, pp. 2615-33, 2007.

[125] M. Rao, T. Varghese, and E. L. Madsen, "Shear strain imaging using shear deformations," *Med Phys,* vol. 35, pp. 412-23, 2008.

[126] F. Kallel and J. Ophir, "A least-squares strain estimator for elastography," *Ultrasonic Imaging,* vol. 19, pp. 195-208, 1997.

[127] B. Galaz, A. K. Thittai, and J. Ophir, "Axial-shear strain distributions in an elliptical inclusion model: A simulation study (abstract) pp. 99," presented at the 8th Intl conf Ultrason Meas Imag Tissue Elasticity, Vlissingen, Zeeland, Netherlands, 2009.

[128] A. K. Thittai, B. Galaz, and J. Ophir, "Axial-shear strain distributions in an elliptical inclusion model: experimental validation and in vivo examples with implications to breast tumor classification," *Ultrasound Med Biol,* vol. 36, pp. 814-20, 2010.

[129] U. Techavipoo, Q. Chen, T. Varghese, and J. A. Zagzebski, "Estimation of displacement vectors and strain tensors in elastography using angular insonifications," *IEEE Trans Med Imaging,* vol. 23, pp. 1479-89, Dec 2004.

[130] M. Rao, Q. Chen, H. Shi, T. Varghese, E. L. Madsen, J. A. Zagzebski, and T. A. Wilson, "Normal and shear strain estimation using beam steering on linear-array transducers," *Ultrasound Med Biol,* vol. 33, pp. 57-66, Jan 2007.

[131] E. L. Madsen, M. A. Hobson, H. Shi, T. Varghese, and G. R. Frank, "Stability of heterogeneous elastography phantoms made from oil dispersions in aqueous gels," *Ultrasound Med Biol,* vol. 32, pp. 261-270, 2006.

[132] E. L. Madsen, M. A. Hobson, G. Frank, H. Shi, J. Jiang, T. J. Hall, T. Varghese, M. M. Doyley, and J. B. Weaver, "Anthropomorphic breast phantoms for testing elastography systems," *Ultrasound Med Biol,* vol. 32, pp. 857-874, 2006.

[133] M. Rao, "Shear Strain Elastography for Breast Cancer Diagnosis," Doctor of Philosophy, Medical Physics, University of Wisconsin-Madison, Madison, 2008.

[134] B. S. Garra, "Imaging and estimation of tissue elasticity by ultrasound," *Ultrasound Q,* vol. 23, pp. 255-68, 2007.

[135] U. Techavipoo and T. Varghese, "Improvements in elastographic contrast-to-noise ratio using spatial-angular compounding," *Ultrasound Med Biol,* vol. 31, pp. 529-36, Apr 2005.

[136] T. Varghese, "Quasi-Static Ultrasound Elastography," *Ultrasound Clin,* vol. 4, pp. 323-338, Jul 2009.

[137] F. Kallel and J. Ophir, "A least-squares strain estimator for elastography," *Ultrason Imaging,* vol. 19, pp. 195-208, Jul 1997.

[138] T. Varghese and J. Ophir, "The nonstationary strain filter in elastography: Part I. Frequency dependent attenuation," *Ultrasound Med Biol,* vol. 23, pp. 1343-56, 1997.

[139] T. Varghese and J. Ophir, "An analysis of elastographic contrast-to-noise ratio," *Ultrasound Med Biol,* vol. 24, pp. 915-24, Jul 1998.

[140] S. Gefen, O. J. Tretiak, C. W. Piccoli, K. D. Donohue, A. P. Petropulu, P. M. Shankar, V. A. Dumane, L. Huang, M. A. Kutay, V. Genis, F. Forsberg, J. M. Reid, and B. B. Goldberg, "ROC analysis of ultrasound tissue characterization classifiers for breast cancer diagnosis," *IEEE Trans Med Imaging*, vol. 22, pp. 170-177, 2003.

[141] Y. Jiang, C. E. Metz, and R. M. Nishikawa, "A receiver operating characteristic partial area index for highly sensitive diagnostic tests," *Radiology*, vol. 210, pp. 745-750, 1996.

[142] K. Drukker, C. A. Sennett, and M. L. Giger, "Automated method for improving system performance of computer-aided diagnosis in breast ultrasound," *IEEE Trans Med Imaging*, vol. 28, pp. 122-8, 2009.

[143] K. Drukker, N. P. Gruszauskas, C. A. Sennett, and M. L. Giger, "Breast US computer-aided diagnosis workstation: performance with a large clinical diagnostic population," *Radiology*, vol. 248, pp. 392-7, 2008.

[144] J. A. Swets and R. M. Pickett, *Evaluation of diagnostic systems: methods from signal detection theory*. New York, NY Academic Press, 1982.

[145] C. E. Metz, "ROC methodology in radiologic imaging," *Invest Radiol*, vol. 21, pp. 720-733, 1986.

[146] D. M. Green and J. M. Swets, *Signal detection theory and psychophysics*. New York: John Wiley and Sons Inc., 1966.

[147] C. E. Metz and X. Pan, ""Proper" Binormal ROC Curves: Theory and Maximum-Likelihood Estimation," *J Math Psychol*, vol. 43, pp. 1-33, Mar 1999.

[148] L. L. Pesce and C. E. Metz, "Reliable and computationally efficient maximum-likelihood estimation of "proper" binormal ROC curves," *Acad Radiol*, vol. 14, pp. 814-29, Jul 2007.

[149] D. D. Dorfman and K. S. Berbaum, "Degeneracy and discrete receiver operating characteristic rating data," *Acad Radiol*, vol. 2, pp. 907-15, Oct 1995.

[150] H. Shi and T. Varghese, "Two-dimensional multi-level strain estimation for discontinuous tissue," *Phys Med Biol*, vol. 52, pp. 389-401, 2007.

[151] H. Xu, M. Rao, T. Varghese, S. Baker, A. M. Sommer, T. J. Hall, E. S. Burnside, and G. A. Sisney, "Axial shear strain imaging for breast mass differentiation," *IEEE UFFC*, vol. 1, pp. 534-437, 2009.

[152] H. Xu, T. Varghese, J. Jiang, and J. A. Zagzebski, "In vivo classification of breast masses using features derived from axial-strain and axial-shear images," *Ultrason Imaging*, vol. 34, pp. 222-36, Oct 2012.

[153] M. Rao and T. Varghese, "Spatial angular compounding for elastography without the incompressibility assumption," *Ultrason Imaging*, vol. 27, pp. 256-270, 2005.

[154] J. Ophir, B. Garra, F. Kallel, E. Konofagou, T. Krouskop, R. Righetti, and T. Varghese, "Elastographic imaging," *Ultrasound Med Biol,* vol. 26, suppl., pp. S23-9, 2000.

[155] B. S. Garra, "Elastography: current status, future prospects, and making it work for you," *Ultrasound Q,* vol. 27, pp. 177-86, 2011.

[156] D. T. Ginat, S. V. Destounis, R. G. Barr, B. Castaneda, J. G. Strang, and D. J. Rubens, "US elastography of breast and prostate lesions," *Radiographics,* vol. 29, pp. 2007-16, 2009.

[157] A. Thitaikumar, T. A. Krouskop, B. S. Garra, and J. Ophir, "Visualization of bonding at an inclusion boundary using axial-shear strain elastography: a feasibility study," *Physics In Medicine And Biology,* vol. 52, pp. 2615-2633, May 7 2007.

[158] A. Thitaikumar, L. M. Mobbs, C. M. Kraemer-Chant, B. S. Garra, and J. Ophir, "Breast tumor classification using axial shear strain elastography: a feasibility study.," *Phys Med Biol,* vol. 53, pp. 4809-23, 2008.

[159] C.-C. a. L. Chang, Chih-Jen, "LIBSVM : a library for support vector machines," *ACM Transactions on Intelligent Systems and Technology,* vol. 2, pp. 27:1- 27, 2011.

[160] V. Vapnik, *The Nature of Statistical Learning Theory*. New York: Springer-Verlag, 1995.

[161] R. F. Chang, W. J. Wu, W. K. Moon, Y. H. Chou, and D. R. Chen, "Support vector machines for diagnosis of breast tumors on US images," *Acad Radiol,* vol. 10, pp. 189-97, 2003.

[162] T. J. Hall, A. A. Oberai, P. E. Barbone, A. M. Sommer, N. H. Gokhale, S. Goenezent, and J. Jiang, "Elastic nonlinearity imaging," *Conf Proc IEEE Eng Med Biol Soc.*, pp. 1967-70, 2009.

[163] A. T. Stavros, *Breast ultrasound* vol. vii pp 95. Philadelphia, PA, USA: Lippincott Williams & Wilkins, c2004., 2004.

[164] M. H. Bukhari and Z. M. Akhtar, "Comparison of accuracy of diagnostic modalities for evaluation of breast cancer with review of literature," *Diagn Cytopathol,* vol. 37, pp. 416-424, 2009.

[165] A. H. Lee, H. E. Denley, S. E. Pinder, I. O. Ellis, C. W. Elston, P. Vujovic, R. D. Macmillan, and A. J. Evans, "Excision biopsy findings of patients with breast needle core biopsies reported as suspicious of malignancy (B4) or lesion of uncertain malignant potential (B3)," *Histopathology,* vol. 42, pp. 331-336, 2003.

[166] T. C. Kwok, E. A. Rakha, A. H. Lee, M. Grainge, A. R. Green, I. O. Ellis, and D. G. Powe, "Histological grading of breast cancer on needle core biopsy: the role of immunohistochemical assessment of proliferation," *Histopathology,* vol. 2010, p. 2, 2010.

[167] M. E. El-Sayed, E. A. Rakha, J. Reed, A. H. Lee, A. J. Evans, and I. O. Ellis, "Predictive value of needle core biopsy diagnoses of lesions of uncertain malignant potential (B3) in

abnormalities detected by mammographic screening," *Histopathology,* vol. 53, pp. 650-657, 2008.

[168] M. F. Dillon, E. W. McDermott, A. D. Hill, A. O'Doherty, N. O'Higgins, and C. M. Quinn, "Predictive value of breast lesions of "uncertain malignant potential" and "suspicious for malignancy" determined by needle core biopsy.," *Ann Surg Oncol,* vol. 14, pp. 704-711, 2007.

[169] B. D. Hayes, A. O'Doherty, and C. M. Quinn, "Correlation of needle core biopsy with excision histology in screen-detected B3 lesions: the Merrion Breast Screening Unit experience," *J Clin Pathol,* vol. 62, pp. 1136-1140, 2009.

[170] F. A. Zito, P. Verderio, G. Simone, V. Angione, P. Apicella, S. Bianchi, A. F. Conde, O. Hameed, J. Ibarra, A. Leong, N. Pennelli, E. Pezzica, V. Vezzosi, V. Ventrella, S. Pizzamiglio, A. Paradiso, and I. O. Ellis, "Reproducibility in the diagnosis of needle core biopsies of non-palpable breast lesions: an international study using virtual slides published on the world-wide web," *Histopathology,* vol. 56, pp. 720-726, 2010.